TU Delft

Delft University of Technology

Anisotropic Joint Migration Inversion: Automatic estimation of reflectivities and anisotropic velocities

Alshuhail, Abdulrahman

DOI
10.4233/uuid:3746fbe1-fd8a-4b5e-aa0b-a09c69ac0abc

Publication date
2017

Document Version
Final published version

Citation (APA)
Alshuhail, A. (2017). *Anisotropic Joint Migration Inversion: Automatic estimation of reflectivities and anisotropic velocities*. [Dissertation (TU Delft), Delft University of Technology].
https://doi.org/10.4233/uuid:3746fbe1-fd8a-4b5e-aa0b-a09c69ac0abc

Important note
To cite this publication, please use the final published version (if applicable).
Please check the document version above.

Copyright
Other than for strictly personal use, it is not permitted to download, forward or distribute the text or part of it, without the consent of the author(s) and/or copyright holder(s), unless the work is under an open content license such as Creative Commons.

Takedown policy
Please contact us and provide details if you believe this document breaches copyrights.
We will remove access to the work immediately and investigate your claim.

This work is downloaded from Delft University of Technology.
For technical reasons the number of authors shown on this cover page is limited to a maximum of 10.

Anisotropic Joint Migration Inversion: Automatic estimation of reflectivities and anisotropic velocities

Anisotropic Joint Migration Inversion: Automatic estimation of reflectivities and anisotropic velocities

PROEFSCHRIFT

ter verkrijging van de graad van doctor
aan de Technische Universiteit Delft,
op gezag van de Rector Magnificus prof. ir. K.C.A.M. Luyben,
voorzitter van het College voor Promoties,
in het openbaar te verdedigen
op donderdag 6 juli 2017 om 12:30 uur

door

Abdulrahman Abdullatif A ALSHUHAIL

Master of Science in Earth Science and Engineering
King Abdullah University of Science and Technology, Saoedi-Arabië
geboren te Hofuf, Saoedi-Arabië

Dit proefschrift is goedgekeurd door de promotor:
Prof. dr. ir. L.J. van Vliet

en de copromotor:
Dr. ir. D.J. Verschuur

Samenstelling promotiecommissie:

Rector Magnificus,	voorzitter
Prof. dr. ir. L.J van Vliet,	promotor, Technische Universiteit Delft
Dr. ir. D.J. Verschuur,	copromotor, Technische Universiteit Delft

Onafhankelijke leden:

Prof. dr. ir. J.T. Fokkema,	Technische Universiteit Delft
Prof. dr. A. Metrikine,	Technische Universiteit Delft
Prof. dr. T. Alkhalifah,	King Abdullah Univ. of Science and Tech.
Prof. dr. C.D. MacBeth,	Heriot Watt University
Dr. B.E. Cox,	Shell Intl. Exploration & Production

ISBN 978-94-6186-830-5

Copyright ©2017, by A. Alshuhail. All rights reserved. No part of this publication may be reproduced, stored in a retrieval system or transmitted in any form or by any means, electronic, mechanical, photocopying, recording or otherwise, without the prior written permission of the author.

Typesetting system: LaTeX.

To the most inspirational scientist that I have ever known:
Dr. Abdullatif Alshuhail

Contents

1

Introduction

1.1 Reflection Seismology

The objective of reflection seismology is to collect information about the Earth's subsurface, without having to resort to drilling. It has been and continues to be a major asset in identifying geologic structures and rock properties for the hydrocarbon exploration and production industry, but also finds applications in civil engineering (shallow subsurface) and global seismology (deep subsurface). The underlying principle behind this methodology is relatively straightforward. Active seismic sources and an array of detectors (usually hydrophones or geophones) are placed at or near the surface. When the sources are excited, they generate elastic waves that propagate through the Earth's interior. The strength and frequency of the source dictates how deep the waves penetrate. For a depth of investigation of 10km (sufficient for oil and gas exploration purposes) a bandwidth of 100Hz is acceptable [Yilmaz, 1987]. As these waves travel in the subsurface they refract, diffract, and reflect due to the variations in elastic properties in the subsurface. The detectors record the waves that make it back to the surface, similar to when we hear echoes in a cave. Figure 1.1 schematically shows the methodology on a subset of the 2007 BP TTI Velocity-Analysis Benchmark model. [1] By

[1] The model is created by Hemang Shah and is provided courtesy of BP Exploration Operation Company Limited.

processing and careful interpretation of the acquired seismic data, one is able to shed some light on the subsurface. Typical subsurface properties that are obtained are the reflectivities and the propagation velocities of the subsurface. These distributions can be used to further understand the local geology. Dobrin and Savit [1988] and Telford et al. [1990] provide a comprehensive overview of reflection seismology.

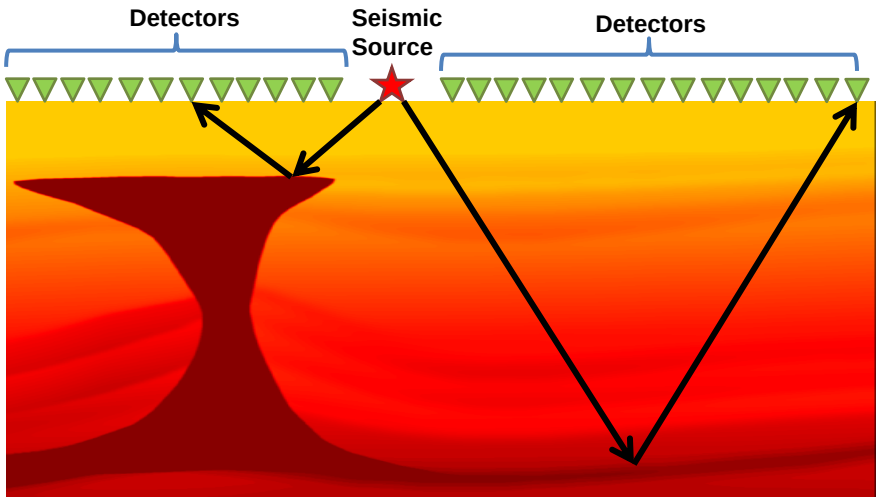

Figure 1.1: *Schematic representation of a seismic experiment.*

Traditionally, reflection seismology has been used to get a general idea of the Earth's reflectivity; recently however, it is used to obtain a plethora of subsurface properties, such as velocities, anisotropic parameters, and porosity to name a few. The method is constantly advancing from the acquisition side, from building more powerful broadband sources to commissioning more geophones for use in a single survey. The method is also constantly evolving from the processing side, more parts of the measured wavefields are being utilized and better inversion algorithms are constantly being developed in order to estimate the subsurface properties in complex geological settings.

1.2 Seismic Imaging

One of the most crucial attributes obtained from reflection seismology is the seismic image. It maps the reflected seismic data to its correct position in the subsurface. For this reason the seismic image has become a crucial part of exploration and reservoir monitoring. For homogeneous horizontal layers the reflections will originate from a reflection point directly underneath the midpoint between source and receiver. However, if the subsurface is not layered or not laterally homogeneous, as in the case of dipping layers, the reflected events will not necessarily map to the midpoint. Imaging resolves this issue by mapping or 'migrating' the reflections to their correct positions [Robinson, 1983], which is why imaging is often referred to as migration in reflection seismology. Therefore, seismic imaging can be defined as a mapping process where the reflected events are mapped to their true subsurface location. The main advantages of seismic imaging can be summarized as:

- Mapping dipping layers to their true subsurface position.
- Collapsing diffractions to their origin at the diffraction points.
- Resolving any conflicting dips if the geology is complicated.

Figure 1.2 exemplifies the effects of imaging, given the true velocity model. The true subsurface reflectivity resembles a syncline (figure 1.2a). Figure 1.2b shows the zero-offset section where we assume that reflection is generated underneath the midpoint of the source and receiver. Note that for the horizontal layers the zero-offset section is adequate. However, for the dipping structures the dip is incorrect in the zero-offset section. Furthermore, there are many diffractions that are not focused in the zero-offset section. Figure 1.2c shows the image after the imaging process is applied to the recorded data. Note that the reflections are at their true subsurface position and the diffractions are collapsed at their apex. Imaging algorithms can be categorized in terms of two categories: integral methods and wavefield continuation methods [Biondi, 2006].

1.2.1 Integral methods

Integral methods (also referred to as Kirchoff methods) are usually based on calculating arrival times in the subsurface (via ray tracing or eikonal

a)

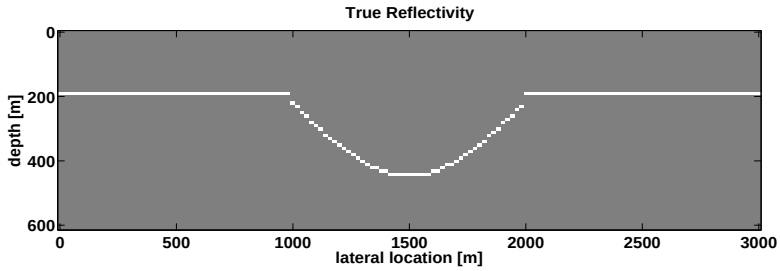

b)

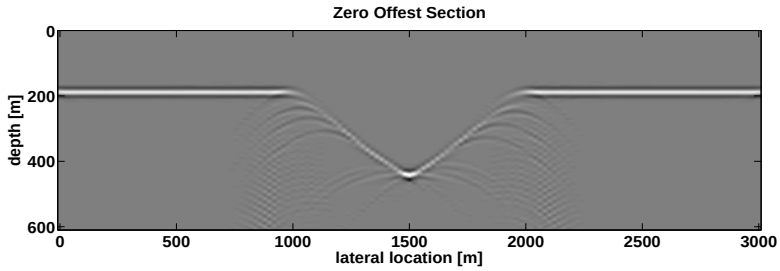

c)

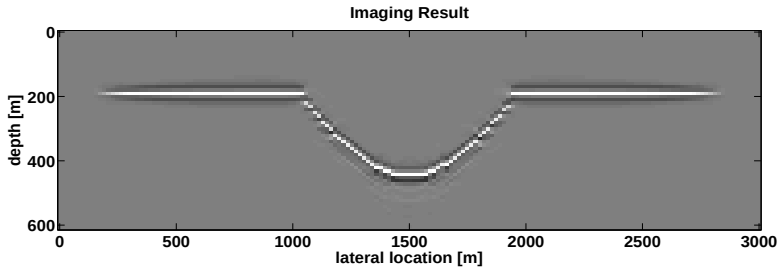

Figure 1.2: *The effects of imaging. a) The true reflectivity. b) The zero-offset section. c) The imaging result.*

solver for example) and a weighted summation over surfaces [Schneider, 1978]. The idea behind them is that every point in the subsurface is a potential scatterer that can generate a diffraction. Therefore, at every image point we integrate the data over a diffraction time surface in order to focus the events to the apex. The integral surface is defined by the subsurface parameters (such as velocity and anisotropy) and is usually computed numerically via the

Eikonal equation [Bleistein, 1987]. Since it uses travel times, a high frequency approximation of the wave equation is assumed. Therefore, the maximum source wavelength should be less than 1/3 of the minimum wavelength of velocity variation [Bleistein, 1984]. Integral methods are attractive because they can handle irregularly sampled data [Biondi and Shan, 2002] and are less computationally expensive to compute compared to wavefield continuation methods in general [Gray et al., 2001].

1.2.2 Wavefield Continuation Methods

Wavefield continuation methods [Claerbout, 1971; Stolt, 1978; Berkhout, 1980; Claerbout, 1985] can be described by three steps:

[1] Forward propagate the source wavefield.

[2] Back propagate the receiver wavefield.

[3] Apply the imaging condition at each point in the subsurface.

Wavefield continuation methods (also referred to as wave-equation migration (WEM) methods) can yield better results than integral methods because they take into account the whole range of seismic frequencies. They also handle multi-pathing better than integral methods, since the whole wavefield is taken into account. The method in which the wavefields are propagated (extrapolated) can further define the type of wavefield continuation method. Two of the most common methods employed, that will be visited frequently in this thesis, are Reverse Time Migration (RTM) and recursive extrapolation (alternatively called downward-continuation methods).

Reverse Time Migration

Reverse Time Migration (RTM) is a wavefield continuation method that can potentially image all dips [Baysal et al., 1983; McMechan, 1983]. The forward- and back-propagation of the source and receiver wavefield respectively are carried out along the time axis via finite-differences (FD), as an example. FD methods are based upon computing the solution to the wave-equation via finite-difference approximations of the involved spatial derivatives [Robertsson et al., 1994; Virieux, 1986], they provide an implicit solution

to the Green's function for wavefield propagation. One can apply the method to different types of wave-equations. For example, Igel et al. [1995] show that it is possible to apply it to an anisotropic elastic wave-equation. A unique property of FD is that the extrapolation is done in time, which allows the waves to propagate in all directions. For the source wavefield extrapolation, FD is run in a forward mode where time increases. However, for the receiver wavefield extrapolation, FD is run in a reverse mode where time decreases (hence, the name reverse time migration). Since it allows waves to propagate in all direction it can image all dips with great accuracy. However, the drawback is that this usually comes at a significant computational cost [Anderson et al., 2012]. Another issue with RTM is that sharp discontinuities in the velocity model cause internal reflections, which can further manifest as crosstalk artifacts in the image [Biondi, 2006].

Recursive Extrapolation

Recursive extrapolation methods propagates the source wavefield and the receiver wavefield along the depth axis as opposed to the time axis in RTM. It utilizes one-way operators, often referred to as phase-shift operators, to extrapolate the wavefields along the depth axis [Gazdag, 1978; Berkhout, 1980]. The computations can be carried out in the temporal-frequency domain which substantially reduces the computational cost. It also provides more flexibility in that sharp discontinuities of the velocity model do not cause internal reflections, because the propagation is independent from the reflection. We will revisit this property when formulating the inversion strategy in chapter 3. The main drawback of recursive methods is that they do not propagate the wavefield in all directions naturally, which limits the range of dips that are imaged. Therefore, overturned events such as diving waves will not be accounted for nor will they contribute to an image. Methods have been developed to extend the imaged dips [Shan and Biondi, 2004; Davydenko and Verschuur, 2014], they usually involve a change in coordinate system.

Closed-loop Migration

Imaging in general can be formulated as a closed-loop process, were it is possible to iterate with the reflectivity as unknown as done in so-called least-squares imaging [Nemeth et al., 1999]. For each iteration, forward modeling

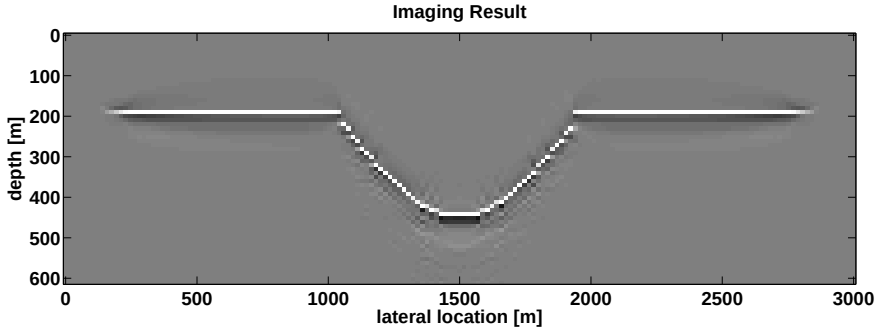

Figure 1.3: *Results of imaging the syncline of figure 1.2a in a closed-loop approach. Note that the reflectors are sharper compared to figure 1.2c.*

generates synthetic seismic data, a residual is computed from the difference between the observed and the synthetic data. The residual is back propagated and the imaging condition is applied. Finally a scaled version of the image gradient is added to the image obtained from the previous iteration. Although, computationally more expensive (since each iteration involves imaging) it increases the resolution of the reflectors and allows for more accurate amplitudes [Nemeth et al., 1999; Plessix and Mulder, 2004; Aldawood et al., 2015]. Figure 1.3 demonstrates the effects of closed-loop imaging on the same model as in figure 1.2a. Note that a sharper image is obtained with a closed-loop process.

Full Wavefield Migration (FWM) is a recently developed closed-loop imaging method that falls within the recursive extrapolation category [Berkhout, 2014b; Davydenko and Verschuur, 2017]. It utilizes recursive one-way operators to propagate both the source and receiver wavefields along the depth axis. FWM considers not only primaries in imaging but multiple scattering as well, without having to define multiples generating surfaces. Utilizing multiples usually broadens the subsurface illumination and attenuates the effect of shadow zones, which provides a more balanced illumination of the subsurface [Kumar et al., 2014; Davydenko and Verschuur, 2017]. Furthermore, they provide a better vertical resolution of the subsurface [Jiang et al., 2007]. Its inversion-based formulation enables the method to take into account the true-amplitudes and the transmission effects. Finally, since it is an recursive extrapolation method it avoids scattering the wavefields at

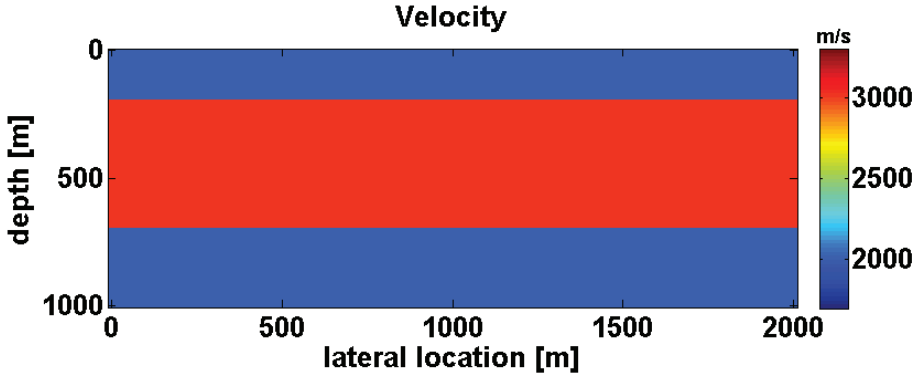

Figure 1.4: *The true velocity model.*

velocity discontinuities, which reduces the amount of crosstalk appearing in the image. Moreover, the velocity model does not need to be smooth in order to avoid the scattering.

1.3 Velocity

Velocity estimation is a crucial step associated to the imaging process. In order to get an accurate image one needs an accurate velocity model, which is especially the case for the more advanced imaging techniques (such as RTM). To better understand the effect of velocity on imaging, imaging is applied to a simple model with and without the correct velocity model. Figure 1.4 shows the true velocity model. Figure 1.5 shows the imaging result at $1000m$ lateral location using the correct velocity model, while figure 1.6 shows the imaging result at the same location using an erroneous velocity model. Notice that the image of the second reflector is at an incorrect depth and has a significantly weaker amplitude. Another example showing the significance of the velocity model on imaging is demonstrated on the syncline model from figure 1.2. The velocity model used for imaging in $800m/s$ faster than the true velocity model. Note that the reflections are not in the correct locations and the syncline is not focused.

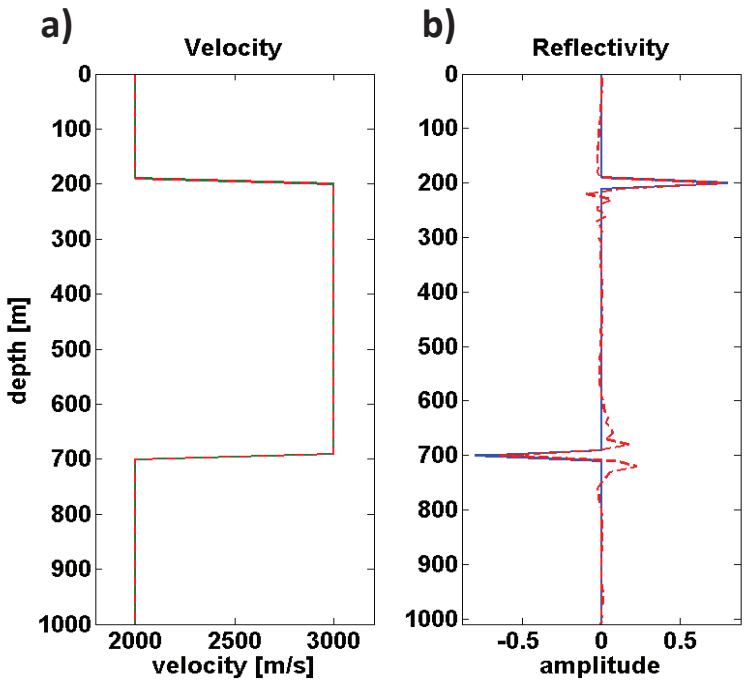

Figure 1.5: *Imaging with the true velocity model. a) The true velocity model in blue and the velocity model used for imaging is in red. b) The true image in blue while the estimated image is in red.*

Velocity estimates can be categorized in two categories: The first is direct velocity estimates, an example of which is the velocity obtained from sonic logs. The second category is the so-called processing velocity (or pro-velocity), which is an indirect estimate of velocity obtained from processing seismic data [Al-Chalabi, 2014]. Usually direct velocity estimates provide more accurate estimates compared to pro-velocities. However, they require a well to be drilled, which is rarely satisfied. In this thesis the velocities refer to the pro-velocities in that they are indirect estimates.

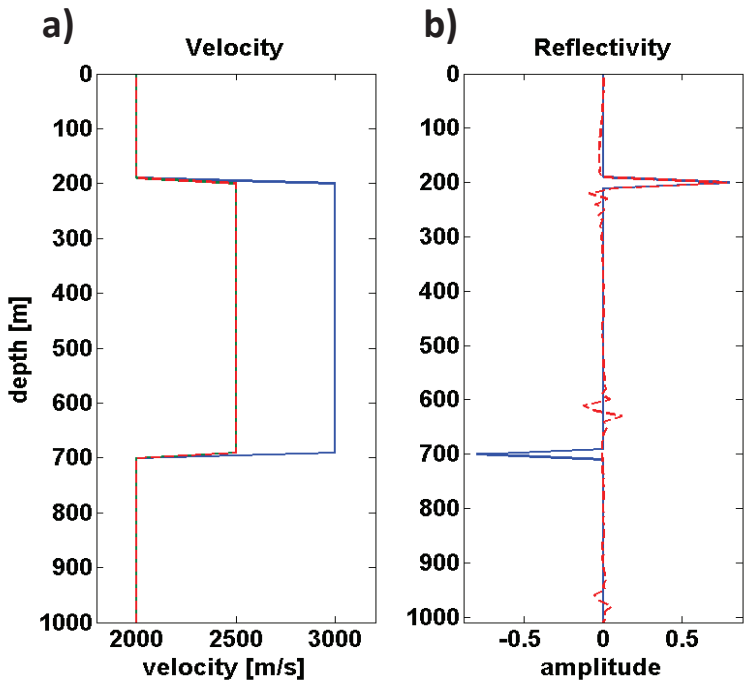

Figure 1.6: *Imaging with the wrong velocity model. a) The true velocity model in blue and the velocity model used for imaging is in red. b) The true image in blue while the estimated image is in red.*

1.3.1 NMO Velocity Analysis

Traditionally, velocity is estimated as a separate step from imaging. For a horizontally layered medium velocity analysis displays (semblance plots) are generated and a user picks the Normal Move-Out (NMO) velocity function that generates the maximum coherence from these plots. Picking the correct NMO velocity is always a challenge since the maximum coherence is not necessarily attributed to the correct velocity. Furthermore, the method is prone to user bias and is time consuming, as it has to be done for a wide range of lateral locations. The NMO velocity can be equated to the Root Mean Square (RMS) velocity for short spreadlength (i.e. short offsets). Using

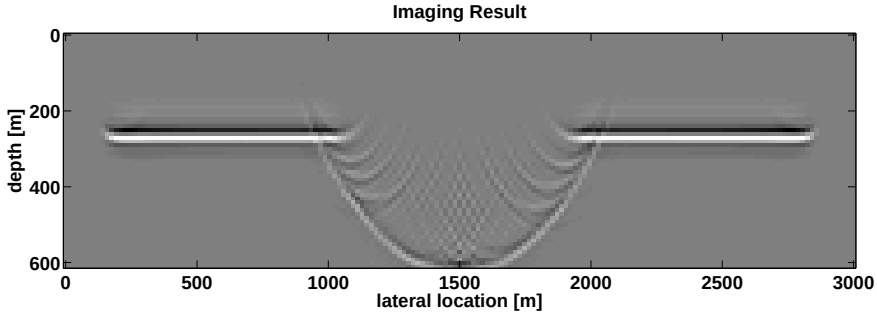

Figure 1.7: *Result of imaging the syncline of figure 1.2 with the wrong velocity model. The true velocity is* $2000m/s$ *whereas the imaging velocity is* $2800m/s$.

the Dix formula [Dix, 1955] the RMS velocity can be translated into interval velocities that can be used for imaging. For an extensive overview on traditional velocity analysis methods and strategies the reader is referred to Robein [2003], Jones [2010], and Al-Chalabi [2014]. Note, however, that for dipping structures with strong lateral velocity changes a Dix-type inversion process may neither be appropriate nor sufficient to estimate the interval velocities.

1.3.2 Model-domain Velocity Estimation

For more complex media, one can take advantage of imaging to estimate velocities [Al-Yahya, 1989; Symes and Carazzone, 1991] as done in Migration Velocity Analysis (MVA). MVA methods consist of imaging the data with an approximate velocity model, followed by updating the corresponding velocity model such that it produces a better focused image. Common Image Gathers (CIGs) are usually evaluated to asses the velocity model. CIGs can be defined as variations between partial images at a fixed image point [Biondi, 2006]. The flatness of the CIGs usually indicate a suitable velocity model that will generate a high quality image. However, if the CIGs are curved it is an indication that the velocity model is incorrect and subsequently the image will not be focused. Utilizing image domain methods enables updating the velocity model in more complex velocity structures with lateral velocity variations, since they make use of imaging to focus the events. The draw-

back lies in that extracting the kinematic information from the image is not straightforward. Furthermore, the nonlinear relationship between the image and the velocity poses a challenge in arriving at the correct solution.

Similar to MVA, Wave-Equation Migration Velocity Analysis (WEMVA) is an image domain velocity estimation method that uses the focusing capabilities of migration to extract the kinematic information [Symes and Kern, 1994; Sava and Biondi, 2004a,b]. However, WEMVA uses the wavepaths rather than rays to model the reflections, which take into account the broad range of frequencies involved. Furthermore, the wavepaths also take into account multipathing. As in the MVA case, the nonlinearity of WEMVA can hinder the convergence to the correct solution. Therefore, the Born scattering series is truncated to the first-order term in order to linearize the relationship between the velocity error and the image. A shortcoming of WEMVA is that this linearization of the Born series limits the method to primaries-only. Hence, multiples are considered as noise.

1.3.3 Full Waveform Inversion

Recently, we have seen a shift in the industry to utilize the full waveforms to automatically estimate the velocities. Full Waveform Inversion (FWI), which can be summarized as a reconstruction of the seismic experiment in our simulation tools [Tarantola, 1987; Virieux and Operto, 2009]. The reconstruction encompassing the proper description of the physics of wave-propagation in the subsurface, the acquisition geometry, and the medium parameters needed to obtain the synthetic data that resembles the observed data. FWI is generally considered to be a data domain method, where the objective is to minimize the error between the observed and calculated data sets. FWI methods are able to invert for the long-wavelength (smooth) components of the velocity as well as the short-wavelength (sharp) components. The long-wavelength component is encoded in the kinematic part of the wavefield. On the other hand, the short-wavelength (high resolution features) component is encoded in the amplitudes of the wavefield. Separation of the long- and short-wavelengths is not easily achievable in traditional FWI, consequently the method suffers from a high degree of nonlinearity. Therefore, FWI is applied in a hierarchical multi-scale approach where the low-frequencies of the transmitted and diving waves are first used to update the long-wavelength component of the model. Thereafter, higher-frequencies and more reflections come in to update

the short-wavelength component. Although theoretically feasible, in reality updating the long-wavelength is seldom achieved, since the low-frequencies are usually not recored in the data [Bunks et al., 1995]. Furthermore, the diving waves need to be recorded at very large offsets in order to update the deeper parts of the model [Pratt, 1999].

Nevertheless, methods from both the acquisition and the processing sides have been developed in order to mitigate these effects. From the acquisition side more low-frequency sources are being developed [Bagaini, 2006] as well as larger offsets being recorded to facilitate the acquisition of diving waves. Recently we have seen a survey where $50km$ offsets were recorded [Yang et al., 2016]. From the processing side numerous approaches have been developed that facilitate the convergence of FWI. Integrating MVA with FWI can help reduce the high degree of nonlinearity of the objective function [Biondi and Almomini, 2014; Alkhalifah and Wu, 2016]. Another promising approach is adaptive FWI [Warner and Guasch, 2014], which utilizes Wiener filters to match the observed and calculated data sets. Although, the velocity model estimated can be very detailed, it is usually smoothed and used as input for a linear depth migration method that does not utilize the velocity details.

1.4 Anisotropy

The seismic wave velocity usually changes with a change in the direction of propagation, in which the velocity is considered to be anisotropic. Velocity anisotropy is usually caused by a certain structure (order) at a much smaller scale than the dominant wavelength. Gerchka [2009] defines anisotropy on a macroscale as order heterogeneity on a microscale. Therefore, anisotropy and heterogeneity are closely related. For reflection seismology the frequencies that are used are generally in the tens of Hertz, therefore, the ordered microscale heterogeneity appears as effective anisotropy. In his classical paper Backus [1962] presents an effective-medium theory that represent this microscale heterogeneity as an effective medium that is more homogeneous and anisotropic. It can be used to calculate the effective anisotropy as done in Liner and Fei [2006]. The ordered microscale heterogeneities, or more appropriately anisotropy, can be caused by a plethora of different geologic scenarios [Tsvankin, 2012]:

- Intrinsic anisotropy due to preferred orientation of the mineral grains.

Shales exhibit this type of anisotropy due to their aligned plate-shaped clay particles [Banik, 1984; Thomsen, 1986].

- Thin bedding of isotropic layers on a small scale compared to the wavelength. This is the case for thin isotropic sedimentary layers with different properties, which is commonly encountered in the North Sea area [Levin, 1979].

- Vertical or dipping fractures, ordered fractures cause a preferred wave propagation [Schoenberg and Sayers, 1995]. This type of anisotropy becomes useful for fractured reservoirs where the predominant fracture direction needs to be identified in order to drill [Alshuhail, 2006].

- Nonhydrostatic stress [Nur and Simmons, 1969; Sarkar et al., 2003]. Uniaxial stress changes the elastic properties of certain rocks, which can cause velocity anisotropy, due to the microcracks.

Anisotropy manifests at different extents. The most generalized form of anisotropy is triclinic media. This type of anisotropy model is seldom used for seismic reflection imaging, due to the large number of variables needed to describe it. A more manageable and simpler type of anisotropy is Transversely Isotropic (TI) media [Alkhalifah, 1997]. It is arguably the most commonly used and studied type of anisotropy for seismic exploration [Tsvankin, 2012]. It is suitable for describing thinly bedded sedimentary sequences and for bedded shales of arbitrary dip. This is the type of anisotropy that will be mainly discussed in this thesis. A more detailed definition and explanation of these types of anisotropy is presented in chapter 2. However, for the time being we would like to examine how the anisotropic effects manifest in seismic data. Figure 1.8 shows a comparison between wavefronts in an isotropic medium and a TI medium, VTI with $\delta = -0.2$ and $\epsilon = 0.2$ [Thomsen, 1986], in polar coordinates. Note that the TI wavefront is no longer circular due to the variation of velocity with angle.

Ignoring seismic anisotropy, when present, causes mispositioning of reflectors and unfocused images in migration [Byun et al., 1989; Lynn et al., 1991]. This is because the wavefronts deviate from a sphere for homogeneous media, and assuming spherical wavefronts in imaging is no longer adequate. One needs to account for the true propagation effects to arrive at a well-focused image. To illustrate the effect of anisotropy on the kinematics, the model in figure 1.4 is updated to contain anisotropic coefficients in the second layer (VTI

with $\delta = 0.1$ and $\epsilon = 0.2$) as shown in figure 1.9a. Figure 1.9b shows a comparison between isotropic (red) and anisotropic (black) waveforms. The first reflection does not change, however, the second reflection has a different arrival time as a function of angle and offset. Also note that the multiples have different arrivals times as well. This is of particular interest, since they can be potentially used to help the inversion process in estimating the anisotropic parameters.

1.5 Multiples

Multiples are reflected events that have bounced more than once in the subsurface. If subsurface contrasts are large enough then multiples start to be more significant in the recorded data. The events that happen after $0.75s$ in figure 1.9b are all multiples. Multiples can be categorized in two cat-

a)

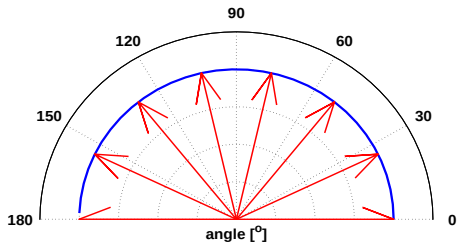

b)

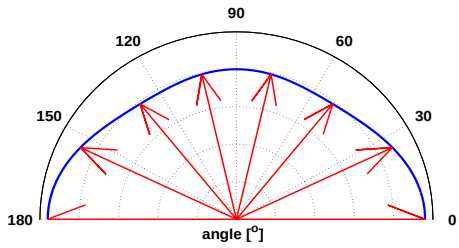

Figure 1.8: *The wavefronts for a) an isotropic medium b) an anisotropic medium.*

egories: Surface-related multiples and internal multiples. Surface-related multiples usually have larger energy than internal multiples, because they are reflected at the surface (reflectivity at the surface is approximately -1

a)

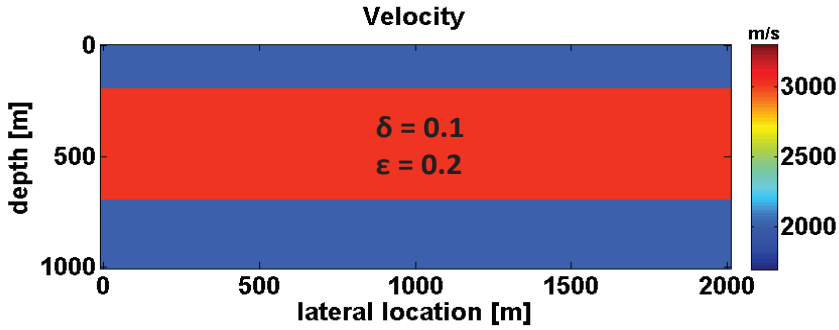

b)

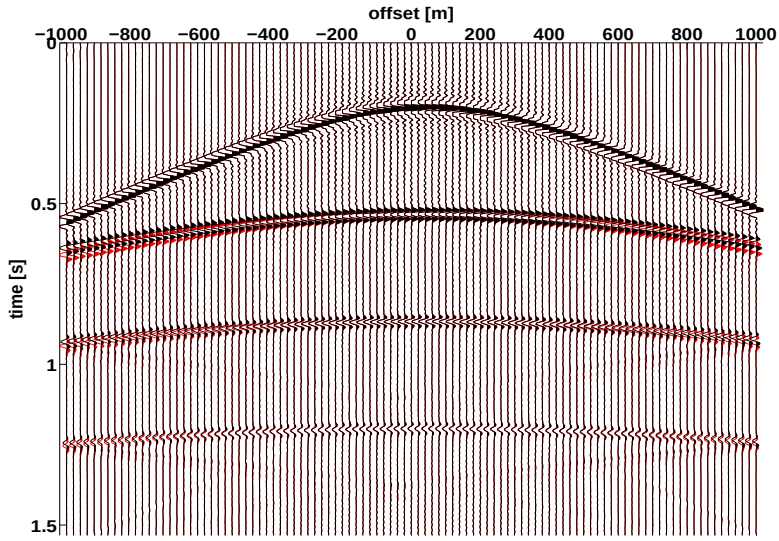

Figure 1.9: *a) An anisotropic model. b) The associated reflection data in black and the its isotropic counterpart in red.*

in the marine case). For the marine case with no shallow water, they are often removed from the seismic data via Surface-Related Multiple Elimination (SRME) [Verschuur et al., 1992; Verschuur, 2006]. The method works by predicting the surface-related multiples by data-driven convolutions and eliminating them via subtraction in an adaptive way. Internal multiples on the other hand are more difficult to eliminate, since the multiple generating surface is usually unknown. Nevertheless, there have been internal multiple elimination methods based on a prior information of the multiple generating surface. Examples include removal via the inverse scattering integral [Coates and Weglein, 1996; Matson and Weglein, 1996] or via the Internal Multiple Elimination (IME) method [Berkhout and Verschuur, 1999, 2000]. Removing multiples will always be sub-optimal since the acquisition geometries are neither dense enough nor are the multiple elimination algorithms efficient enough to handle the complete multiple coda.

Estimation of Primaries by Sparse Inversion (EPSI) uses the same fundamental equation as SRME, however, instead of estimating the multiples and iteratively subtracting them from the data, it estimates the primaries [van Groenestijn and Verschuur, 2009a,b]. Like SRME it is a data-driven method that does not require a subsurface model. Unlike SRME it does not require interpolating the data beforehand, if the near offsets are missing, since reconstruction is done simultaneously via the multiples. Furthermore, the source signature is also estimated since the parametrization was based on primary responses (spiked reflections) and the wavelet. Lopez and Verschuur [2015] propose a combination of SRME and EPSI, where the multiples are estimated in a closed-loop inversion approach similar to EPSI.

Recently however, there has been a drive to utilize multiples rather than eliminating them. Multiples generally spend more time in the subsurface, compared to primaries, therefore, have a higher vertical resolution of the subsurface parameters [Zhang and Schuster, 2013; Berkhout, 2014c; Zuberi and Alkhalifah, 2014; Berkhout and Verschuur, 2016]. Utilizing them also broadens the subsurface illumination and attenuates the effect of shadow zones [Davydenko and Verschuur, 2017], hence, providing a more balanced illumination of the subsurface [Kumar et al., 2014; Lu et al., 2015]. Another benefit that comes out of using internal multiples is that it enables imaging structures from below as shown by Davydenko and Verschuur [2013] and Davydenko and Verschuur [2017]. Different imaging conditions can be applied, since the incident field and scattered field are separable, to image the

reflector from above and below. A significant issue that arises when imaging with multiples is that an accurate velocity model is needed. Multiples are generally more sensitive to the velocity model because they spend more time in the subsurface compared to primaries. Therefore, the velocity model must be accurate in order to image the multiples correctly [Jiang et al., 2007].

1.6 Joint Migration Inversion

Obtaining an accurate reflectivity and velocity model of the subsurface is essential for seismic exploration. However, as we have seen in the previous sections, in order to obtain an accurate reflectivity model one needs an accurate velocity model, and vice versa. Joint Migration Inversion (JMI) proposed by Berkhout [2012, 2014c] and implemented by Staal and Verschuur [2012, 2013]; Staal [2015] inverts for these two parameters in a full waveform approach, such that both the dynamics and kinematics of the data are taken into account. The approach is based on parameterizing the modeling and inversion in terms of scattering and propagation operators (which can be translated into reflectivities and velocities, respectively). It is a data-driven full waveform approach that minimizes the error between the observed and modeled data in an iterative manner.

Perhaps the most significant and unique property of JMI is that it strictly separates scattering and phase information of the seismic measurements. The scattering information is encoded in the reflectivity operators while the phase information is encoded in the propagation operators. This strict separation enables the JMI method to decrease the degree of nonlinearity and, in turn mitigates the effect of cycle-skipping [Staal et al., 2014; Alshuhail and Verschuur, 2015; Berkhout et al., 2015; Verschuur et al., 2016].

JMI utilizes all types and orders of multiples, both surface and internal multiples. It was argued in the previous section that multiples generally spend more time in the subsurface and, therefore, are more sensitive to the subsurface parameters. Utilizing them also broadens the subsurface illumination and attenuates the effect of shadow zones. However, since they spend more time in the subsurface and have bounced multiple times they are usually weak when they are recorded. Finally, since the multiples are naturally explained in the forward model for JMI, their crosstalk is automatically modeled [Berkhout, 2014b; Davydenko and Verschuur, 2017]. By utilizing the joint

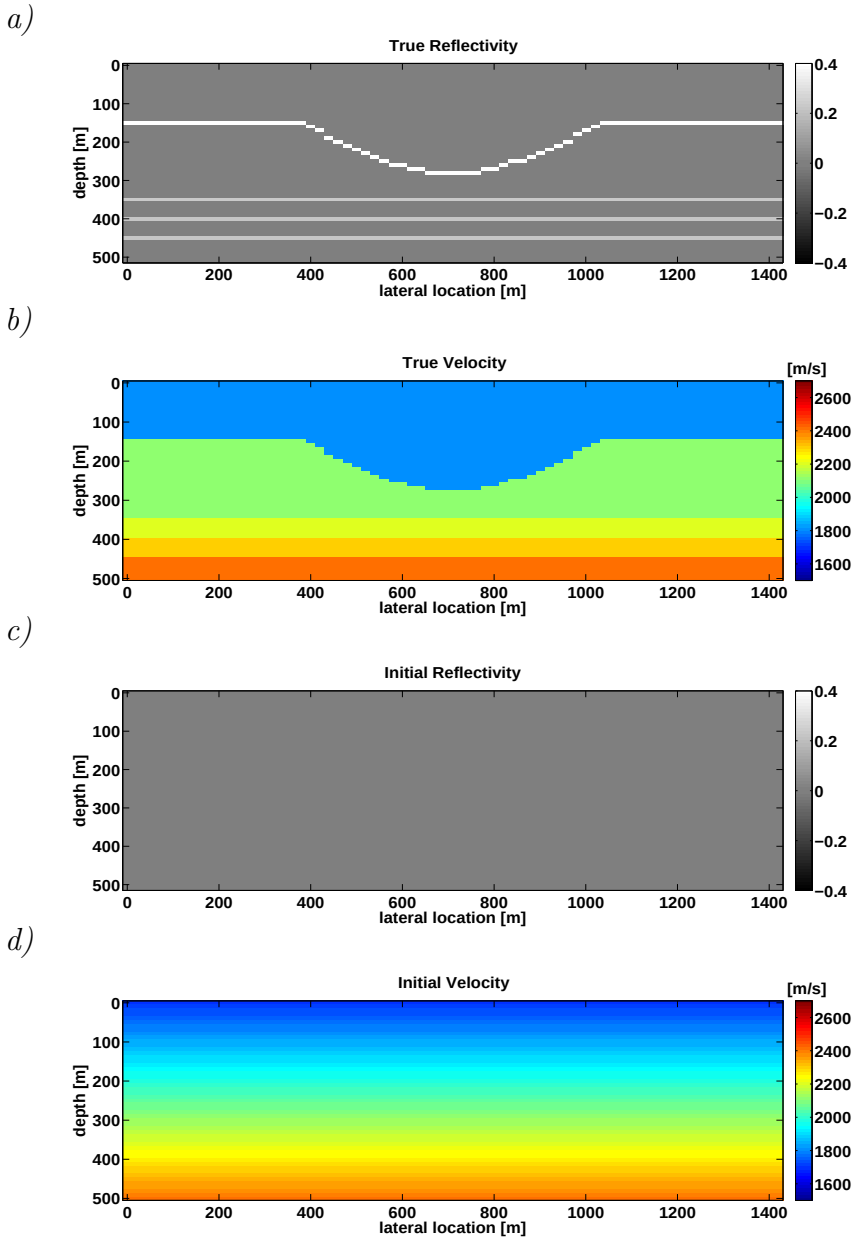

Figure 1.10: *The true values for a) the reflectivity and b) the velocity [m/s]. The initial values for c) the reflectivity and d) the velocity [m/s].*

a)

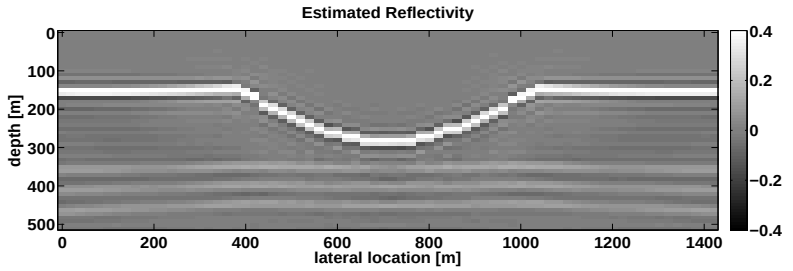

b)

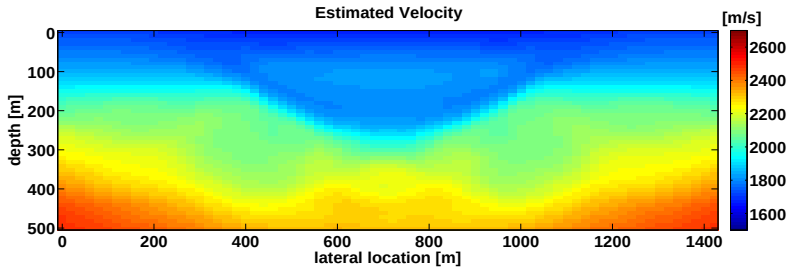

Figure 1.11: *The estimated values for a) the reflectivity and b) the velocity [m/s].*

inversion of reflectivity and velocity and including all multiples in a full waveform, data-driven way, JMI is able to produce a sharp reflectivity model and a smooth but accurate velocity model of the subsurface. Figures 1.10 and 1.11 illustrate the capability of JMI on a similar syncline model as the one presented in figure 1.2. Figures 1.10a and b show the true reflectivity and velocity models, while figures 1.10c and d show the initial reflectivity and velocity models. Figure 1.11 shows the estimated reflectivity and velocity after applying JMI.

In its current implementation JMI assumes the subsurface to be isotropic (velocity is not a function of propagation direction). However, in reality there are a plethora of geologic scenarios where anisotropy (velocity is a function of propagation direction) is evident and significant. In these cases ignoring anisotropy leads to poor results. Hence estimating and accounting

for anisotropy becomes essential [Alkhalifah and Tsvankin, 1995; Lee et al., 2010; Vigh et al., 2010]. Moreover, we have seen a shift in the seismic industry to obtain wide-azimuth and wide-aperture seismic data [Michell et al., 2006], where the anisotropic signatures are more evident compared to narrow azimuth surveys [Prieux et al., 2011]. Hence, taking anisotropy into account becomes essential to correctly explain the data at far offsets, and, thereby, create more accurate and reliable subsurface images.

1.7 Thesis Objective and Outline

The objective of this thesis is motivated by the presence of anisotropy. Clearly, we live in an anisotropic world (depending on the observers wavelength), therefore we should treat it as anisotropic. This thesis aims at incorporating anisotropic kinematics in the JMI scheme, in order to make JMI better applicable in realistic geologic settings.

We present a data-domain inversion-based imaging and anisotropic velocity analysis approach that utilizes primary reflections as well as multiple reflections, without any a priori information of the multiple generating boundaries. The method is flexible in that inaccurate starting models can be handled, where the strict separation of the reflectivity from the anisotropic velocity models promotes this flexibility. The method is relatively hands off in terms of user interference once the initial setup is defined. The remainder of this thesis consists of six chapters.

- Chapter 2 presents an overview of velocity anisotropy in reflection seismology. It provides the basic assumptions and the fundamental equations that will be used throughout this chapter. We then introduce JMI's modeling method Full Wavefield Modeling (FWMod) that utilizes integral operators to model the reflections. FWMod strictly separates the scattering information from the kinematics via the reflectivity and propagation operators respectively. We then include VTI kinematics in the propagation operators via replacing the dispersion relation with the acoustic anisotropic dispersion relation. We address some of the limitations of the acoustic anisotropic dispersion relation in order to increase the flexibility of the modeling method. We incorporate the anisotropic propagation operators in the FWMod scheme.

- Chapter 3 is split into two parts. In the first part we review a number of different parameterizations proposed for anisotropic inversion. After that we evaluate the cost function associated with chosen parameterization. Using the cost function we analyze the effects of including reflectivity estimation and the effects of internal multiples in inversion. We show that estimating the reflectivity reduces the nonlinearity and including internal multiples reduces the trade-off between the different parameters. In the second part we formulate the theory of anisotropic JMI. The method is data-driven in that we minimize the difference between the observed and calculated data sets in a least-squares sense. Since the nonlinearity is reduced (via estimating the best fit reflectivity) we optimize the method via a steepest decent approach. We derive the gradients associated with the different parameters and finally update the inversion strategy to accommodate anisotropic inversion.

- Chapter 4 illustrates the capabilities of anisotropic JMI on a number of different synthetic models. Each example attempts to isolate and show a specific property of anisotropic JMI. We first examine the effects of including anisotropy in inversion as opposed to ignoring it on lens-shaped model. We then demonstrate the method in updating all the parameters simultaneously (reflectivity and anisotropic velocity) for a simple model. Next, we test the method in converging for exceedingly poor initial models. After that we investigate the elastic effects in inversion. Subsequently, we examine the effect of internal multiples in updating the parameters on a model that generates strong internal multiples. Finally, we validate the method on a realistic synthetic model (the HESS VTI model) that resembles Gulf of Mexico geology.

- Chapter 5 shows the application of the method on marine data from the Viking Graben in the North Sea. We illustrate the effectiveness of the method in estimating the reflectivities and the anisotropic velocities. We corroborate our inverted results via examining the Angle-Domain Common Image Gathers (ADCIGs).

- Chapter 6 extends the method towards TTI media. As in the VTI case we first update the modeling engine to include TTI kinematics. We then include TTI kinematics in the imaging engine of JMI, Full Wavefield Migration (FWM). FWM includes, besides transmission effects, internal multiples in imaging. Therefore, we examine the effect

of internal multiples in imaging a TTI medium. Finally, we analyze the effect of errors in the different TTI parameters on the image quality.

- In Chapter 7 we present our main conclusions and our recommendations for future research.

2

Anisotropic Full Wavefield Modeling

Only in the last two decades anisotropy has become an important and recognizable topic in seismic exploration. Perhaps the reason for the delay lies in that isotropy is simpler. The basic idea of isotropy is obvious and the fundamental equations are straightforward compared to the complex ideas behind anisotropy and the abstruse equations associated with it. However, with recent advancements in acquisition and the expected efficiency of hydrocarbon exploration and production monitoring we must move beyond an isotropic view on the Earth and welcome an anisotropy view of it. The first part of this chapter presents an overview of anisotropy in seismic exploration. This will provide the basic building blocks for the modeling and inversion theories in later chapters.

The second part presents JMI's unique modeling method, Full Wavefield Modeling (FWMod). It is unique in that it does not solve the wave-equation but rather utilizes integral operators. These operators enable the distinction between the kinematics and dynamics, which will play an imperative role in inversion. Afterwards, anisotropic kinematics will be incorporated in the modeling scheme in a relatively straightforward manner.

2.1 Theory of Anisotropy in Seismic Exploration

2.1.1 Anisotropic Parameters

For elastic media stress is linearly related to strain through Hooke's law:

$$\tau_{ij} = C_{ijmn} E_{mn}, \tag{2.1.1}$$

where τ_{ij} is the stress tensor, E_{mn} is the strain tensor, and C_{ijmn} is a 3x3x3x3 tensor that describes the elasticity [Aki and Richards, 1980; Wapenaar and Berkhout, 1989]. In order to simplify notation and manipulation, we use the elasticity tensor representation given by a 6x6 matrix according to the Voigt scheme [Thomsen, 2002]. The C_{ijkl} matrix can be written as:

$$\mathbf{C}^{(trc)} = \begin{bmatrix} C_{11} & C_{12} & C_{13} & C_{14} & C_{15} & C_{16} \\ C_{12} & C_{22} & C_{23} & C_{24} & C_{25} & C_{26} \\ C_{13} & C_{23} & C_{33} & C_{34} & C_{35} & C_{36} \\ C_{14} & C_{24} & C_{34} & C_{44} & C_{45} & C_{46} \\ C_{15} & C_{25} & C_{35} & C_{45} & C_{55} & C_{56} \\ C_{16} & C_{26} & C_{36} & C_{46} & C_{56} & C_{66} \end{bmatrix}. \tag{2.1.2}$$

This is the most general anisotropic model, it has 21 independent stiffness coefficients. Materials that exhibit this type of anisotropy are referred to as triclinic. The large number of independent variables hinders its application in seismology [Tsvankin, 2012].

Fortunately, many geologic scenarios contain a plane of mirror symmetry [Winterstein, 1990]. If the geology contains a plane of mirror symmetry, it is possible to arrive at an elasticity matrix with a reduction in the number of independent variables. Orthorhombic media are systems that have three orthogonal planes of mirror symmetry, the number of independent parameters in the stiffness matrix greatly reduces to nine. In practice, sedimentary sequences with two or three orthogonal fracture systems can be described as orthorhombic. The stiffness matrix for orthorhombic media can be written as:

$$\mathbf{C}^{(ort)} = \begin{bmatrix} C_{11} & C_{12} & C_{13} & 0 & 0 & 0 \\ C_{12} & C_{22} & C_{23} & 0 & 0 & 0 \\ C_{13} & C_{23} & C_{33} & 0 & 0 & 0 \\ 0 & 0 & 0 & C_{44} & 0 & 0 \\ 0 & 0 & 0 & 0 & C_{55} & 0 \\ 0 & 0 & 0 & 0 & 0 & C_{66} \end{bmatrix}. \tag{2.1.3}$$

Transversely isotropic media are a special case of orthorhombic media, with a more simplified description. TI media can be defined as having one axis of symmetry, where the media is invariant to any rotation around this axis. An example would be thinly dipping bedded sequences, such as shales. Furthermore, the angle of the symmetry axis classifies the type of TI media. Having non-vertical symmetry axis defines the medium as Tilted Transverse Isotropy (TTI), which is the case for the flanks of salt diapirs and dipping shale sequences. On the other hand having vertical symmetry axis defines the media as Vertical Transpose Isotropy (VTI), which is the case for thinly bedded sedimentary sequences and for horizontally bedded shales. The number of independent parameters reduces to five and the stiffness matrix for VTI media is given by:

$$\mathbf{C}^{(VTI)} = \begin{bmatrix} C_{11} & (C_{11}-2C_{66}) & C_{13} & 0 & 0 & 0 \\ (C_{11}-2C_{66}) & C_{11} & C_{13} & 0 & 0 & 0 \\ C_{13} & C_{13} & C_{33} & 0 & 0 & 0 \\ 0 & 0 & 0 & C_{44} & 0 & 0 \\ 0 & 0 & 0 & 0 & C_{44} & 0 \\ 0 & 0 & 0 & 0 & 0 & C_{66} \end{bmatrix}. \tag{2.1.4}$$

In this thesis chapters 2 through 5 will focus on the VTI case and chapter 6 will focus on the TTI case. Figure 2.1a shows a schematic representation of a VTI model, while figure 2.1b shows a schematic representation of a TTI model. Not that the difference lies in the symmetry axis.

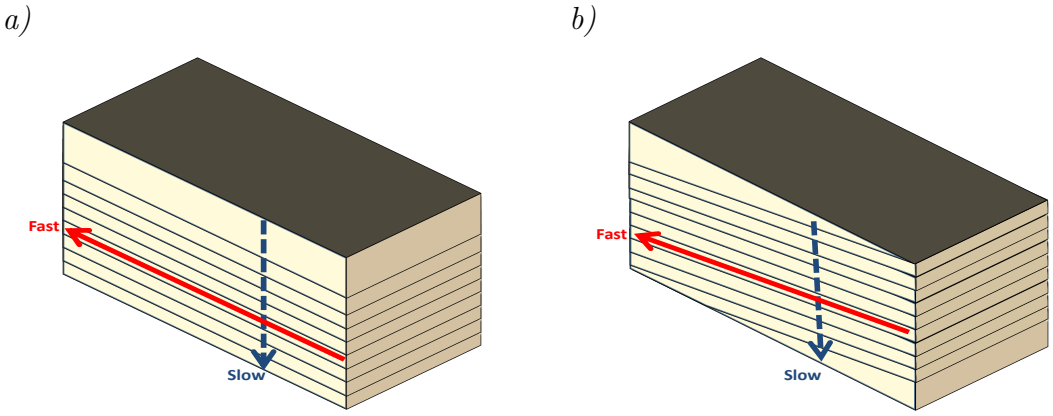

Figure 2.1: *Schematic representation of a) a VTI medium and b) a TTI medium.*

For completeness' sake, the stiffness matrix for isotropic media is given as:

$$\mathbf{C}^{(iso)} = \begin{bmatrix} \lambda+2\mu & \lambda & \lambda & 0 & 0 & 0 \\ \lambda & \lambda+2\mu & \lambda & 0 & 0 & 0 \\ \lambda & \lambda & \lambda+2\mu & 0 & 0 & 0 \\ 0 & 0 & 0 & \mu & 0 & 0 \\ 0 & 0 & 0 & 0 & \mu & 0 \\ 0 & 0 & 0 & 0 & 0 & \mu \end{bmatrix}, \tag{2.1.5}$$

where λ and μ are Lamé's constants with $C_{44} = C_{55} = C_{66} = \mu$, $C_{12} = C_{13} = C_{23} = \lambda$, and $C_{11} = C_{33} = \lambda + 2\mu$. They can be directly equated to the P-wave velocity V_p and the S-wave velocity V_s via:

$$V_p = \sqrt{\frac{\lambda+2\mu}{\rho}}, \tag{2.1.6}$$

and

$$V_s = \sqrt{\frac{\mu}{\rho}}, \tag{2.1.7}$$

where ρ is the density.

The choice of parametrization is of utmost importance in multiparameter inversion problems [Menke, 2012]. Traditionally, anisotropy was parametrized in terms of stiffness coefficients. However, the stiffness coefficients parametrization is not ideal to describe seismic wavefields in anisotropic media. The stiffness coefficients do neither give immediate insight on wave-propagation properties nor on the strength of anisotropy. In his iconic paper Thomsen [1986] proposed a different parametrization that relates anisotropy immediately to wave-propagation. He suggested describing anisotropy using the P- and S-wave velocities along the symmetry axis and three dimensionless parameters. The dimensionless parameters are:

- ϵ: the fractional difference between the horizontal and vertical P-wave velocities. It is given by:

$$\epsilon \equiv \frac{C_{11} - C_{33}}{2C_{33}} \ , \tag{2.1.8}$$

- γ: the fractional difference between the horizontal and vertical S-wave velocities. It is given by:

$$\gamma \equiv \frac{C_{66} - C_{44}}{2C_{44}} \ , \tag{2.1.9}$$

- δ: is responsible for the curvature or angular dependence of the P-wave velocity in the vicinity of the symmetry axis. It is given by:

$$\delta \equiv \frac{(C_{13} + C_{44})^2 - (C_{33} - C_{44})^2}{2C_{33}(C_{33} - C_{44})} \ . \tag{2.1.10}$$

The Thomsen parameters vanish for the case of isotropy. Hence, they can be a good measure to estimate the strength of anisotropy. They also bring immediate insight regarding the effects of anisotropy on wave propagation. Moreover, it is possible to equate the Thomsen parameters to different measurable velocities in seismic exploration. One crucial parameter that is estimated in almost all surface seismic experiments is the normal moveout

velocity, abbreviated as V_{nmo}. It can be expressed by the P-wave velocity along the symmetry axis and δ parameter via:

$$V_{nmo} = V_v\sqrt{1+2\delta}. \tag{2.1.11}$$

The δ parameter dictates how far or how close the NMO velocity is to the vertical velocity. If the medium has a non-zero δ and if one were to use the NMO velocity to estimate depths, one will definitely arrive at an erroneous depth. Another important parameter is the horizontal velocity V_h, which can be expressed by the P-wave velocity along the symmetry axis and the ϵ parameter via:

$$V_h = V_v\sqrt{1+2\epsilon}. \tag{2.1.12}$$

These relations make the Thomsen parameterization attractive to describe anisotropy. Note that although the Thomsen parameters were introduced in the context of the weak anisotropy approximation, they are convenient for use regardless of the magnitude of anisotropy as shown by Tsvankin [2012]. If we consider P-wave kinematics only, we find that they are insensitive to the S-wave along the symmetry axis and γ in the VTI case, hence, the number of parameters needed to describe it further reduces to three, namely V_v, δ, and ϵ [Alkhalifah, 1998]. Moreover, for time processing the number of parameters further reduces to two, namely V_{nmo} and a new parameter η [Alkhalifah and Tsvankin, 1995]. η is defined as the anellipticity, it quantifies the deviation of the travel-time function from a hyperbola. It is given as:

$$\eta = \frac{\epsilon-\delta}{1+2\delta} = \frac{V_h^2 - V_{nmo}^2}{2V_{nmo}^2}. \tag{2.1.13}$$

We analyze the kinematic effects of the different Thomsen parameters on the P-wave wavefront. Figure 2.2a shows the P-wave wavefront for the isotropic case while figures 2.2b-f show the P-wave wavefront for a number of different anisotropic scenarios. Note that many of scenarios are not commonly encountered in the subsurface. However, these examples provide insights on how the Thomsen parameters affect wave propagation.

2.1.2 Acoustic Anisotropic Dispersion Relation

Anisotropy normally does not exist in acoustic media (except for the special case of elliptic anisotropy). Therefore, full elastic modeling is needed to accurately model the anisotropic kinematics. However, due to the complexity and computational cost involved with full elastic modeling, a simple alternative was desired. Alkhalifah [2000] derived an acoustic wave-equation for VTI media, which was done by setting the vertical shear velocity to zero in the stress-strain relation then deriving the wave-equation. The dispersion relation is the kernel for the anisotropic wave-equation, which can be written as:

$$k_z^2 = \frac{V_{nmo}^2}{V_v^2}\left(\frac{\omega^2}{V_{nmo}^2} - \frac{\omega^2 k_x^2}{\omega^2 - 2V_{nmo}^2\eta k_x^2}\right) , \tag{2.1.14}$$

where k_z is the vertical wavenumber, ω is the angular frequency, and k_x is the horizontal wavenumber. Using the identities in equations 2.1.11 and 2.1.12 it is possible to rewrite the dispersion equation in terms of V_v, δ, and V_h:

$$k_z^2 = \frac{\omega^2}{V_v^2} - \left(\frac{\omega^2(1+2\delta)k_x^2}{\omega^2 - V_h^2 k_x^2 + V_v^2(1+2\delta)k_x^2}\right) . \tag{2.1.15}$$

The acoustic anisotropic dispersion relation will introduce VTI kinematics. However, one needs to note that the acoustic anisotropic dispersion relation has limitations if one were to use it directly. Two limitations were documented by Alkhalifah [2000] when deriving the anisotropic acoustic wave-equation. The first one was a pseudo S-wave (diamond shaped shear wave mode) that manifested if the source or receivers were in or near anisotropic media (figure 2.4a). The second limitation was an exponentially increasing solution for negative values of η. For the first limitation, which was the pseudo S-wave, he proposed placing the sources and receivers in an isotropic layer, where the pseudo S-wave does not manifest itself. As for the second limitation Alkhalifah [2000] concluded that this equation is not suitable for negative values of η due to the exponential growth in solution. It is possible to place the sources and receivers in an isotropic layer and avoid models with negative η. However, this limits the applicability of the dispersion relation. Grechka et al. [2004] studied the pseudo S-wave in more detail and showed that the pseudo S-waves are ironically SV-waves that propagate in acoustic VTI media.

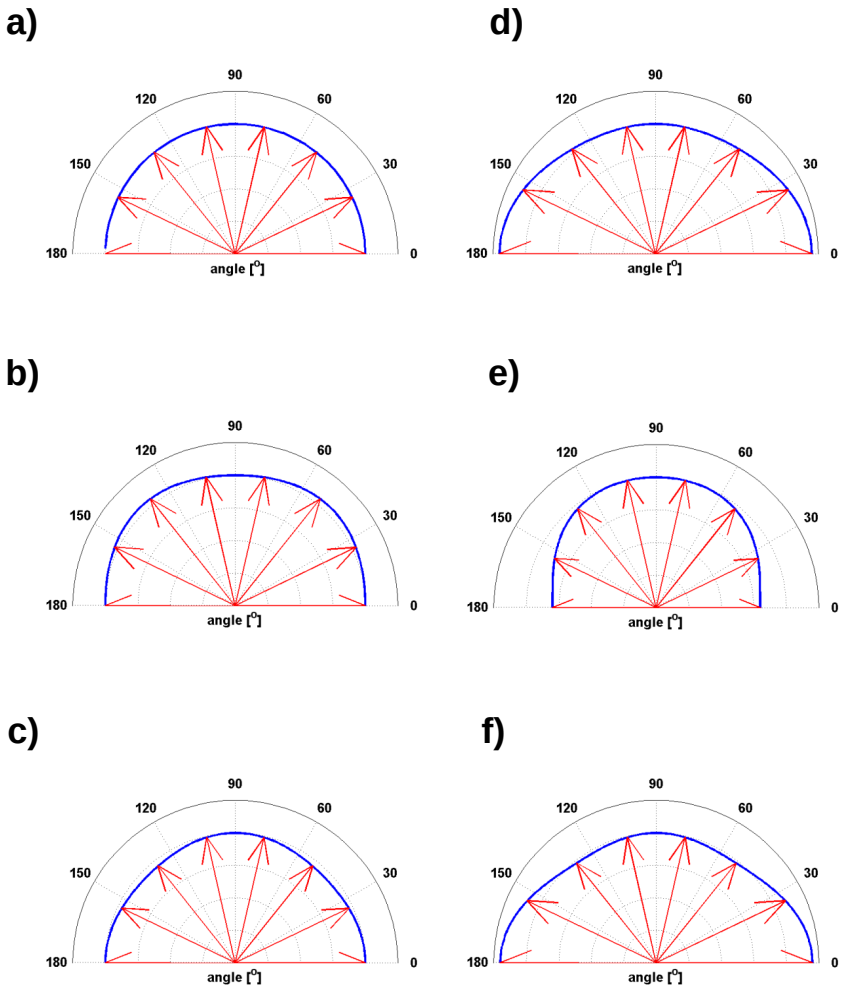

Figure 2.2: *P-wave wavefront. a) For the isotropic case, where* $V = 2000$ *[m/s]. b) For the anisotropic case, where* $V_v = 2000$ *[m/s],* $\delta = 0.2$*, and* $\epsilon = 0$*. c) For the anisotropic case, where* $V_v = 2000$ *[m/s],* $\delta = -0.2$*, and* $\epsilon = 0$*. d) For the anisotropic case, where* $V_v = 2000$ *[m/s],* $\delta = 0$*, and* $\epsilon = 0.2$*. e) For the anisotropic case, where* $V_v = 2000$ *[m/s],* $\delta = 0$*, and* $\epsilon = -0.2$*. f) For the anisotropic case, where* $V_v = 2000$ *[m/s],* $\delta = -0.2$*, and* $\epsilon = 0.2$*.*

a)

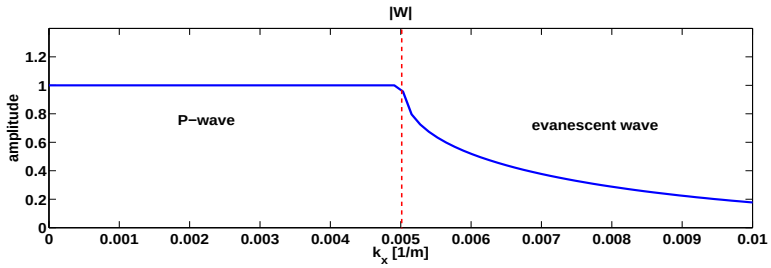

b)

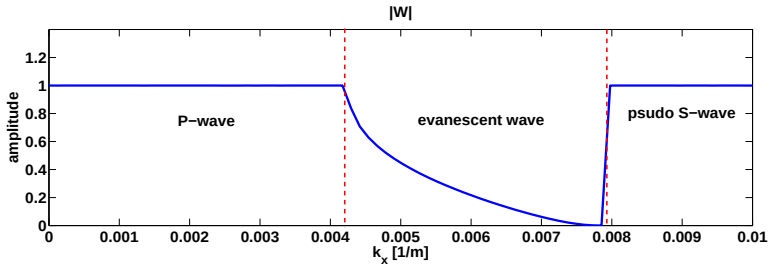

c)

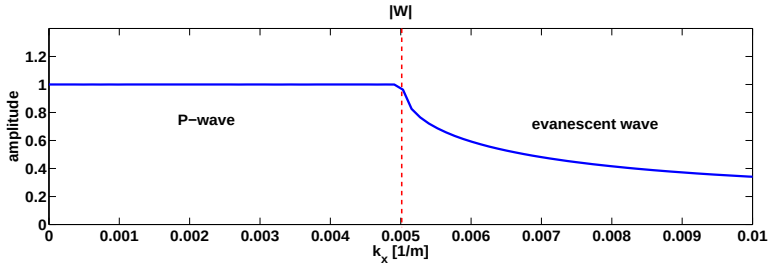

Figure 2.3: *A slice of the amplitude spectrum of the phase shift operator at* $10Hz$ *for: a) An isotropic medium with* $V = 2000m/s$. *b) A VTI medium with* $V_v = 2000$, $\epsilon = 0.2$, *and* $\delta = 0$ $(\eta > 0)$. *Note that it is possible to clearly distinguish and eliminate the pseudo S-wave in this domain. c) a VTI medium with* $V_v = 2000$, $\epsilon = 0$, *and* $\delta = 0.2$ $(\eta < 0)$.

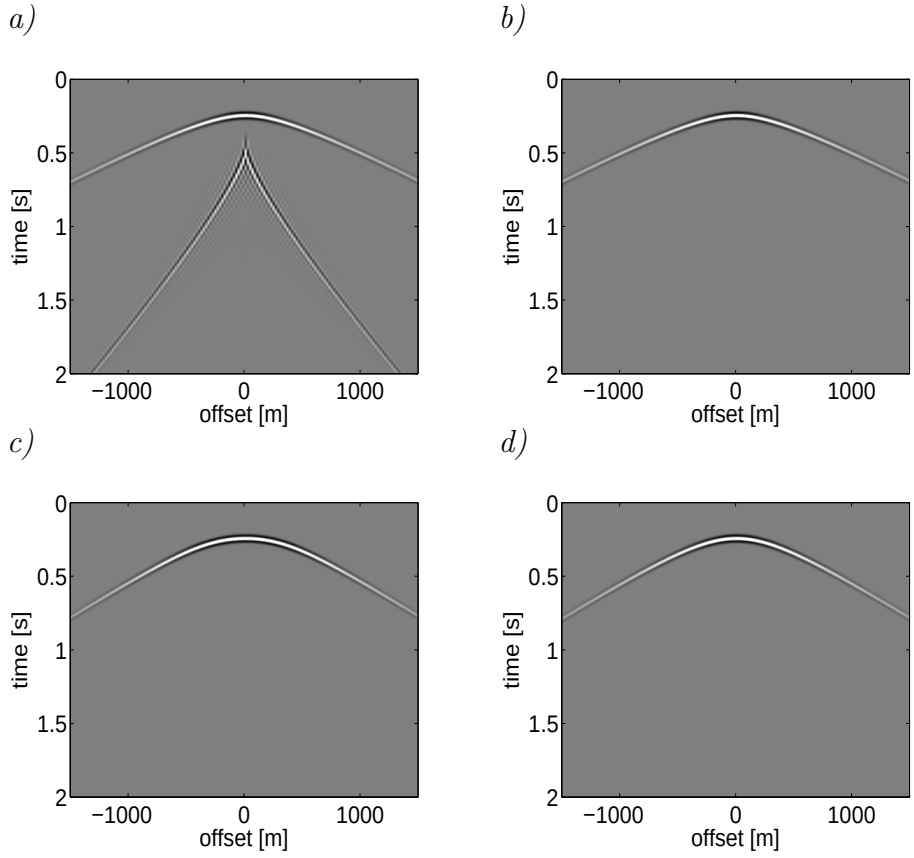

Figure 2.4: *a) Modeled wavefields in a VTI medium with $V_v = 2000m/s$, $\epsilon = 0.2$, and $\delta = 0$ ($\eta > 0$), note the diamond shaped event that corresponds to the pseudo S-wave. b) Suppressing the pseudo S-wave using the same model as in a). c) Modeled wavefield in a VTI medium with $V_v = 2000m/s$, $\epsilon = 0$, and $\delta = 0.2$ ($\eta < 0$). Note the different curvature at the apex. d) Modeled wavefield in an isotropic medium with $V_v = 2000m/s$ for comparison.*

A number of different methods were developed to eliminate the pseudo S-wave for finite-difference modeling [Fei and Liner, 2008; Duveneck et al., 2008]. However, these methods are neither straightforward to implement nor do they solve the issue of negative values of η. These limitations can be alleviated when using phase shift extrapolation [Bale, 2007]. For the first limitation, the pseudo S-wave, two propagating waves manifest in the extrapolator for $\eta > 0$. These propagating waves were attributed to the P-wave and pseudo S-wave. As a reference, figure 2.3a shows the absolute value of the phase shift operator at $10Hz$ in an isotropic medium with $V = 2000m/s$. There are two distinct regions attributed towards the propagating P-wave and the evanescent wave. Figure 2.3b shows the absolute value of the same phase shift operator at $10Hz$, however, in a VTI medium with $V_v = 2000$, $\epsilon = 0.2$, and $\delta = 0$ ($\eta > 0$). We notice three distinct regions, the propagating P-wave, the evanescent wave, and an extra propagating wave attributed to the pseudo S-wave. The extra propagating wave can be clearly distinguished in the extrapolation operator. Bale [2007] suggested writing the anisotropic dispersion relationship as:

$$k_z^2 = \frac{\omega^2}{V_v^2}\left(\frac{A}{B}\right) \ , \tag{2.1.16}$$

where $A = \omega - V_{nmo}^2\left(1 + 2\eta\right)k_x^2$ and $B = \omega - 2V_{nmo}^2\eta k_x^2$. If A and B are both positive then we get the propagating P-wave. However, if A or B is negative we get the evanescent wave. Finally, if A and B are both negative, we get another propagating wave, which was attributed to the pseudo S-wave. Therefore, it is possible to eliminate the pseudo S-wave by muting the result when $A \leq 0$ and $B \leq 0$.

We have noticed that it is common practice to eliminate the pseudo S-wave in finite-difference modeling by placing the sources and receivers in an isotropic region. We tested the technique for surface seismic acquisition and we noticed that we do not get the pseudo S-wave in the data because the pseudo S-wave does not propagate in the isotropic layer. However, this sets a limitation that the near surface should be isotropic. This also limits the extension of the method to Vertical Seismic Profile (VSP) geometries where the receivers can be located in an anisotropic layer. Finally, the pseudo S-waves can be converted back to a P-wave in the isotropic layer as shown by Grechka et al. [2004]. Therefore, we prefer eliminating the pseudo S-wave in the phase shift operator, even if the near surface is isotropic. This avoids converted waves

from the pseudo S-wave and provides flexibility in extending the method to VSP geometries. Figures 2.4a and 2.4b show the suppression of the pseudo S-wave in the x-t domain for the same anisotropic model as in figure 2.3b. Note that the P-wave kinematics are not affected.

As for the second limitation, which is the exponential growth of solution for negative values of η, we notice that the phase shift operators do not suffer from this instability. Bale [2007] shows that by having control of the sign of the exponent in phase shift operators it is possible to ensure evanescent decay, even for $\eta < 0$. Figure 2.3c shows the absolute value of the phase shift operator at $10Hz$ in a VTI medium with $V_v = 2000m/s$, $\epsilon = 0$, and $\delta = 0.2$ ($\eta < 0$). Figure 2.4c shows the modeled wavefield in the x-t domain, while figure 2.4d shows the isotropic case. Note that the curvature near the apex is different, although the flanks of the wave arrive at almost the same time (due to $\epsilon = 0$).

2.2 Full Wavefield Modeling in VTI media

Full Wavefield Modeling (FWMod) is an integral based approach that models reflection type events [Berkhout, 2012, 2014b; Davydenko and Verschuur, 2013, 2017]. It explains the seismic reflection response in terms of two independent operators, a scattering operator denoted by $\mathbf{R}$ and a local propagation operator denoted by $\mathbf{W}$. $\mathbf{R}$ contains the reflection information of the subsurface while the kinematics of wave propagation (velocity and anisotropy) is encoded in the $\mathbf{W}$ operators. Using $\mathbf{R}$ and $\mathbf{W}$ we can model primary, internal multiple, and surface-related multiple reflections. It consists of two main operations that are done sequentially, scattering and extrapolation. Note that the vector and matrix notation used in this chapter is the same notation introduced by Berkhout [1980]. It describes wavefields as a function of space for one frequency component as a vector.

Our modeling derivation and its subsequent implementations are for the 2D case. Taking a 2D assumption simplifies the equations and substantially reduces the computational cost involved. However, for complex 3D structures in subsurface a 2D assumption is not enough and out of plane reflections can cause discrepancies. Theoretically, the method can be extended to the 3D case as done by Marhfoul and Verschuur [2016] for the isotropic JMI case and [Davydenko and Verschuur, 2017] for the isotropic FWM case. The

complexity lies in optimizing the algorithms to handle the large amount of data being recorded as well as in compensating for the sparse and irregular spatial sampling of many 3D surveys in imaging and velocity estimation.

2.2.1 Scattering

To illustrate the method, assume a set of scatterers in the subsurface along a depth level z_m (figure 2.5). That depth level can have two wavefields approaching it, namely a downgoing wavefield, represented by $\vec{P}^+(z_m; z_s)$, and an upgoing wavefield, represented by $\vec{P}^-(z_m; z_s)$, where z_s refers to the location of the source that created these wavefields. The outgoing wavefields just above, represented by $\vec{Q}^-(z_m; z_s)$, and below, represented by $\vec{Q}^+(z_m; z_s)$, are given by:

$$\vec{Q}^-(z_m; z_s) = \mathbf{R}^{\cup}(z_m)\vec{P}^+(z_m; z_s) + \mathbf{T}^-(z_m)\vec{P}^-(z_m; z_s), \tag{2.2.17}$$

and

$$\vec{Q}^+(z_m; z_s) = \mathbf{T}^+(z_m)\vec{P}^+(z_m; z_s) + \mathbf{R}^{\cap}(z_m)\vec{P}^-(z_m; z_s). \tag{2.2.18}$$

In these equations $\mathbf{R}^{\cup}$ and $\mathbf{R}^{\cap}$ are the reflectivity operators acting from above and below, respectively. Similarly, $\mathbf{T}^+$ and $\mathbf{T}^-$ are the transmission operators acting from above and below, respectively. The transmission operator is defined as $\mathbf{T} = \mathbf{I}+\delta\mathbf{T}$, where $\delta\mathbf{T} \approx \mathbf{R}$ for small S-wave contrasts. Substituting this expression we get:

$$\vec{Q}^-(z_m; z_s) = \vec{P}^-(z_m; z_s) + \delta\vec{S}(z_m; z_s) \tag{2.2.19}$$

$$\vec{Q}^+(z_m; z_s) = \vec{P}^+(z_m; z_s) + \delta\vec{S}(z_m; z_s)\ , \tag{2.2.20}$$

where

$$\delta\vec{S}(z_m; z_s) = \mathbf{R}^{\cup}(z_m)\vec{P}^+(z_m; z_s) + \mathbf{R}^{\cap}(z_m)\vec{P}^-(z_m; z_s), \tag{2.2.21}$$

with $\delta\vec{S}$ being defined as the secondary sources along the depth level z_m. Note that the scattering and propagation are strictly separated, hence, the transmission effects are included in the scattering and not in the propagation. In

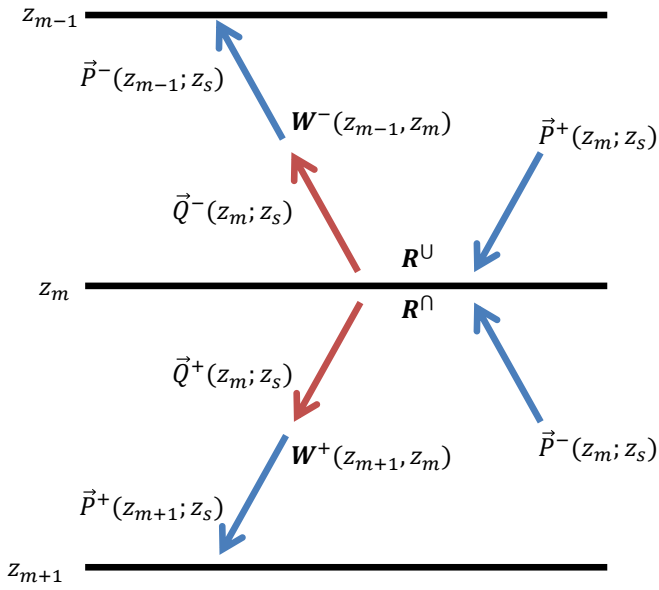

Figure 2.5: *Schematic representation of the incoming and outgoing wavefields acting on a scattering depth level z_m.*

this formulation the reflectivity $\mathbf{R}$ can be parametrized as angle-independent or angle-dependent. For the angle-independent case the reflectivity matrix $\mathbf{R}$ is a diagonal matrix with scalar coefficients. In order to reduce the number of parameters we assume that $\mathbf{R}^{\cup} = -\left[\mathbf{R}^{\cap}\right]^T$.

Anisotropy not only affects the traveltimes but also has an influence on the polarization and amplitudes of the seismic waves [Rüger, 2002]. The angle-dependent effects manifest as off diagonal components in the reflectivity operator as described in de Bruin et al. [1990] and in Berkhout [1997]. Not only does one need to analyze the off-diagonal components of the reflectivity, but also needs to go beyond the 2D assumption and into a 3D assumption in order to correctly describe polarizations and amplitudes. Davydenko and Verschuur [2017] incorporate angle-dependent reflectivity in the images of FWM by making use of the linear Radon domain. However, for this thesis

the reflectivity is assumed to be angle-independent. For the 2D case this means that the angle-independent reflectivity is given as ($i = 1, 2, ..., I$):

$$\mathbf{R}^{\cup}(z_m) = diag\left(R(x_1, z_m), R(x_2, z_m), ..., R(x_i, z_m), ...R(x_I, z_m)\right), \quad (2.2.22)$$

with $R(x_i, z_m)$ being the angle-dependent reflectivities at x_i and depth level z_m. The angle-independent reflectivities will only provide structural knowledge of the subsurface.

2.2.2 Extrapolation

Extrapolating the outgoing wavefields $\vec{Q}^{-}(z_m; z_s)$ and $\vec{Q}^{+}(z_m; z_s)$ to the next scattering depth level is done via the operator $\mathbf{W}(z_{m+1}, z_m)$. $\mathbf{W}(z_{m+1}, z_m)$ is a forward propagation operator. Each column is associated with the derivative of Green's function dictating wave propagation from one depth level z_m to the next z_{m+1}. For the 2D isotropic homogeneous case the scalar expression can be defined as [Berkhout, 1980; Wapenaar and Berkhout, 1989]:

$$\vec{W}(z_{m+1}, z_m) = \mathcal{F}_x^{-1}\left[e^{-jk_z\Delta z}e^{-jk_x x_s}\right], \quad (2.2.23)$$

where $\Delta z = |z_{m+1} - z_m|$, x_s is the source position of the Green's function, and $\mathcal{F}_x^{-1}$ indicates taking the inverse spatial Fourier transform and organizes the result in a vector. The isotropic dispersion relation is given as:

$$\begin{aligned} k_z &= \sqrt{k^2 - k_x^2} \qquad for \qquad |k_x| \leq |k| \\ k_z &= -j\sqrt{k_x^2 - k^2} \qquad for \qquad |k_x| > |k|, \end{aligned} \quad (2.2.24)$$

where $k = \frac{\omega}{V}$, ω is the angular frequency, and V is the isotropic P-wave velocity. For heterogeneous media the local velocity is used to evaluate each column of the propagation operator, however, this assumes that the velocity model is smooth. It is possible to relax this constraint and extend the method to handle more prominent laterally changing velocity models, as done in Hammad and Verschuur [2016]. Also note that the superscripts indicate the direction of extrapolation, where $\mathbf{W}^{+}$ indicates a downward extrapolation operator and $\mathbf{W}^{-}$ indicates an upward extrapolation operator. They are related to each other via $\mathbf{W}^{+}(z_{m+1}, z_m) = [\mathbf{W}^{-}(z_m, z_{m+1})]^T$.

In order to include VTI kinematics we need to substitute the isotropic dispersion relation (equation 2.2.24) with the anisotropic dispersion relation (equation 2.1.15) and apply the remedies described in the previous subsection (2.1.2). Utilizing FWMod and the **W** operators provides us with an immense advantage over other modeling methods in terms of choosing any desired VTI model (even for negative η) and the ability to directly eliminate the pseudo S-wave rather than having it implicitly there.

We base our modeling engine on an anisotropic acoustic approximation of the subsurface, although its validity is questionable when comparing it with real elastic data. Full elastic modeling requires much more parameters to describe it and subsequently more parameters to invert for. Hence, an accurate starting model is essential for inversion in order to avoid the null space. Starting with an acoustic approximation can help identify and estimate the essential parameters for subsequent inversion. Moreover, three or sometimes four component data is required for elastic inversion. Frequently, single component pressure or vertical displacement data are all that is recorded. Therefore, in this thesis, we assume that the data we are dealing with mainly consists of P-wave arrivals. We also assume that the contrasts are relatively weak. Hence, the S-wave and converted waves are weak. Furthermore, if the elastic effects are prominent we will rely on preprocessing that mitigates the elastic effects.

2.2.3 Forward Modeling Equations

Combining the scattering and extrapolation operations, we arrive at the governing equations for FWMod [Berkhout, 2014a]. For downgoing wavefields ($m = 1, 2, ..., M$):

$$\vec{P}^{+}(z_m; z_0) = \mathbf{W}^{+}(z_m, z_0)\vec{S}(z_0) + \sum_{k=0}^{m-1} \mathbf{W}^{+}(z_m, z_k)\delta\vec{S}(z_k; z_0), \qquad (2.2.25)$$

for upgoing wavefields ($m = 0, 1, ..., M-1$):

$$\vec{P}^{-}(z_m; z_0) = \mathbf{W}^{-}(z_m, z_M)\vec{P}^{-}(z_M; z_0) + \sum_{k=m+1}^{M} \mathbf{W}^{-}(z_m, z_k)\delta\vec{S}(z_k; z_0). \qquad (2.2.26)$$

$\vec{S}(z_0)$ represents the source wavefield generated at the surface level. Note that $\mathbf{W}^+$ and $\mathbf{W}^-$ are the upgoing and downgoing VTI one-way scatter free-operators, respectively. The modeling is done iteratively in so-called roundtrips. Each roundtrip adds an order of scattering by updating the scattering wavefields $\delta\vec{S}$, according to equation 2.2.21. Hence, for the first roundtrip only primaries without transmission effects are modeled. However, for the second roundtrip primaries and first-order multiples are modeled and so on for subsequent roundtrips. With more roundtrips the transmission effects become more accurate. The recursive modeling method is akin to the Bremmer series [Bremmer, 1951; de Hoop et al., 2000], where each iteration adds a new order of scattering. Note that in this description we do not take into account diving waves nor do we consider surface waves such as direct wave and ground rolls. The recorded data is assumed to consist of upgoing wavefields only, hence, deghosting must me done prior to inversion.

2.3 Forward Modeling Examples

In this section the anisotropic modeling method is demonstrated on a 2D synthetic model and is compared to its isotropic counterpart. Figure 2.6 shows the reflectivity, vertical velocity, δ, and ϵ models used for modeling. Equations 2.2.25 and 2.2.26 are used to generate reflection data using a split spread geometry. The source is a Ricker wavelet with a dominate frequency of $10Hz$ located at lateral location $2000m$. No free surface multiples were modeled, however, internal multiples were taken into account. Figure 2.7a shows the primaries and figure 2.7b shows the primaries and first-order multiples, while figure 2.7c shows the difference between a and b, i.e. the 1st order multiples only. Similarly, figure 2.7d shows the primaries and first-order multiples (i.e. same as figure 2.7b), while figure 2.7e shows the primaries, first-order multiples, and second-order multiples. Finally, figure 2.7f shows the difference between d and e, i.e. the second-order multiples. Note that the multiples exponentially increase the amount of events in the data with each successive roundtrip, however, their amplitudes decrease dramatically. Also note that the sources and receivers are in an anisotropic layer, which could cause the pseudo S-wave to be recorded. However, they do not exist in the recorded data due to the flexibility of the modeling method in eliminating them.

In order to compare the effects of anisotropy on the multiples, we update the

model (in figure 2.6) to be isotropic (i.e $\delta = \epsilon = 0$). Figure 2.8 shows the isotropic counterpart to figure 2.7. It is possible to analyze the anisotropic effects by comparing both data sets. The isotropic shot gather is shown in red while and the anisotropic shot gather is shown in black in figure 2.9. FWMod allows us to separate the primaries from the multiples, therefore, we can analyze the isotropic (red) and anisotropic (black) primaries (Figure 2.10). Note that the first reflection shows the maximum difference, this is because the anisotropy is largest for the first layer and the first reflection has a broader range of angles compared to the deeper reflectors (due to its position and the acquisition geometry). Figure 2.11 shows a comparison between the isotropic (red) and the anisotropic (black) first-order internal multiples. Note that as in the previous case (Figure 1.9b) the deviation is happening away from the apex.

Also note that the difference in primaries is much greater than in the first-order multiples when looking at the same offset. This is because the first-order multiples are associated with smaller angles compared to primaries and in this anisotropic model, the greater the angle the larger the effect of anisotropy. However, note that the number of events that are deviating from their isotropic counterparts has increased drastically. Thus, the residual has more data in it. However, one should note that the multiples generally have a lower amplitude than the primaries. Hence, in practice the added value of using multiples for anisotropic analysis will be dependent on their relative strength compared to the primaries. In Chapter 3 and 4 we study the effect of multiples on the residual more meticulously, and try to understand whether they add extra information or not in inversion.

a)

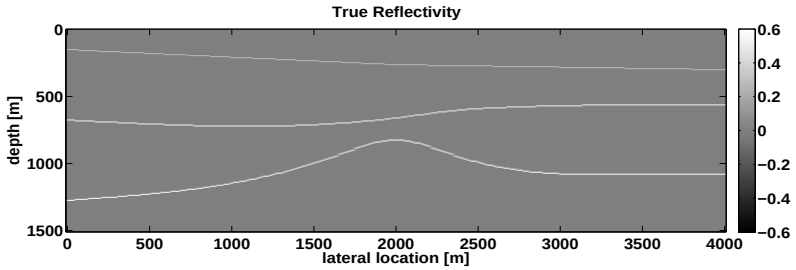

b)

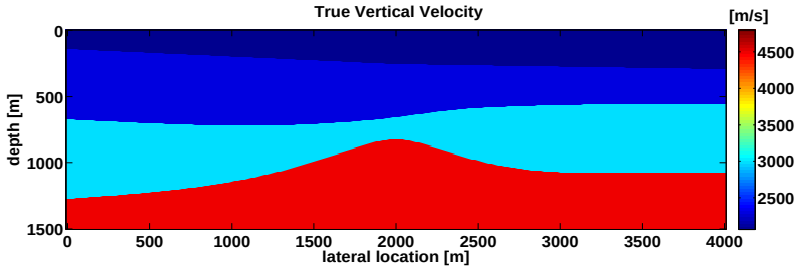

c)

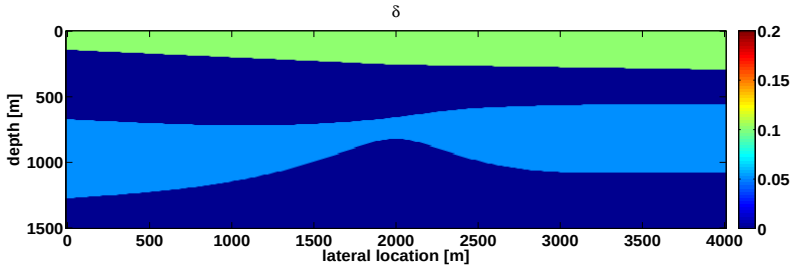

d)

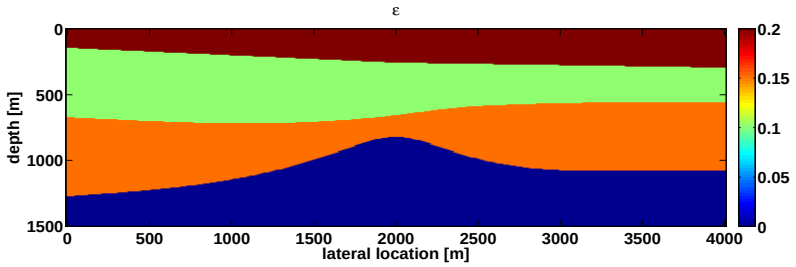

Figure 2.6: *The values for a) the reflectivity, b) the vertical velocity V_v [m/s], c) the δ model, and d) the ϵ model.*

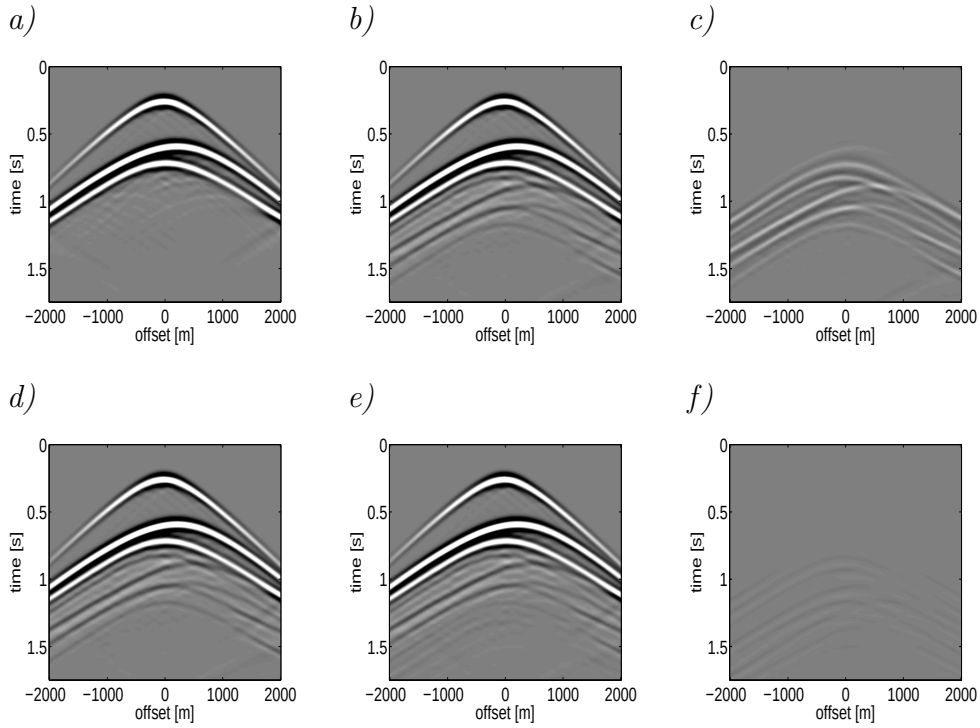

Figure 2.7: *Modeled data via anisotropic FWMod. a) The primary reflections. b) The primary reflections and first-order multiples. c) The first-order multiples obtained via the difference between a) and b). d) The primary reflections and first-order multiples. e) The primary reflections, first-order multiples, and second-order multiples. f) The second-order multiples obtained via the difference between d) and e).*

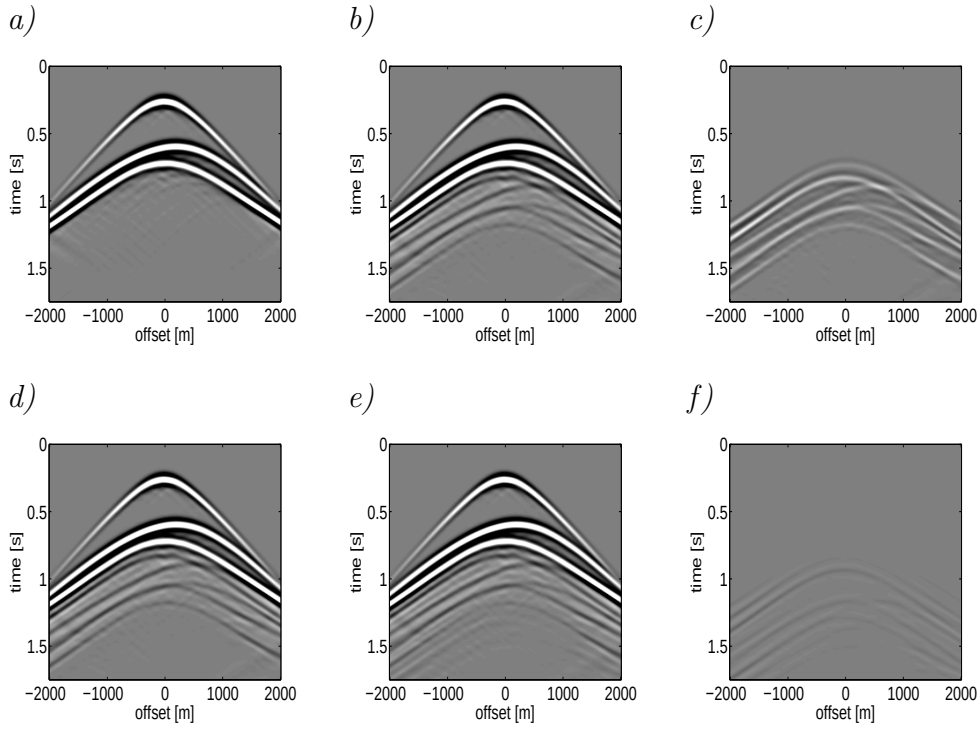

Figure 2.8: *Modeled data via isotropic FWMod. a) The primary reflections. b) The primary reflections and first-order multiples. c) The first-order multiples obtained via the difference between a) and b). d) The primary reflections and first-order multiples. e) The primary reflections, first-order multiples, and second-order multiples. f) The second-order multiples obtained via the difference between d) and e).*

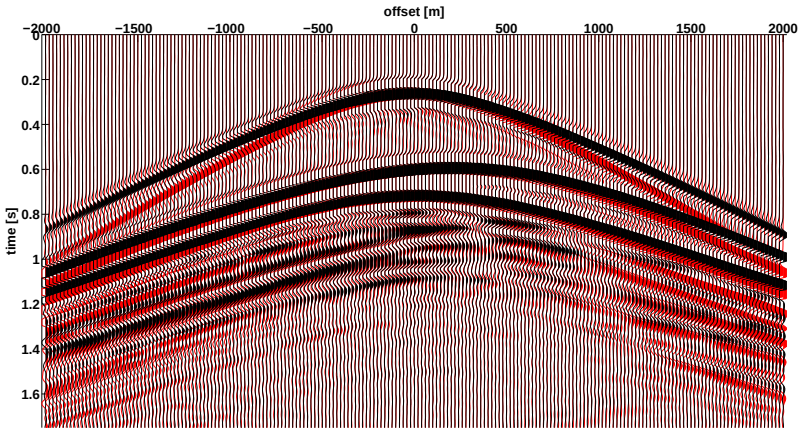

Figure 2.9: *The anisotropic (black) and isotropic (red) shot gathers related to figure 2.7e and 2.8e.*

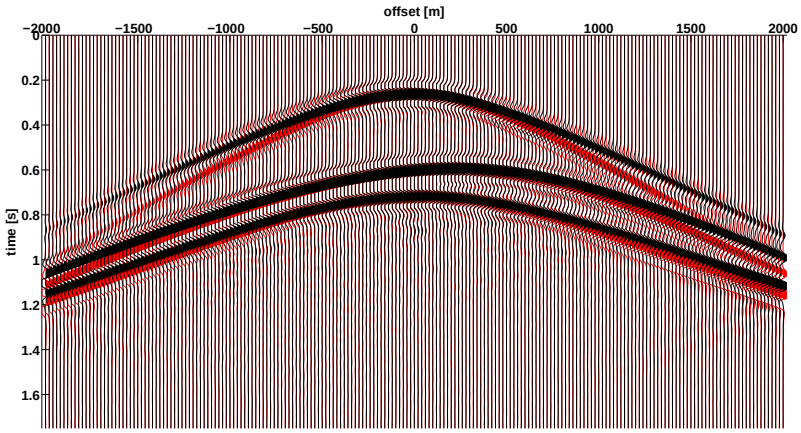

Figure 2.10: *The anisotropic (black) and isotropic (red) primaries related to figure 2.7a and 2.8a.*

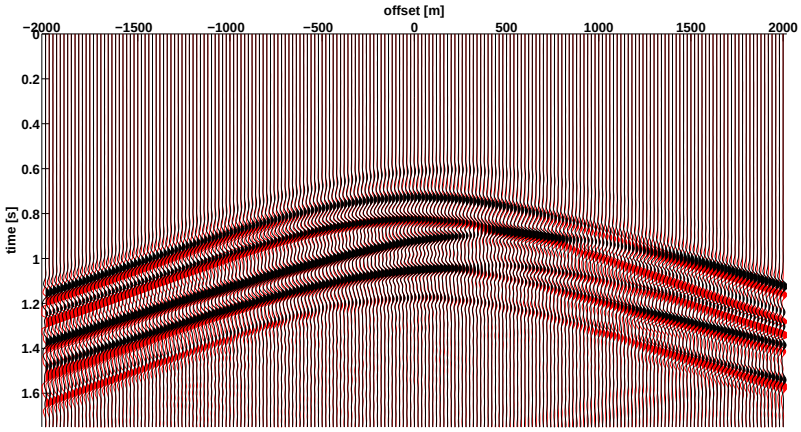

Figure 2.11: *The anisotropic (black) and isotropic (red) first-order multiples, related to figure 2.7c and 2.8c.*

3

Theory of JMI in VTI media

Unlike modeling, the choice of parametrization in inversion is of utmost importance in multi-parameter inversion problems. Joint Migration Inversion is unique in its chosen parametrization, as it ideally provides a solution for the reflectivity operator $\mathbf{R}$ and the propagation operator $\mathbf{W}$. It is unique in that other methods (e.g. FWI) do not make this distinct separation between scattering and propagation. In its current implementation $\mathbf{W}$ is isotropic, with $\mathbf{W}$ being further parameterized in terms of the velocity [Staal, 2015]. Extending the method to handle anisotropic kinematics one needs to re-parametrize the propagation operator $\mathbf{W}$. One must also take into account the sensitivity and trade-off of the different parameters in order to stabilize the inversion. In this chapter we review a number of different parameterizations proposed for inversion. We then evaluate the associated cost function for our chosen parameterization. The cost function gives insights on how the chosen parametrization behaves in inversion. It also allows us to analyze the sensitivity of the method to multiples. With the parameterization in hand we then derive the anisotropic gradients and refine the JMI algorithm to handle VTI kinematics.

3.1 Parametrization

With the abundance of different parameterizations available for VTI inversion, one needs to analyze the sensitivity and trade-off between the different parameters on the data. The resolution possibilities and limitations associated must be investigated before inversion. Many authors analyze different parameterizations for anisotropic FWI applications and we rely on their work to understand the advantages and disadvantages of the different parameterizations.

Plessix and Cao [2010] studied the VTI parametrization of acoustic FWI and analyzed which parameters can be retrieved. They did this by applying eigenvalue decomposition analysis on the Hessian. The parametrization they analyzed was V_{nmo}, δ, η and V_{nmo}, δ, V_h. They concluded that δ can not be retrieved due to the intrinsic ambiguity between this parameter and depth. However, the other parameters can be retrieved with different degrees of accuracy from different parts of the data. For instance the η parameter and V_h are predominately sensitive to the diving wave, while the V_{nmo} is predominantly sensitive to the short offset reflections. Nonetheless, trade-off is still apparent in both parameterizations especially in the middle part of the gathers. Therefore, they suggested using a hierarchical approach where they limit the cable length in subsequent iterations to alleviate some of the trade-off.

Gholami et al. [2013b] also investigated which parametrization is suitable for FWI in VTI media. They analyzed different parameter classes on the modeled data as a function of the scattering angle. Their primary analysis is done via computing the radiation patterns of virtual sources for different parameterizations. The radiation patterns show the sensitivity of each parameter as a function of angle. By analyzing the different radiation patterns for the different sets of parameters they conclude that the choice of parameterization highly depends on the acquisition geometry. For narrow azimuth surveys a V_v, δ, and ϵ parameterization is suitable. However for wide azimuth surveys V_v, δ, and V_h is more suitable, since the velocity parameterization has considerably less trade-off. The wide aperture data updates the large to intermediate wavelengths of the horizontal velocity, whereas the narrow aperture data updates the short to intermediate wavelengths of the vertical velocity. They supported their findings by inverting with a number of different parameterizations and then analyzing their accuracy [Gholami et al.,

2013a].

Alkhalifah [2014] investigates many aspects of anisotropic FWI, he devotes a whole chapter towards choosing an optimal parametrization for VTI media. He arrives at two notable sets of parameterizations, the first consists of V_{nmo}, δ, and η. It facilitates inverting for reflections and diving waves. The second consists of V_h, η, and ϵ. It accommodates the need for FWI to start with diving waves. Alkhalifah and Plessix [2014] evaluate the sensitivity kernels (the response of the model space to perturbations in the data) to study the angular dependency of these two parameterizations. By evaluating the associated radiation pattern for each parametrization set they are able to understand which parts of the wavefield will update which parameters. For the V_{nmo}, δ, η parameterization, the NMO velocity has an angle-invariant radiation pattern while η is mostly associated with the horizontal component. The angle-invariant radiation pattern associated with V_{nmo} is attractive since it facilitates a hierarchal approach where one inverts for the isotropic case before moving towards a VTI case. It also enables all parts of the wavefields short and long offsets to update the NMO velocity. However, significant trade-off exists between V_{nmo} and η, for which they suggest obtaining V_{nmo} from reflection velocity analysis then updating it with FWI. Since δ is weakly resolvable from the geometrical aspects of the wavefield they categorize it as a secondary parameter that is used to compensate for the deficiency of the acoustic assumption. The second parameterization set of V_h, η, and ϵ is of little interest to us since in our current implementation we will not use the diving waves to update the model parameters.

Other anisotropy parameterizations are provided by Kamath and Tsvankin [2016], where they investigate a velocity parameterization (V_v,V_{nmo},V_h, and the shear velocity) for the elastic VTI case, while Lee et al. [2010] update the elastic coefficient in the elasticity matrix for inversion for the elastic VTI case. There is no general consensus on which parametrization is ideal for acoustic VTI inversion. However, we can conclude that the parametrization chosen highly depends on the inversion method, acquisition geometry, accuracy of the starting model as well as any priori information that can be used for inversion.

For our setup we assume that we have wide aperture surface seismic data, we will also mainly rely on reflections to update our model. We also want to minimize the trade-off effects. Hence, we chose to use the V_v, δ, and V_h parameterization for anisotropic JMI. It facilitates reflection type events and

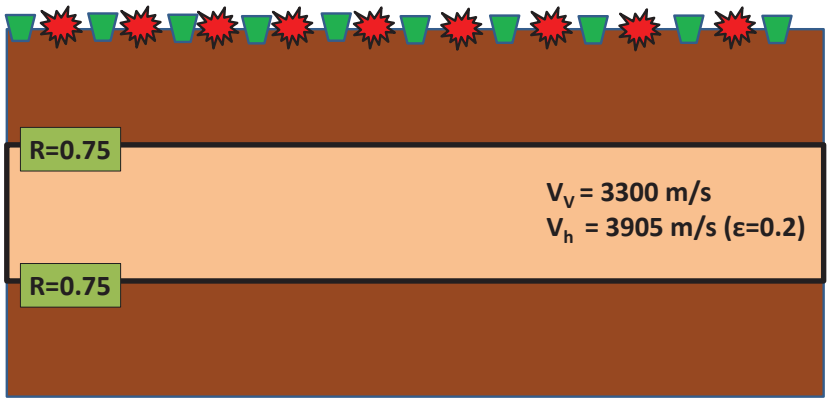

Figure 3.1: *The model used to evaluate the cost function.*

it minimizes the trade-off between the parameters. It also avoids scaling issues, since the inverted parameters are of the same scale. Note that δ is often called the depthing parameter, because it ties V_v with V_{nmo} (equation 2.1.11). δ suffers from intrinsic ambiguity between it and depth, as shown in Alkhalifah and Tsvankin [1995] and later in Plessix and Cao [2010]. Due to the intrinsic ambiguity we will not estimate δ from surface seismic data; its estimates will be reserved for other sources of information, such as well-logs.

3.2 Misfit Function Analysis

The cost function is analyzed in order to understand the nonlinearity associated with the chosen parametrization (V_v, V_h, and δ). We consider a simple $2000m$ wide by $650m$ deep model with an anomaly in the middle (figure 3.1). The anomaly has a vertical velocity of $V_v = 3300m/s$ and a horizontal velocity of $V_h = 3905m/s$, which corresponds to an ϵ of 0.2. There are two prominent reflectors at the top and bottom of the anomaly. There are 41 sources located at equal intervals at the surface. Receivers are also located at the surface at $20m$ intervals. A dense source and receiver acquisition geometry is used in order to reduce the effect of extending the illumination caused by the multiples. The misfit function is evaluated over different values of V_v

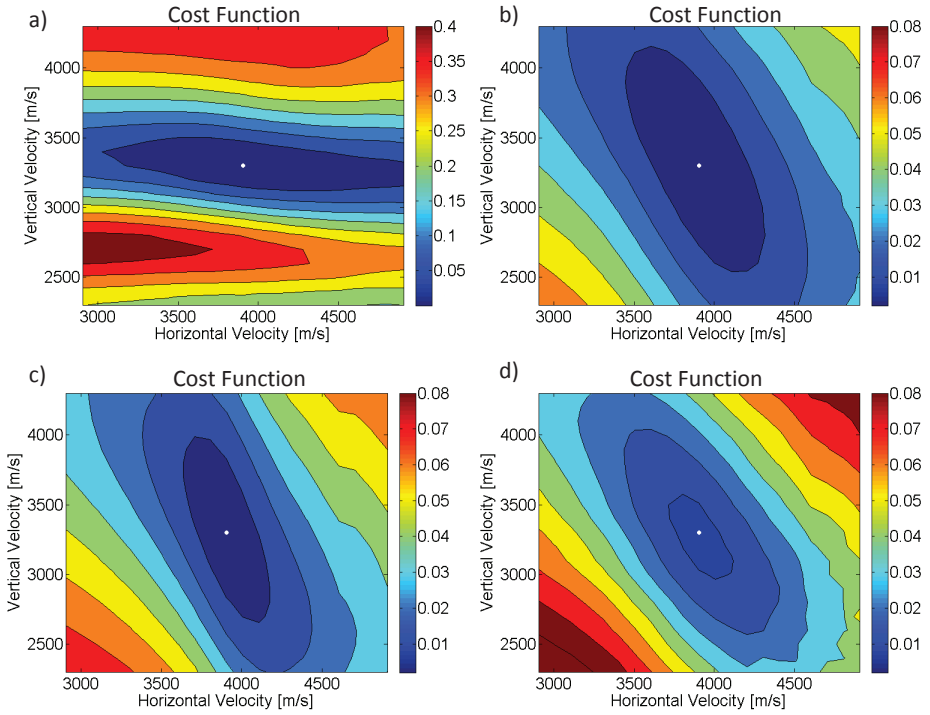

Figure 3.2: *a) The cost function when the reflectivity is fixed. b) The cost function when the reflectivity is estimated. c) The cost function when the offset is doubled. d) The cost function when primaries and multiples are included, the offset is restored to it's original value as in figure 3.2b.*

and V_h. The misfit function is given as:

$$J = \sum_{shots} \sum_{\omega} \left\| \vec{P}^{-}_{obs}(z_0) - \vec{P}^{-}_{mod}(z_0) \right\|^2 = \sum_{shots} \sum_{\omega} \left\| \vec{E}^{-}(z_0) \right\|^2 , \qquad (3.2.1)$$

where $\vec{P}^{-}_{obs}(z_0)$ represents the monochromatic component of the observed or measured wavefield at the surface and $\vec{P}^{-}_{mod}(z_0)$ is the monochromatic component of the modeled or calculated wavefield at the surface z_0. Note that in this example no direct waves were considered only upgoing reflections were recorded (i.e. deghosted data). The misfit function is analyzed by evaluat-

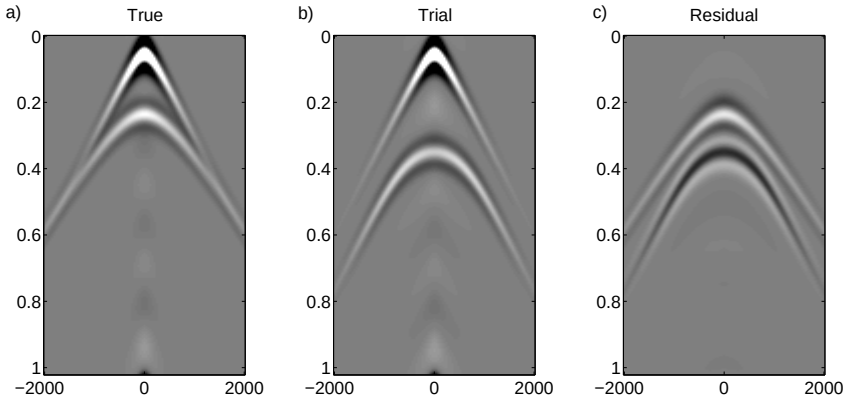

Figure 3.3: *Shot gathers involved in evaluating the cost function for a fixed reflectivity (see Figure 3.2a). a) The observed or true shot gather. b) The modeled or trial shot gather pertaining to trial velocities of* $V_v = 2300m/s$ *and* $V_h = 2905m/s$*. c) The residual between the two. Note that the residual shows that the events are more than half a cycle away, hence cycle-skipping occurs (figure 3.2a).*

ing different sets of vertical and horizontal velocities. Note that we do not estimate the reflectivity but rather fix it to the correct value and position. Furthermore, in this example only the primaries are modeled. Figure 3.2a shows the associated misfit function. The V_v parameter is very well defined compared to V_h, as there is no vertical valley. On the other hand there is a large horizontal valley along the V_h parameter. Perhaps the most prominent issue that is apparent are local minima that are caused by cycle-skipping. When the reflectivity is fixed and not updated, the reflected events in the data might appear more than half a cycle away from each other (depending on the trial velocities), and therefore a meaningful update is not obtained. Figure 3.3 exemplifies this case in the shot gather domain. Note that the second event in the trial gather arrives very late compared to the true one. The trial velocities, corresponding to $V_v = 2300$ and $V_h = 2905$, cause the second reflection to be more than half a cycle away from the true one. If one were to use gradient decent methods it would be very difficult to converge to the global solution from a highly erroneous starting model without modifying the inversion technique.

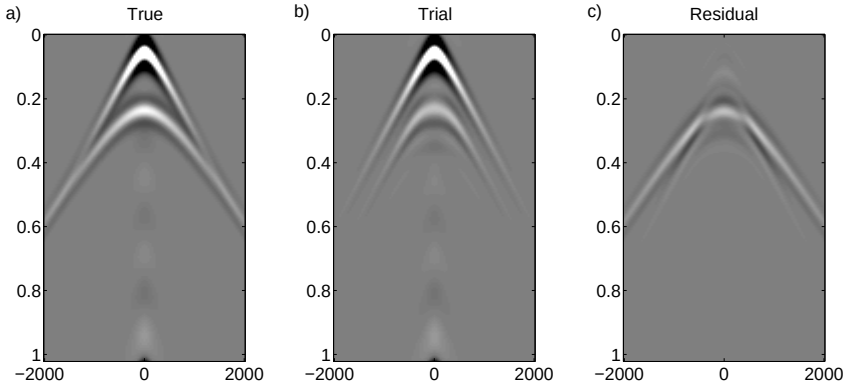

Figure 3.4: *Shot gathers involved in evaluating the cost function when the reflectivity is estimated (see Figure 3.2b). a) The observed or true shot gather. b) The modeled or trial shot gather pertaining to trial velocities of* $V_v = 2300m/s$ *and* $V_h = 2905m/s$*. c) The residual between the two. Note that the residual shows that the events are now interacting due to estimating the reflectivity (figure 3.2b).*

We re-evaluate the misfit function, we use the same model and the same geometry as in the previous experiment. However, for each trial point (V_v and V_h pair) the best fit reflectivity is evaluated as well via Full Wavefield Migration (see section 3.3.1 for more information over FWM). Hence, we do not assume a fixed reflectivity. The reflectivity moves the reflected event to the location that produces the least error between the observed and calculated data. Figure 3.2b shows the associated misfit function for the second experiment. What is noteworthy is that the local minima are no longer there. By allowing the reflectivity to move, it is possible to drastically reshape the misfit function and enable it to be more suitable for gradient descent methods. This is corroborated by the findings of Alkhalifah [2016b], where he analyzes the role of a non-fixed reflector on the radiation parameters. Figure 3.4 shows a shot gather that corresponds to the same trial velocities (V_v and V_h) as in figure 3.3, however, the best fit reflectivity is estimated. Note that the second reflection in the trial gather falls on top of the second reflection in the observed gather (around the apex). Hence, updating the reflector is more manageable than in the previous case. Despite the absence of local min-

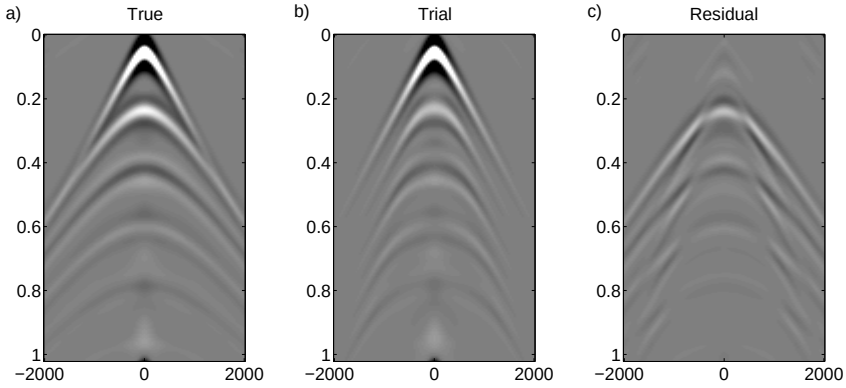

Figure 3.5: *Shot gathers involved in evaluating the cost function when internal multiples are included (see Figure 3.2d. a) The observed or true shot gather. b) The modeled or trial shot gather pertaining to trial velocities ($V_v = 2300m/s$ and $V_h = 2905m/s$). c) The residual between the two. The multiple events add the extra sensitivity in the cost function (figure 3.2d).*

ima, there is a degree of trade-off happening between V_v and V_h (the slanted valley). This trade-off would cause issues in arriving at a unique solution, because many solutions fulfill the misfit function fairly well. Without a priori information it is difficult to arrive at a unique solution, especially when there is noise in the data.

One would like to reduce the trade-off as much as possible. Therefore, one obvious attempt to reduce it is by redesigning the acquisition survey such that more horizontally traveling waves are acquired. The same experiment is repeated, however, the maximum offset is extended to double its initial value. The receivers span $4000m$ with the same sources as in the previous experiment. Figure 3.2c shows the new misfit function, where we can note that the valley is much narrower in the V_h parameter than in figure 3.2b. The reason is because there are more horizontally traveling waves acquired in the data, which help in better defining the horizontal velocities. However, the accuracy of the vertical velocity does not improve much.

Another attempt to reduce the trade-off is to include internal multiples. The acquisition is restored back to the original case of receivers only spanning $2000m$ (the same geometry as in the first and second experiments). However,

internal multiples are introduced in modeling. In the previous experiments only primaries are considered in both the observed and modeled data. In this particular experiment the observed and modeled data include internal multiples, in order to understand their effects on the cost function. The setup is the same as in the second experiment, with figure 3.2d being the new result. Both the vertical velocity and horizontal velocity are more uniquely defined, compared to the primaries-only case (figure 3.2b versus figure 3.2d). Surprisingly, they are also more uniquely defined compared to the third experiment where the offset was doubled (figure 3.2c versus figure 3.2d). Figure 3.5 shows a shot gather that corresponds to the same V_v and V_h as in figure 3.3, however, the internal multiples are included and the best fit reflectivity is estimated. In this experiment, the multiples are mostly associated with vertical events. This is because multiples usually have a smaller propagation angle compared to primaries at the same offset. Hence, they bring in the extra sensitivity to the V_v parameter. However, in order to obtain accurate V_h estimates one must have accurate V_v estimates for surface seismic geometries. Therefore, although the internal multiples are mostly associated with smaller angles than primaries, their influence leaks onto the V_h parameter in an indirect way. The more accurate the V_v estimate, the more accurate the V_h parameter is in turn.

Finally, for the sake of completion we evaluate the cost function associated with a different parametrization, namely V_{nmo}, δ, and η. As in the previous parameterization δ will not be estimated but rather it will be obtained from other sources of information. We translate both ranges of V_v and V_h into their corresponding V_{nmo} and η ranges. Figure 3.6a shows the cost function associated with V_{nmo} and η while figure 3.6b shows the cost function associated with V_v and V_h. Note that only primaries were considered in evaluating both cost functions. Analyzing them shows that the low error range (the blue colored valley in figure 3.6) of V_v and V_{nmo} is similar. However, the low error range (blue colored valley in figure 3.6) of V_h and η are drastically different. Although both misfit functions have a degree of trade-off we can see that for the V_v and V_h parameterization the trade-off is localized around the true solution compared to the V_{nmo} and η parameterization, where the trade-off is smeared over a larger range. By employing all the strategies exemplified, one may reduce the nonlinearity and the trade-off, via estimating the reflectivity separately, choosing a suitable parametrization, opting for a wider acquisition geometry, and taking internal multiples into account.

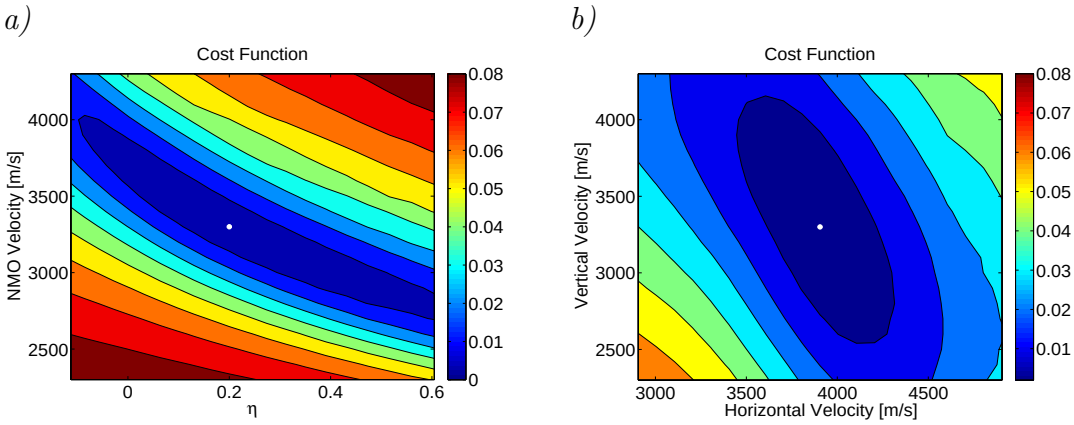

Figure 3.6: *Cost function associated with a (a) V_{nmo} and η parameterization and a (b) V_v and V_h parameterization.*

3.3 Theory of Joint Migration Inversion in VTI media

Anisotropic JMI simultaneously inverts for scattering and propagation operators, which can be directly parametrized in terms of reflectivity and anisotropic velocities. This is done by minimizing the error between the observed and calculated data and linearly updating the parameters via a gradient descent method as done in Berkhout [2012, 2014c] and Staal and Verschuur [2012] for the isotropic case. Note that the scattering and propagation operators are treated as separate entities in JMI. Therefore, the dynamics will be attributed towards the reflectivity, while the kinematics will be attributed towards the anisotropic velocities. We expect the estimated anisotropic velocities will be smoothed versions of their true counterparts since the kinematics will be used to update them. On the other hand, the reflectivities will be of high resolution because the dynamics are used to update them.

We follow an iterative gradient descent method in arriving at a solution, where the calculated measurements are compared to the observed measurements in a least-squares sense. For each iteration we compute the misfit

function and its gradient, then we update the reflectivity, vertical velocity, and horizontal velocity. As in FWMod, each iteration or roundtrip adds an order of scattering. In the first iteration only the primaries are addressed. However, for subsequent iterations multiples will be modeled and compared to the observed data's multiples. Hence, they will contribute towards an update for the reflectivity, the vertical velocity, and the horizontal velocity. As indicated in the previous section, multiples can potentially add extra sensitivity in estimating the subsurface parameters. In the following sections we will derive the anisotropic JMI gradients and modify the inversion strategy in order to incorporate VTI kinematics.

3.3.1 Reflectivity

The reflectivity is updated in each iteration via Full Wavefield Migration [Berkhout, 2014b; Davydenko and Verschuur, 2017]. FWM is based on minimizing the error between the observed and calculated reflections at the surface (equation 3.2.1), assuming that the migration velocity is correct. In our implementation each point in the subsurface will be characterized as a scalar reflector. Therefore, the reflectivity matrix $\mathbf{R}$ is a diagonal matrix with the scalar reflectivity $\Delta\vec{r}$ values along its diagonal. We can write the reflectivity as:

$$\mathbf{R}^{\cup}(z_m) = \mathbf{R}_0^{\cup}(z_m) + \Delta\mathbf{R}^{\cup}(z_m), \tag{3.3.2}$$

where $\mathbf{R}^{\cup}$ is the true reflectivity, $\mathbf{R}_0^{\cup}$ is background reflectivity which is the current estimate of the reflectivity, and $\Delta\mathbf{R}^{\cup}$ is the update that tries to make the background reflectivity equal to the true reflectivity. The gradient of reflectivity is given as:

$$\Delta\mathbf{R}^{\cup}(z_m) = \sum_{shots}\sum_{\omega}\left[\mathbf{W}^{-}(z_0, z_m)\right]^H \vec{E}^{-}(z_0)\left[\vec{P}^{+}(z_m)\right]^H, \tag{3.3.3}$$

where $\mathbf{W}$ is the VTI propagation operator that is based on equation 2.1.15. $\Delta\mathbf{R}^{\cup}$ is a square matrix that has the gradient values of the reflectivity $\Delta\vec{r}$ along its diagonal. The superscript H represents the Hermitian, note however that in practice we approximate it by the transpose. Only scalar reflectivity is considered, therefore, all off-diagonal elements of $\Delta\mathbf{R}^{\cup}$ are discarded in

the following steps, yielding a diagonal matrix for $\Delta\mathbf{R}^{\cup}$. The gradient is computed by cross-correlating the back-propagated residual and the forward propagated source field and then summing over frequency at each depth level. With more iterations we include more roundtrips, hence, internal multiples are included in our forward modeled data and can be matched with observed internal multiples in the back-propagated residual when we apply our imaging condition. Hence, the multiples will contribute towards imaging a point in the subsurface. A prominent issue in imaging with multiples is the cross-talk between primaries and higher-order multiples (cross-correlating a primary event with a second-order multiples, for example). The cross-talk would cause noise for the initial iterations, however, with more iterations the multiples are naturally explained via the modeling engine. Therefore, the cross-talk (residual of the multiples) naturally decays in the closed-loop approach. With the reflectivity gradient computed for each depth level z_m, we can define the wavefield perturbation associated with the update in $\mathbf{R}$ at each level by:

$$\Delta\vec{P}^{-}_{\Delta r}(z_0) = \sum_{m=1}^{M} \mathbf{W}^{-}(z_0, z_m)\, \Delta\mathbf{R}^{\cup}(z_m)\, \vec{P}^{+}(z_m; z_0)\,. \tag{3.3.4}$$

The step length or the scaling parameter α_r is given by:

$$\alpha_r = argmin_{\alpha_r} \left(\sum_{shots} \sum_{\omega} \left\| \vec{E}^{-}(z_0) - \alpha_r \Delta\vec{P}^{-}_{\Delta r}(z_0) \right\|^2 \right). \tag{3.3.5}$$

Taking the derivative with respect to α_r and equating the expression to zero, we arrive at:

$$\alpha_r = \frac{\sum_{shots}\sum_{\omega} \left(\left[\Delta\vec{P}^{-}_{\Delta r}\right]^H \vec{E}(z_0) + \left[\vec{E}(z_0)\right]^H \Delta\vec{P}^{-}_{\Delta r} \right)}{\sum_{shots}\sum_{\omega} 2 \left[\Delta\vec{P}^{-}_{\Delta r}\right]^H \Delta\vec{P}^{-}_{\Delta r}}. \tag{3.3.6}$$

Note that a true line search is required in order to obtain accurate values of α_r, however, we assume that the linearization error is low in order to reduce the computational cost for each iteration. However, taking this simplified approach to calculating α_r does not guarantee that the objective function will be lowered at each iteration. The reflectivity is updated for each iteration (i) as:

$$\mathbf{R}^{\cup}_{(i)} = \mathbf{R}^{\cup}_{(i-1)} + \alpha_r \Delta \mathbf{R}^{\cup}_{(i)}, \tag{3.3.7}$$

where we usually start the process by setting $\mathbf{R}^{\cup}_{(0)} = 0$. In our derivation we assume that $\mathbf{R}^{\cup} = -\mathbf{R}^{\cap}$ in order to reduce the number of parameters estimated for each depth level. However, one can derive a separate gradient for $\mathbf{R}^{\cap}$ in order to incorporate imaging from below, as was done in Davydenko and Verschuur [2013, 2017].

3.3.2 Vertical Velocity

In section 3.1 we have chosen to parametrize the $\mathbf{W}$ operator in terms of a vertical velocity (V_v), a horizontal velocity (V_h), and δ. In this section we formulate the theory for estimating the V_v parameter. The process is fairly similar to the reflectivity, where we compute a gradient and a step length and then update the parameter. We start by defining a vertical velocity contrast parameter β_v as:

$$\beta_v(x,z) = 1 - \frac{V0_v(x,z)^2}{V_v(x,z)^2}, \tag{3.3.8}$$

where $V0_v$ is the background vertical velocity, while V_v is the true vertical velocity. The extrapolation operators in the true medium for the upgoing and downgoing wavefields are then defined as:

$$\mathbf{W}^{-}(z_m, z_{m+1}) = \mathbf{W}_0^{-}(z_m, z_{m+1}) + \Delta\mathbf{W}^{-}(z_m, z_{m+1}), \tag{3.3.9}$$

and

$$\mathbf{W}^{+}(z_{m+1}, z_m) = \mathbf{W}_0^{+}(z_{m+1}, z_m) + \Delta\mathbf{W}^{+}(z_{m+1}, z_m), \tag{3.3.10}$$

where $\mathbf{W}_0^{\mp}$ are the extrapolation operators defined in the background medium and $\Delta\mathbf{W}^{\mp}$ are the differences between the true and background operators. The linearization of a single column of $\Delta\mathbf{W}^{\mp}$ with respect to β_v is given as:

$$\Delta\vec{W}^{-}(z_m, z_{m+1}) \approx \left[\frac{\partial\vec{W}^{-}}{\partial\beta_v}\right]_{\beta_v=0} \beta_v(x, z_m) = \vec{G}_v^{-}(z_m, z_{m+1})\beta_v(x, z_m), \tag{3.3.11}$$

and

$$\Delta\vec{W}^{+}\left(z_{m+1},z_{m}\right)\approx\left[\frac{\partial\vec{W}^{+}}{\partial\beta_{v}}\right]_{\beta_{v}=0}\beta_{v}(x,z_{m})=\vec{G}_{v}^{+}(z_{m+1},z_{m})\beta_{v}(x,z_{m}), \tag{3.3.12}$$

where the anisotropic-medium $\vec{G}_v$ is given as:

$$\vec{G}_{v}\left(z_{m},z_{n}\right)\approx\mathcal{F}_{x}^{-1}\left[\frac{j\Delta z}{2k_{z}+\sigma}(D_{v})e^{-jk_{z}\Delta z}e^{-jk_{x}x_{i}}\right], \tag{3.3.13}$$

where $\mathcal{F}_x^{-1}$ indicates taking the inverse spatial Fourier transform and organizes the result in a vector. σ is a stabilization term to avoid dividing by zero. D_v is given by:

$$D_{v}=\left(\frac{\omega}{V0_{v}}\right)^{2}-\frac{\omega^{2}V0_{v}^{2}(1+2\delta)^{2}k_{x}^{4}}{\left(\omega^{2}-(V_{h}^{2}-V0_{v}^{2}(1+2\delta))k_{x}^{2}\right)^{2}}. \tag{3.3.14}$$

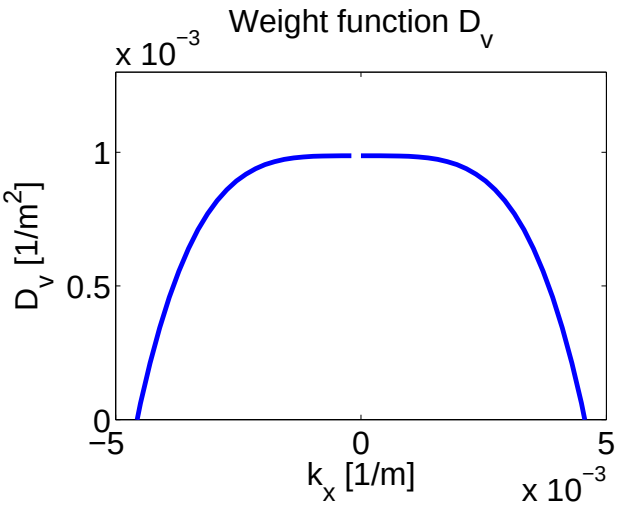

Figure 3.7: *The scaling parameter D_v. Note that it decays for larger values of $|k_x|$.*

A detailed derivation of the gradient is provided in appendix A. Upon further investigation we find that D_v is a scaling term that prioritizes the vertically traveling events (events located close to $k_x = 0$) in updating the β_v gradient. Figure 3.7 shows the D_v scaling parameter at $10Hz$ for a VTI medium with $V_v = 2000$, $\epsilon = 0.2$, and $\delta = 0.1$. Note that as $|k_x|$ increases the scaling decreases. Hence, vertically traveling waves have a greater effect in updating the gradient compared to horizontally traveling waves. We limit the scaling effect of D_v to span the domain of the real part of k_z, since we are mostly interested in the propagating waves. With the linearization at hand, we can define the total vertical velocity contrast gradient $\Delta\vec{\beta}_v$ as a summation of:

$$\Delta\vec{\beta}_v(z_m) = \Delta\vec{\beta}_v^{-}(z_m) + \Delta\vec{\beta}_v^{+}(z_m), \tag{3.3.15}$$

where $\Delta\vec{\beta}_v^{-}(z_m)$ is the contrast gradient utilizing upgoing waves and $\Delta\vec{\beta}_v^{+}(z_m)$ is the contrast gradient utilizing downgoing waves. They are given by:

$$\Delta\vec{\beta_v^{-}}(z_m) = diag\left(\sum_{shots}\sum_{\omega}\left[\mathbf{G}_v^{-}(z_m, z_{m+1})\right]^H \vec{E}^{-}(z_m)\left[\vec{Q}^{-}(z_{m+1})\right]^H\right), \tag{3.3.16}$$

and

$$\Delta\vec{\beta_v^{+}}(z_m) = diag\left(\sum_{shots}\sum_{\omega}\left[\mathbf{G}_v^{+}(z_{m+1}, z_m)\right]^H \vec{E}^{+}(z_{m+1})\left[\vec{Q}^{+}(z_m)\right]^H\right), \tag{3.3.17}$$

with $\vec{E}^{-}(z_m)$ being the upgoing back-propagated residual and $\vec{E}^{+}(z_m)$ being the downgoing back-propagated residual obtained via the reflectivity estimate. They are given by:

$$\vec{E}^{-}(z_m) = \left[\mathbf{W}^{-}(z_0, z_m)\right]^H \vec{E}^{-}(z_0), \tag{3.3.18}$$

while

$$\vec{E}^{+}(z_m) = \sum_{n>m}\left[\mathbf{W}^{+}(z_n, z_m)\right]^H \mathbf{R}^{\cup}(z_n)\vec{E}^{-}(z_n). \tag{3.3.19}$$

The velocity gradient is fundamentally different from the reflectivity gradient. The reflectivity gradient is computed by examining wavefields propagating in opposite directions (upgoing and downgoing) at a certain depth level in the subsurface. However, for the the velocity contrast gradient we examine wavefields propagating in the same direction (both upgoing or both downgoing) at a certain depth level in the subsurface. Figures 3.8 and 3.9 show schematically the wavefields used to compute each gradient. The associated perturbation for the vertical velocity contrast can be defined as:

$$\Delta \mathbf{P}^{-}_{\Delta\beta_v}(z_0) = \sum_{m=1}^{M} \mathbf{W}^{-}(z_0, z_m)\, \mathbf{G}^{-}_{v}(z_m, z_{m+1})\, \Delta\boldsymbol{\beta_v}(z_m)\, \vec{Q}^{-}(z_{m+1}) + \sum_{m=1}^{M}\sum_{n>m}^{M} \mathbf{W}^{-}(z_0, z_n)\mathbf{R}^{\cup}(z_n)\mathbf{W}^{+}(z_n, z_{m+1})\mathbf{G}^{+}_{v}(z_{m+1}, z_m)\Delta\boldsymbol{\beta_v}(z_m)\, \vec{Q}^{+}(z_m)\,, \tag{3.3.20}$$

where $\Delta\boldsymbol{\beta}_v$ is a square matrix with gradients $\Delta\vec{\beta}_v(z_m)$ along its diagonal. Finally, the new vertical velocities will be updated as:

$$V_v^{(i)} = \frac{V_v^{(i-1)}}{\sqrt{1-\alpha_v \Delta\beta_v}}, \tag{3.3.21}$$

where i is the iteration number and α_v is the step length.

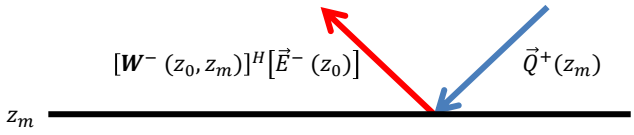

Figure 3.8: *Schematic representation of the downgoing and upgoing wavefields contributing towards a reflectivity update at depth level z_m.*

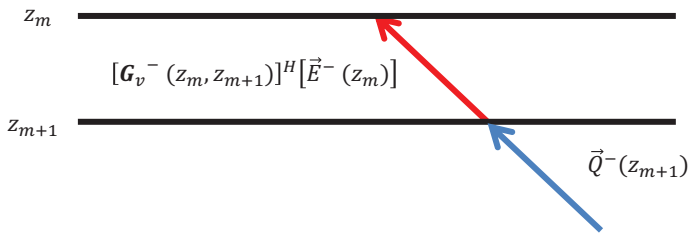

Figure 3.9: *Schematic representation of the two upgoing wavefields contributing towards a velocity update at depth level z_m.*

■ 3.3.3 Horizontal Velocity

As in the vertical velocity case, we define a contrast parameter associated with the horizontal velocity as:

$$\beta_h(x,z) = 1 - \frac{V0_h(x,z)^2}{V_h(x,z)^2}, \tag{3.3.22}$$

where $V0_h$ is the background horizontal velocity, while V_h is the true horizontal velocity. The extrapolation operators can be written as:

$$\mathbf{W}^{-}(z_m, z_{m+1}) = \mathbf{W}_0^{-}(z_m, z_{m+1}) + \Delta\mathbf{W}^{-}(z_m, z_{m+1}), \tag{3.3.23}$$

and

$$\mathbf{W}^{+}(z_{m+1}, z_m) = \mathbf{W}_0^{+}(z_{m+1}, z_m) + \Delta\mathbf{W}^{+}(z_{m+1}, z_m), \tag{3.3.24}$$

where $\mathbf{W}_0^{\mp}$ is the extrapolation operator defined in the background medium. $\Delta\mathbf{W}^{\mp}$ is the difference between the true and background operators. We linearize $\Delta\mathbf{W}^{\mp}$ with respect to β_h, where each column can be written as:

$$\Delta\vec{W}^{-}(z_m, z_{m+1}) \approx \left[\frac{\partial\vec{W}^{-}}{\partial\beta_h}\right]_{\beta_h=0} \beta_h(x, z_m) = \vec{G}_h^{-}(z_m, z_{m+1})\beta_h(x, z_m), \tag{3.3.25}$$

and

$$\Delta\vec{W}^{+}(z_{m+1}, z_m) \approx \left[\frac{\partial\vec{W}^{+}}{\partial\beta_h}\right]_{\beta_h=0} \beta_h(x, z_m) = \vec{G}_h^{+}(z_{m+1}, z_m)\beta_v(x, z_m). \tag{3.3.26}$$

The anisotropic-medium $\vec{G}_h$ is given as:

$$\vec{G}_h(z_m, z_n) \approx \mathcal{F}_x^{-1}\left[\frac{j\Delta z}{2k_z + \sigma}(D_h)e^{-jk_z\Delta z}e^{-jk_x x_i}\right], \tag{3.3.27}$$

where $\mathcal{F}_x^{-1}$ indicates taking the inverse spatial Fourier transform and σ is a stabilization term to avoid dividing by zero. D_h is given by:

$$D_h = \frac{\omega^2 V0_h^2(1+2\delta)k_x^4}{\left(\omega^2 - (V0_h^2 - V_v^2(1+2\delta))k_x^2\right)^2}. \tag{3.3.28}$$

A detailed derivation of the gradient is provided in the appendix A. Similar to D_v, D_h is a scaling parameter (or more appropriately radiation parameter). However, D_h prioritizes the events traveling horizontally in updating the β_h gradient. Figure 3.10 shows the D_h scaling parameter at $10Hz$ for a VTI medium with $V_v = 2000$, $\epsilon = 0.2$, and $\delta = 0.1$. Compared to D_v in figure 3.7, D_h increases the weight of events traveling with large $|k_x|$. We also limit the scaling effect to be bound by the domain of real k_z values, to avoid boosting the evanescent wave. The horizontal velocity contrast gradient $\Delta\vec{\beta}_h$ is then defined as a summation of:

$$\Delta\vec{\beta}_h(z_m) = \Delta\vec{\beta}_h^{-}(z_m) + \Delta\vec{\beta}_h^{+}(z_m), \tag{3.3.29}$$

with

$$\Delta\vec{\beta_h^{-}}(z_m) = diag\left(\sum_{shots}\sum_{\omega}\left[\mathbf{G}_h^{-}(z_m, z_{m+1})\right]^H \vec{E}^{-}(z_m)\left[\vec{Q}^{-}(z_{m+1})\right]^H\right), \tag{3.3.30}$$

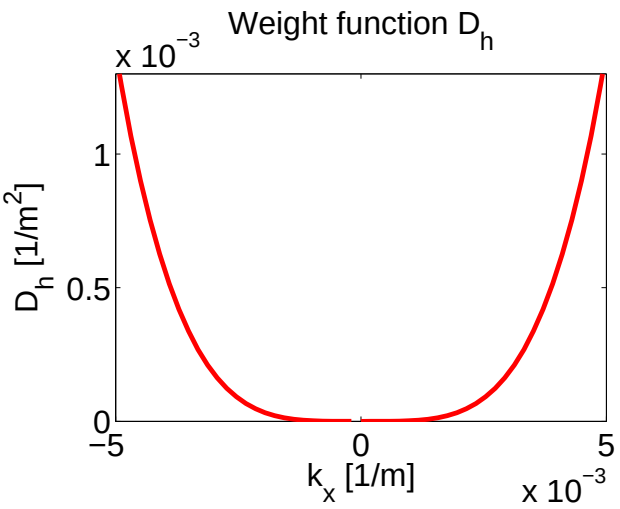

Figure 3.10: *The scaling parameter D_h. Note that it decays for smaller values of $|k_x|$.*

and

$$\Delta\vec{\beta}_h^+(z_m) = diag\left(\sum_{shots}\sum_{\omega}\left[\mathbf{G}_h^+(z_{m+1},z_m)\right]^H\vec{E}^+(z_{m+1})\left[\vec{Q}^+(z_m)\right]^H\right), \tag{3.3.31}$$

where $\vec{E}^-(z_m)$ and $\vec{E}^+(z_m)$ are the upgoing and downgoing extrapolated residual wavefield. They are defined as:

$$\Delta\vec{E}^-(z_m) = \left[\mathbf{W}^-(z_0,z_m)\right]^H\Delta\vec{E}^-(z_0), \tag{3.3.32}$$

and

$$\Delta\vec{E}^+(z_m) = \sum_{n>m}\left[\mathbf{W}^+(z_n,z_m)\right]^H\mathbf{R}^{\cup}(z_n)\Delta\vec{E}^-(z_n). \tag{3.3.33}$$

As in the vertical velocity case we can write the associated perturbation for the horizontal velocity contrast as:

$$\Delta \mathbf{P}^{-}_{\Delta\beta_h}(z_0) = \sum_{m=1}^{M} \mathbf{W}^{-}(z_0, z_m)\, \mathbf{G}^{-}_{h}(z_m, z_{m+1})\, \Delta\boldsymbol{\beta_h}(z_m)\, \vec{Q}^{-}(z_{m+1}) + \sum_{m=1}^{M} \sum_{n>m}^{M} \mathbf{W}^{-}(z_0, z_n)\mathbf{R}^{\cup}(z_n)\mathbf{W}^{+}(z_n, z_{m+1})\mathbf{G}^{+}_{h}(z_{m+1}, z_m)\Delta\boldsymbol{\beta_h}(z_m)\, \vec{Q}^{+}(z_m)\,, \tag{3.3.34}$$

where $\Delta\boldsymbol{\beta}_h$ is a square matrix with gradients $\Delta\vec{\beta}_h(z_m)$ along its diagonal. The update for the horizontal velocities are given as:

$$V_h^{(i)} = \frac{V_h^{(i-1)}}{\sqrt{1 - \alpha_h \Delta\beta_h}}, \tag{3.3.35}$$

where i is the iteration number and α_h is its associated step length.

3.4 Inversion Strategy

Isotropic JMI inverts for the reflectivity and velocity sequentially in the same iteration. With the addition of an extra parameter for the VTI case we need to update the inversion strategy to include the extra parameter. We are interested in reflections that are acquired at the surface. $\mathbf{R}$ and V_v usually have a greater influence on the surface seismic reflections than V_h. Starting with an initial $\mathbf{R}$ and V_v that are far from their true values will cause highly erroneous V_h updates for the initial iterations. However, arriving at a close enough solution for $\mathbf{R}$ and V_v greatly facilitates the convergence of the V_h parameter. Therefore, we prefer to employ a hierarchal approach where we invert for $\mathbf{R}$ and V_v initially and only switch to $\mathbf{R}$, V_v, and V_h inversion when we achieve convergence. Plessix and Cao [2010] and later on Cheng et al. [2014] formulate a similar hierarchal inversion strategy for their chosen parameterizations for FWI applications. The δ parameter will not be estimated in our approach due to the intrinsic ambiguity between it and depth. Therefore, it will be estimated from other sources of information if available.

V_v and V_h are associated with the same operator $\mathbf{W}$ and they have a degree of trade-off happening in between them, as shown in figure 3.2. Finding two different step lengths (α_v and α_h) associated with V_v and V_h respectively in

a flip-flop manner is not ideal since it oscillates the update between the two parameters, for the later iterations. Finding both step lengths and updating the parameters simultaneously helps in alleviating this issue. We solve for α_v and α_h simultaneously by solving the following set of equations:

$$\begin{bmatrix} A & B \\ C & D \end{bmatrix} \begin{bmatrix} \alpha_v \\ \alpha_h \end{bmatrix} = \begin{bmatrix} F \\ G \end{bmatrix}, \tag{3.4.36}$$

where

$$A = \sum_{shots} \sum_{\omega} 2 \left[\Delta \vec{P}_{\Delta\beta_v} \right]^H \Delta \vec{P}_{\Delta\beta_v}, \tag{3.4.37a}$$

$$B = \sum_{shots} \sum_{\omega} \left[\Delta \vec{P}_{\Delta\beta_v} \right]^H \Delta \vec{P}_{\Delta\beta_h}, \tag{3.4.37b}$$

$$C = \sum_{shots} \sum_{\omega} \left[\Delta \vec{P}_{\Delta\beta_h} \right]^H \Delta \vec{P}_{\Delta\beta_v}, \tag{3.4.37c}$$

$$D = \sum_{shots} \sum_{\omega} 2 \left[\Delta \vec{P}_{\Delta\beta_h} \right]^H \Delta \vec{P}_{\Delta\beta_h}, \tag{3.4.37d}$$

$$F = \sum_{shots} \sum_{\omega} \left(\left[\Delta \vec{P}_{\Delta\beta_v} \right]^H \Delta \vec{E}(z_0) + \left[\Delta \vec{E}(z_0) \right]^H \Delta \vec{P}_{\Delta\beta_v} \right), \tag{3.4.37e}$$

$$G = \sum_{shots} \sum_{\omega} \left(\left[\Delta \vec{P}_{\Delta\beta_h} \right]^H \Delta \vec{E}(z_0) + \left[\Delta \vec{E}(z_0) \right]^H \Delta \vec{P}_{\Delta\beta_h} \right). \tag{3.4.37f}$$

With the step lengths at hand we first update the reflectivity $\mathbf{R}$ then we update V_v and V_h simultaneously in each iteration. A single iteration can be summarized as:

[1] Update $\vec{P}^+$ and $\vec{P}^-$ via equations 2.2.25 and 2.2.26.

[2] Calculate the reflectivity gradient $\Delta\mathbf{R}^{\cup}$ via equation 3.3.3.

[3] Calculate the reflectivity perturbation $\Delta \vec{P}^-_{\Delta r}$ via equation 3.3.4.

[4] Calculate the step length α_r associated with the reflectivity gradient via equation 3.3.6.

[5] Update the reflectivity $\mathbf{R}^{\cup}$ via equation 3.3.7.

[6] Update $\vec{P}^{+}$ and $\vec{P}^{-}$ with the new reflectivity $\mathbf{R}^{\cup}$ via equations 2.2.25 and 2.2.26.

[7] Calculate the vertical velocity contrast gradient $\Delta\vec{\beta}_v$ via equation 3.3.15.

[8] Calculated the vertical velocity perturbation $\Delta\mathbf{P}^{-}_{\Delta\beta_v}$ via equation 3.3.20.

[9] Calculate the horizontal velocity contrast gradient $\Delta\vec{\beta}_h$ via equation 3.3.29.

[10] Calculated the horizontal velocity perturbation $\Delta\mathbf{P}^{-}_{\Delta\beta_h}$ via equation 3.3.34.

[11] Calculate the step lengths α_v and α_h associated with the vertical and horizontal velocities respectively via equation 3.4.36.

[12] Update the vertical (V_v) and horizontal (V_h) velocities via equations 3.3.21 and 3.3.35.

Finally, we follow a multi-scale approach where we start with a limited low frequency band then ramp up to wider bands for later iterations. The reason is because the rate of convergence and the stability of the algorithm is better for the low frequency bands than the higher frequency ones. It also reduces the computational cost, arriving at a solution is faster when starting with the lower frequencies (as shown in Staal and Verschuur [2013]).

4

Synthetic Examples

In this chapter, we test the effectiveness of JMI on a number of synthetic VTI models. The first example demonstrates the significance of incorporating anisotropy in inversion. We assume a known anisotropy model and invert for the vertical velocity (V_v) given the anisotropic model. We then invert the same anisotropic data under an isotropic assumption, in order to analyze the effects of anisotropic data on isotropic inversion.

The second example is a step further where we not only invert for the vertical velocity (V_v), but the horizontal velocity (V_h) is updated as well along with the reflectivity. In the third example we show an even more challenging situation where we invert for all three parameters, however, using a different modeling engine to generate the observed data (anisotropic elastic FD modeling), thus avoiding the "inverse crime" situation. We also investigate the convergence of the method. The initial velocities are chosen to have more than $1000m/s$ difference between the initial and the true velocities. In this example we aim to show the flexibility of the method in inverting for a wider range of initial models.

The fourth example tests the effectives of the method to invert for a more complex elastic dataset that was generated using an anisotropic elastic modeling method (FD). Angle-dependent reflectivities and elastic effects such as converted waves are apparent in the data. Therefore, we preprocess the data to attenuate the elastic effects before inversion.

The fifth example analyzes the effects of internal multiples on the inversion. We invert for a model that generates strong internal multiples that reverberate thought the seismic record. We include internal multiples in inversion. Then with the same starting parameters we run the inversion again, however, now we ignore internal multiples in inversion.

For the final example we test the method on the HESS VTI model. The model is a more realistic model that resembles Gulf of Mexico geology. In it we invert for both the vertical and horizontal velocities, along with reflectivity.

4.1 Example 1: Lens-shaped Model

For this example we make use of a modified version of the lens-shaped model presented by Staal [2015] in order to analyze the effects of anisotropy in inversion. We chose this model in particular because it has been studied extensively for isotropic JMI applications. Hence, we can see the effects of anisotropy and compare them with previous JMI results. The model is $2000m$ wide and $620m$ deep and it contains a lens anomaly with flat layers underneath. We add anisotropic coefficients (δ and ϵ) to most of the features in the model. Figure 4.1 shows the reflectivity, vertical velocity, ϵ, and δ distributions. Note that we purposely made the surface anisotropic, meaning that the source and receivers are in an anisotropic region. The pseudo S-wave could manifest itself in the recorded data in some modeling codes. However, here we used phase shift extrapolators in our modeling engine (FWMod), which attenuate the effects of the pseudo S-wave. Also note that the lens anomaly is anisotropic with a negative value of ϵ and $\delta = 0$, resulting in negative values for η, that can cause an exponentially growing solution for some modeling methods. However, due to the flexibility of FWMod and the remedies described in chapter 2 it is possible to remove both limitations.

We generate a Ricker wavelet with a peak frequency of $30Hz$ as the source wavelet. There are 101 equally spaced sources and the receivers span the $2000m$ at $20m$ intervals. The lens anomaly has a high reflectivity compared to the flat target layers underneath, therefore, it will generate strong internal multiples that mask the reflections of the flat layers if not taken into account.

The initial reflectivity is set to zero (figure 4.2a), while the initial vertical velocity model is a linearly increasing model as given in figure 4.2b. In this example a smoothed version of the anisotropic model is assumed to be known

(known δ and ϵ) and the inversion will be focused around estimating the V_v parameter along with $\mathbf{R}$. Figures 4.2c and 4.2d show the resulting image and V_v model after inversion. The velocity model is a smoothed version of the true velocity model due to it relying on the kinematics for inversion. The results also show that the lens and the layers underneath were well recovered in both the reflectivity and the velocity.

In order to illustrate the effect of ignoring anisotropy we invert a second time, however, we assume an isotropic medium. Hence, we assume that $\delta = 0$ and $\epsilon = 0$. We invert for the vertical velocity following the same initial model and the same number of iterations as before. Figures 4.3a and 4.3b show the inverted reflectivity and isotropic velocity. Interestingly, the lens still appears, however, as low velocity anomaly due to the negative value of ϵ. Also note that the region around the lens appears with a higher velocity due to the positive values of δ and ϵ. These anomalies appear because the method is trying to explain the anisotropic effects as isotropic velocity changes. Subsequently, the estimated image suffers due to the erroneous velocity model. This is especially evident from the anticline appearing in the image where the flat layers were supposed to be at $400m$ depth. Surprisingly enough, we do not observe an imprint from the internal multiples. So the wrong model was still accurate enough to explain the internal multiples.

Finally, we invert for $\mathbf{R}$ and V_v assuming a given smooth anisotropic model. However, we account for primaries-only, therefore, internal multiples are considered as noise. For this model the lens causes strong internal multiples that reverberate and mask other weaker events. Figures 4.3c and 4.3d show the inverted reflectivity and vertical velocity. Ignoring the multiples in this case causes severe cross-talk in the image, apparent underneath the lens. The velocity update is also inferior due to the multiples interfering with the layers below. The velocities below the lens appear faster than the true velocities. This is because the internal multiple are associated with the fast velocity in the lens, which leaks into the slower velocity layers underneath the lens.

a)

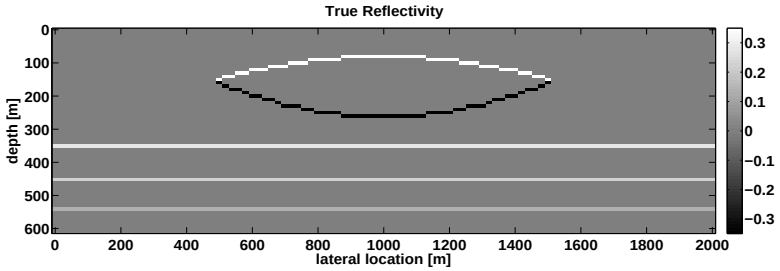

b)

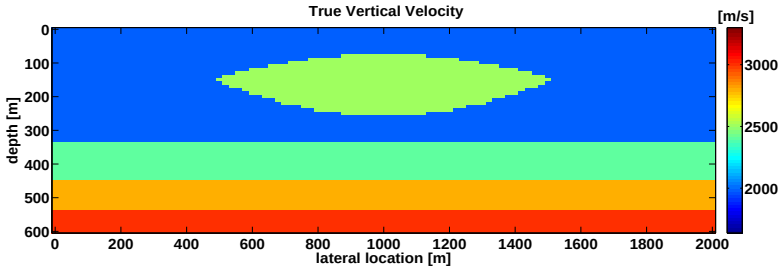

c)

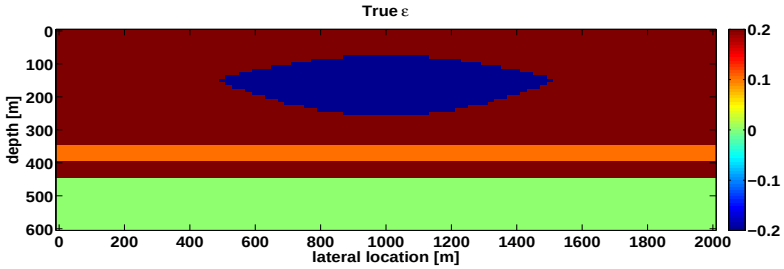

d)

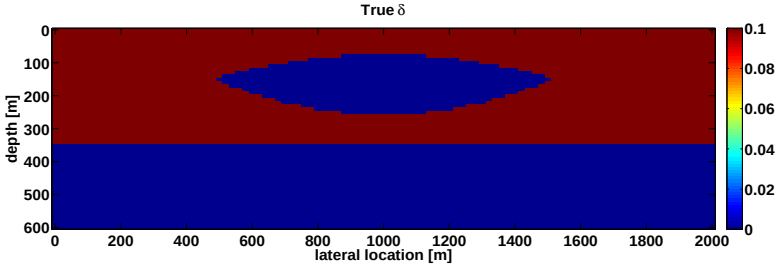

Figure 4.1: *The true values for a) the reflectivity, b) the vertical velocity V_v [m/s], c) the ϵ model, and d) the δ model.*

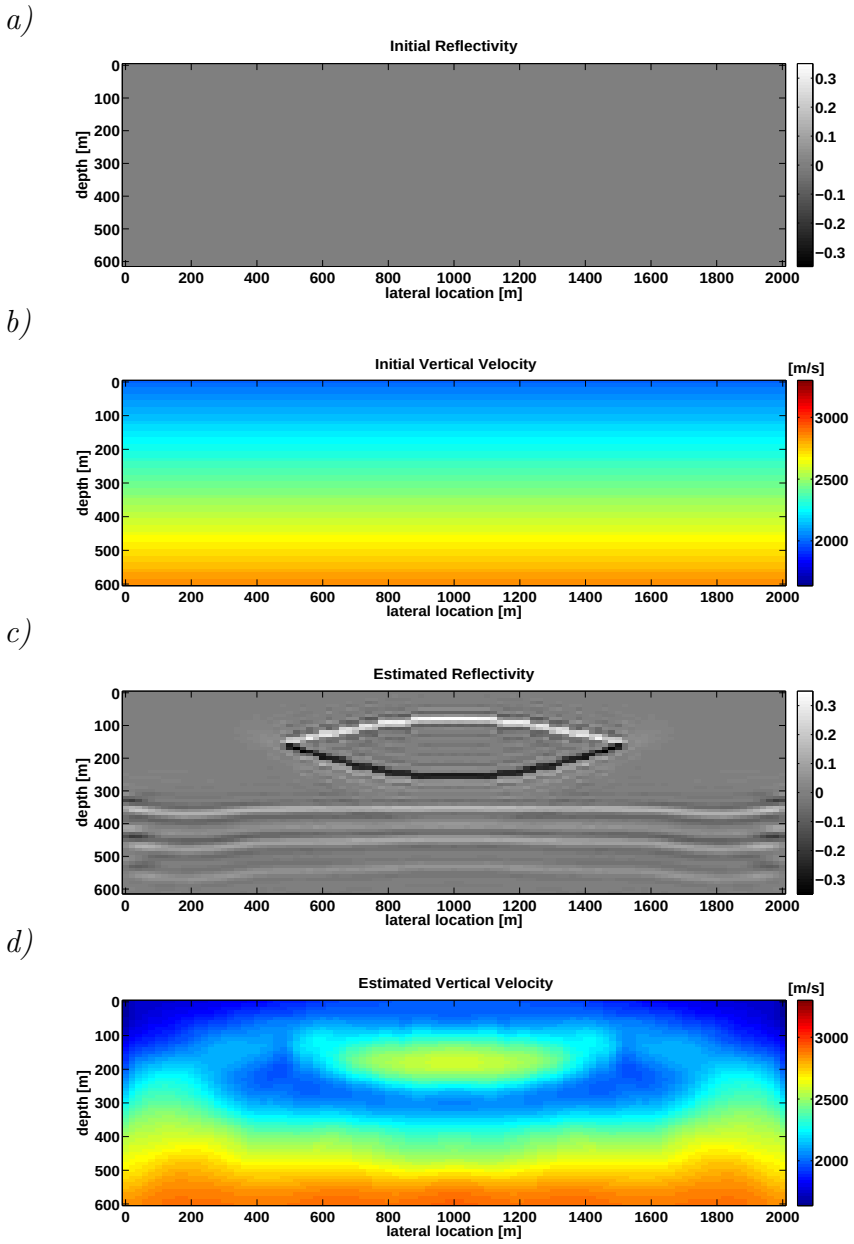

Figure 4.2: *The initial values for a) the reflectivity and b) the vertical velocity V_v [m/s]. The inverted values for c) the reflectivity and d) the vertical velocity V_v [m/s] assuming a known anisotropic parameter distribution for δ and ϵ.*

a)

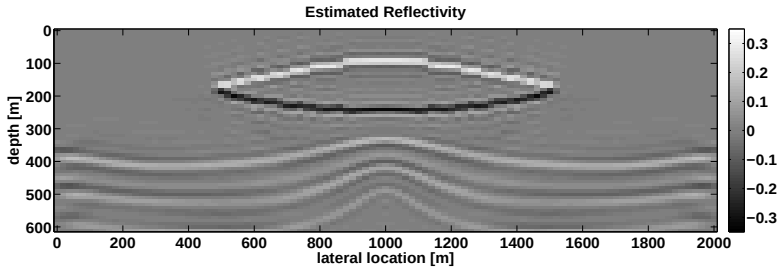

b)

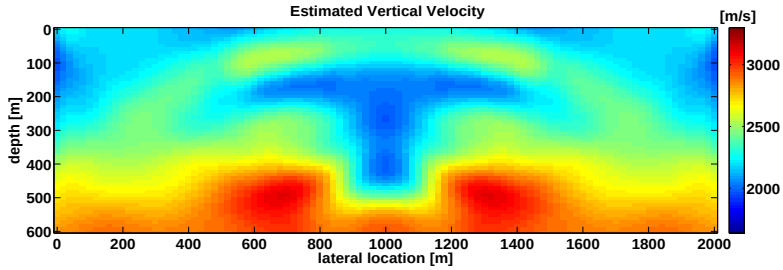

c)

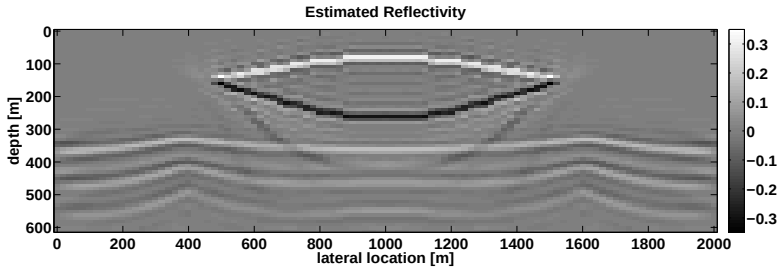

d)

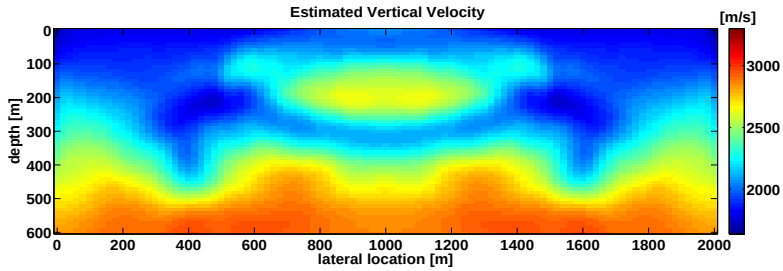

Figure 4.3: *The inverted values for a) the reflectivity and b) the vertical velocity V_v [m/s] assuming an isotropic subsurface ($\delta = 0$ and $\epsilon = 0$). The inverted values for c) the reflectivity and d) the vertical velocity V_v [m/s] when only primaries are considered in the inversion (δ and ϵ are known), such that multiples are not accounted for and are treated as noise.*

4.2 Example 2: Layered Model

For the second example we test the entire inversion algorithm where we estimate $\mathbf{R}$, V_v, and V_h, while a smooth version of δ is assumed to be known. The model is a layered model that is $2000m$ wide and $500m$ deep, the first layer is isotropic while the rest of the model is anisotropic (figure 4.4).

A total of 101 shots were generated at the surface at equal intervals. As in the previous example we generate a Ricker wavelet with a peak frequency of $30Hz$ as the source wavelet. The receivers span the $2000m$ section at $20m$ intervals. We place a $500m$ taper on each side of the model in order to reduce the edge effects and and minimize the effect of insufficient illumination.

the initial reflectivity is set to zero, while the initial velocity models are linearly increasing (figure 4.5). Note that the initial model is very different from the true model. For example, at the bottom of the model there is more than $1000m/s$ difference between the true and initial V_h.

Following the proposed hierarchal approach, we initially invert for $\mathbf{R}$ and V_v, and only after achieving convergence we include V_h inversion. Figure 4.6 shows the inverted results. Both the vertical and horizontal velocities are a smooth version of their true counterparts, as expected, while the reflectivity is an accurate band-limited representation of the true model. Thus, it is demonstrated that the initial model can be quite wrong, while still satisfactory inversion results are obtained. Finally, note that no correct velocity is estimated below the deepest reflector, as expected, as JMI uses only reflection energy.

a)

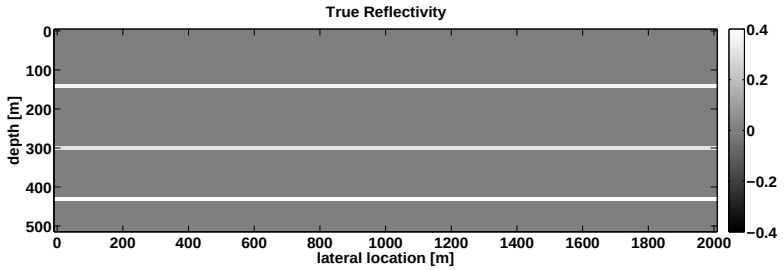

b)

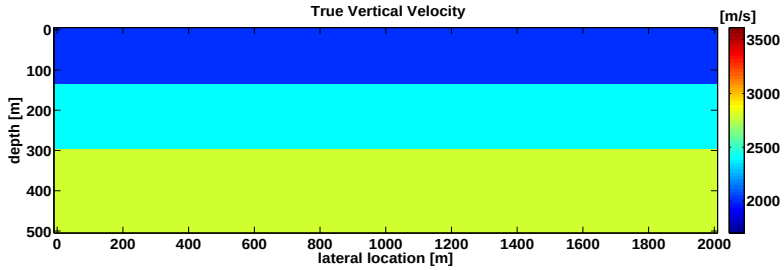

c)

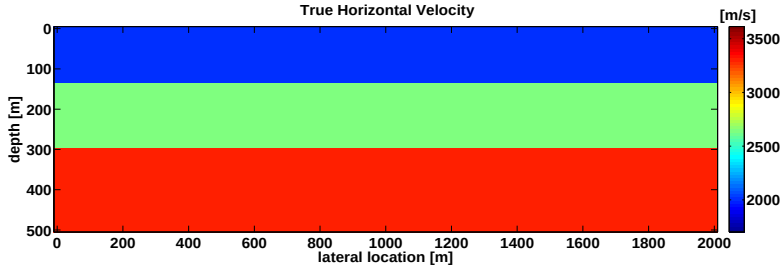

d)

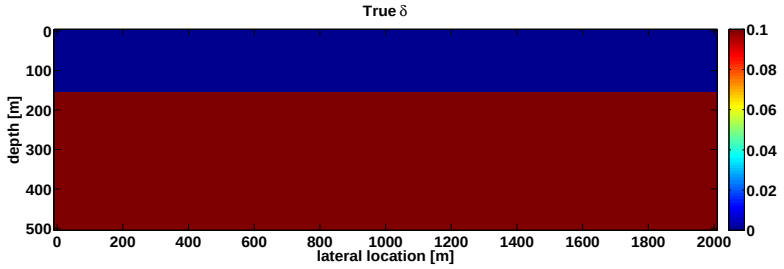

Figure 4.4: *The true values for a) the reflectivity, b) the vertical velocity V_v [m/s], c) the horizontal velocity V_h [m/s], and d) the δ parameter.*

a)

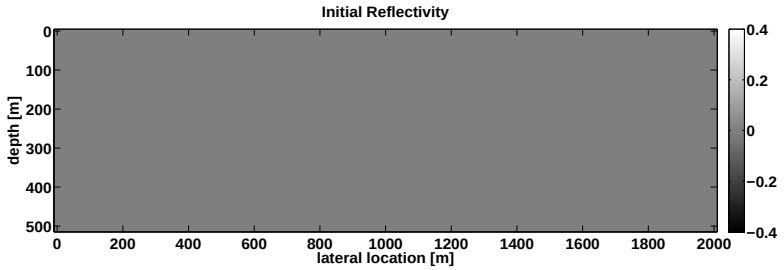

b)

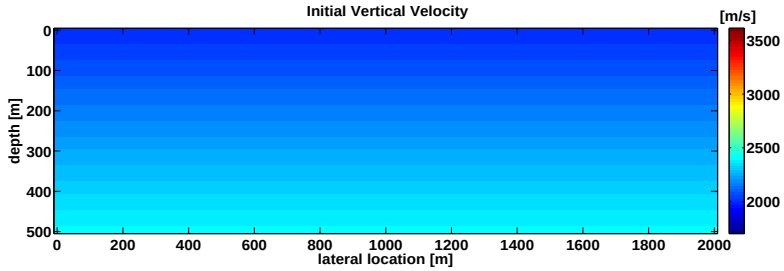

c)

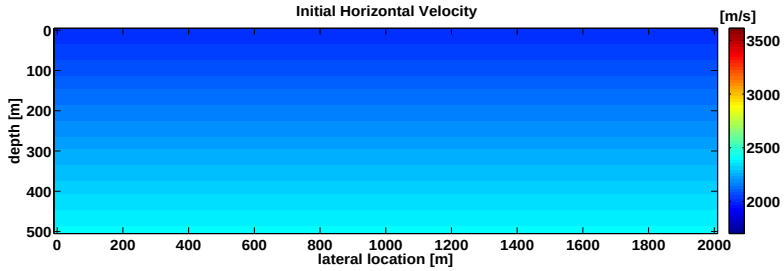

Figure 4.5: *The initial values for a) the reflectivity, b) the vertical velocity V_v [m/s], and c) the horizontal velocity V_h [m/s].*

a)

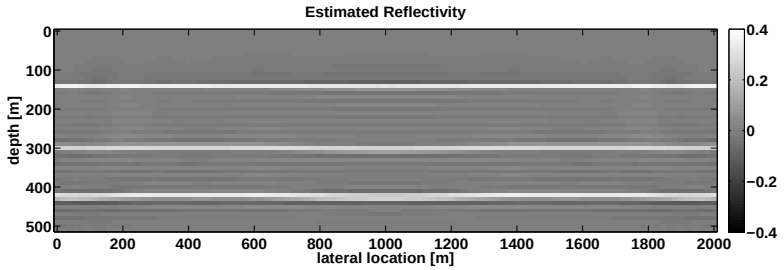

b)

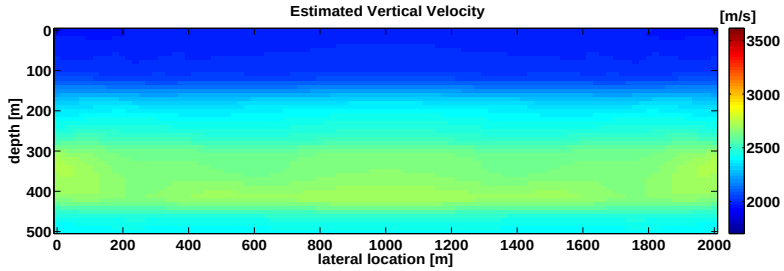

c)

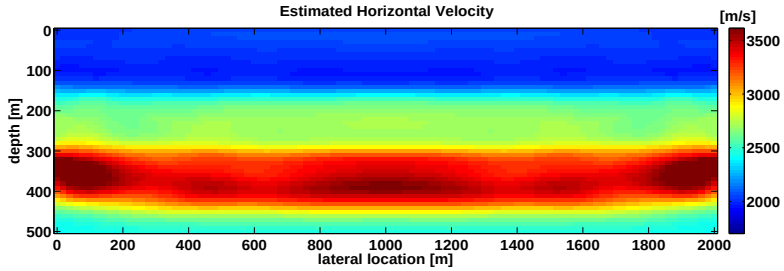

Figure 4.6: *The inverted values for a) the reflectivity, b) the vertical velocity V_v [m/s], and c) the horizontal velocity V_h [m/s].*

4.3 Example 3: Elastic Anisotropic Model

The acoustic anisotropic dispersion relation (equation 2.1.15) provides a good approximation for the VTI P-wave kinematics. However, it does not address some of the elastic effects. In the next two examples we analyze and better understand the elastic effects on the inverted results. We generate the observed data via a different modeling method, namely Finite-Difference (FD) modeling. In our simulations we make use of the open source software Seismic Unix for FD modeling. The FD implementation was elastic anisotropic 2D modeling that is 4th order in space, it is primarily based on the algorithm presented by Juhlin [1995]. Our FWMod implementation is under the acoustic assumption, while the FD implementation is under an elastic assumption. Hence, we will observe the discrepancies between the acoustic and elastic data sets in inversion.

We generate a simple elastic VTI model with constant values of $V_{P0} = 4000m/s$, $V_{S0} = 2309$, $\epsilon = 0.2$, $\delta = 0.1$. The model has a density change at $800m$, where the density changes from $\rho = 2500$ to $\rho = 3000$. Figure 4.7 shows the parameters that we are interested in inverting for, namely the reflectivity, the vertical velocity, and the horizontal velocity. A total of 150 shots were generated at the surface at equal intervals. The source wavelet is a Ricker wavelet with an average frequency of $20Hz$ as the source wavelet. The receivers span the surface at $20m$ intervals. The FD modeled data will contain converted waves as well as angle-dependent reflectivities, which will not be properly explained by the acoustic angle-independent assumption. We eliminate the direct wave and the converted waves, in order to focus on the reflected P-wave. Figure 4.10a shows the FD shot gather while figure 4.10b shows the corresponding FWMod shot gather. We normalize the energy of the FD gathers as a function of offset in order to attenuate some of the elastic effects before attempting to invert for the subsurface parameters. This model is the best case scenario, because after pre-processing the elastic data closely resembles acoustic data.

Figure 4.8 shows the starting models. Note that the vertical velocity difference is $800m/s$ over $800m$ and the horizontal velocity difference is over $1500m/s$ over the same $800m$ interval. This will create large discrepancies between the reflection arrival times between observed and calculated data sets, which will create issues in inversion if the reflectivity is not estimated at each iteration. Figure 4.9 shows the inversion results. The inversion results

are accurate except at the edges due to the poor illumination. It is interesting to note the difference between the edges and the middle of the model. We can see the effect of updating the velocities on the image. By comparing the reflector at the edges and in the middle of the model, we can see that the reflector was shifted more than $200m$.

a)

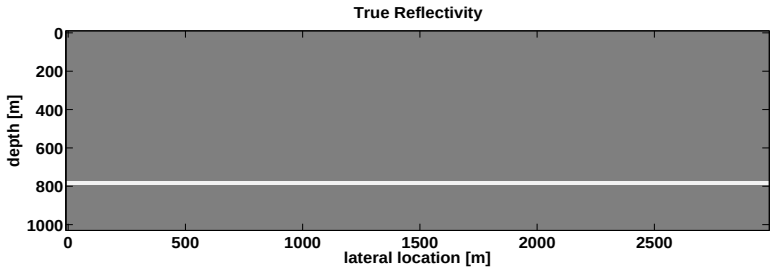

b)

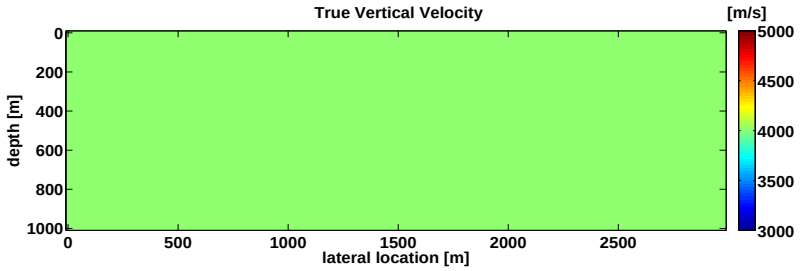

c)

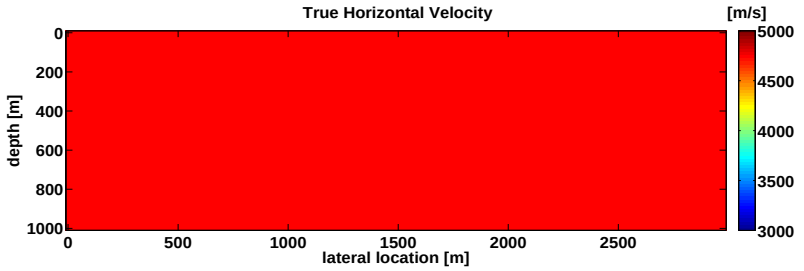

Figure 4.7: *The true values of a) the reflectivity, b) the vertical velocity V_v [m/s], and c) the horizontal velocity V_h [m/s].*

a)

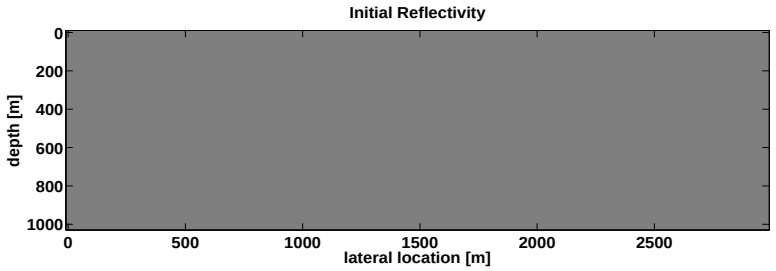

b)

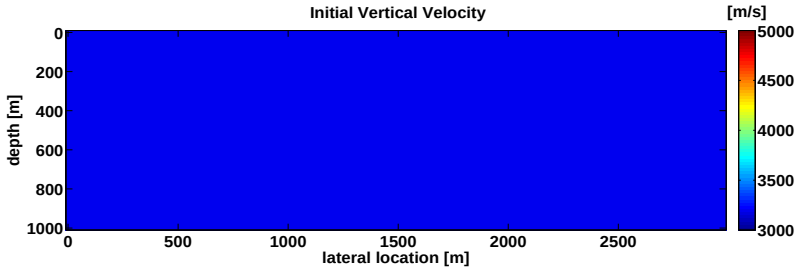

c)

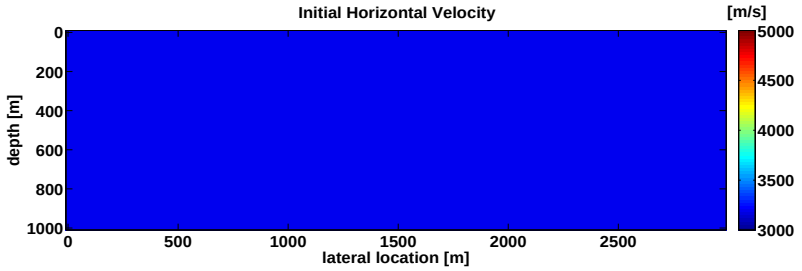

Figure 4.8: *The initial values for a) the reflectivity, b) the vertical velocity V_v [m/s], and c) the horizontal velocity V_h [m/s].*

a)

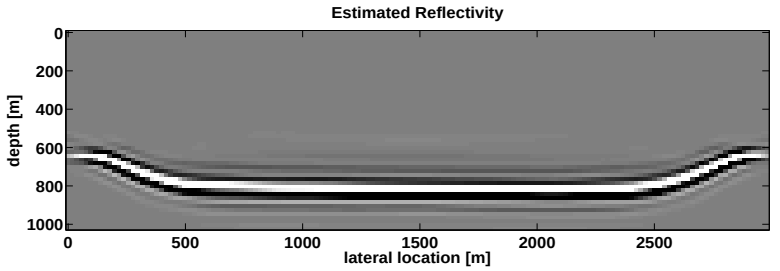

b)

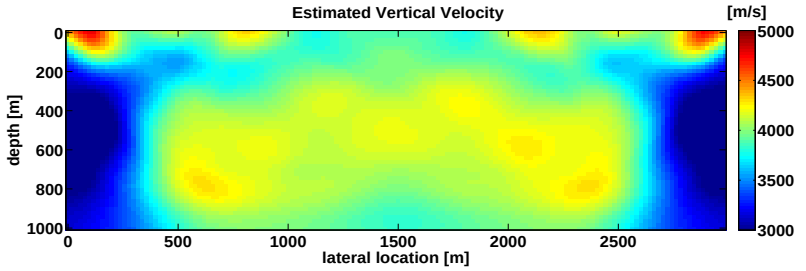

c)

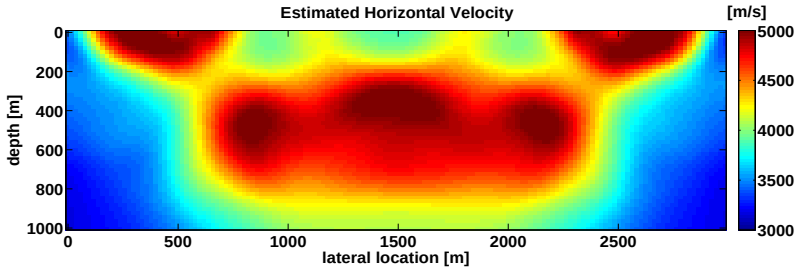

Figure 4.9: *The inverted values for a) the reflectivity, b) the vertical velocity V_v [m/s], and c) the horizontal velocity V_h [m/s].*

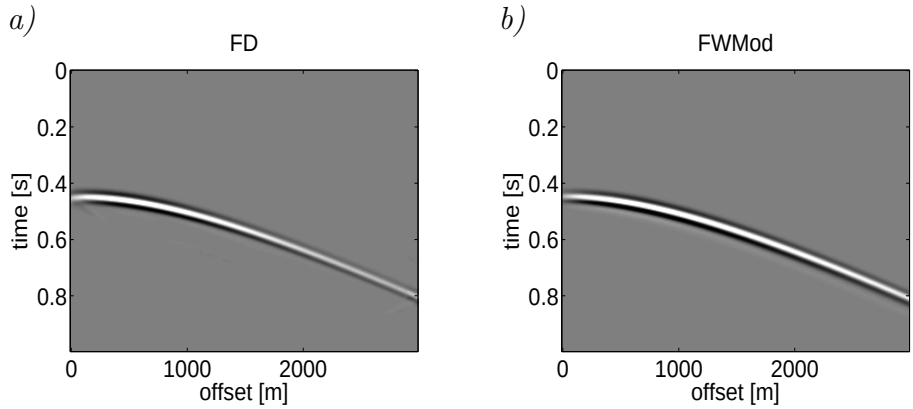

Figure 4.10: *Modeled shot gathers related to the model in figure 4.7. a) The FD shot gather. b) The FWMod shot gather.*

4.4 Example 4: Layered Elastic Anisotropic Model

The elastic model presented in this section is similar to the model presented in example 2 (figure 4.4). However, we convert the model from an acoustic model to an elastic model. In order to translate the acoustic FWMod parameters into elastic finite-difference parameters we make use of Gardner's relation to estimate the density via the P-wave velocity values [Gardner et al., 1974]. As for the S-wave velocity we take it to be half the P-wave velocity. The rest of the parameters can be directly translated into their elastic finite-difference counterparts. Figure 4.11 shows the density, P-wave velocity, S-wave velocity, and ϵ used to generate the elastic anisotropic finite-difference data. Note that δ is the same as in figure 4.4d.

Figure 4.12a shows one shot gather (in the middle of the section) obtained via elastic anisotropic finite-difference modeling (after surface wave removal). There are some significant elastic features, chief among them is the angle-dependent reflectivities and the presence of converted waves (a prominent converted wave arrives at $t \approx 0.58$). The variations in amplitude in the elastic data would cause significant errors in inversion. This is because the method is based on minimizing the error between the observed and modeled

data and it will allocate more effort in minimizing the large amplitudes while ignoring weaker events. Running anisotropic JMI on the raw data sets produces inferior results. Analyzing the estimated data's shot gather generated from the last iteration we can see that many of the elastic effects are not explained. Figure 4.12b shows the estimated shot gather from the last iteration of JMI. It corresponds to the same shot gather in figure 4.12a.

In order to understand the elastic effects we take the $\tau - p$ transform of both the observed data used for inversion and the estimated data provided from the final iteration of anisotropic JMI. Figure 4.12a shows the observed data and figure 4.12b estimated data in the time space domain, while figure 4.12d and figure 4.12e show their $\tau - p$ transforms respectively.

In this domain the angle-dependent features are better identifiable. We can also distinguish the converted wave from the P-wave arrivals. We normalize the observed data, to make it more comparable to the estimated data (figure 4.12f), then we convert it back to the time-space domain (figure 4.12c). We use this normalized data as input for anisotropic JMI and rerun the inversion.

The initial reflectivity and velocities are the same as the ones used in the previous example (figure 4.5). Figure 4.13 shows the inverted reflectivity, vertical velocity, and horizontal velocity. We note that the layering is visible in the velocity models, both the first and second layers are comparable to their true counterparts. However, the third layer is of much lower quality, and we see that the estimated horizontal velocity is lower than its true counterpart.

Looking at the shot gather we can see that the flanks of the primary event associated with the third reflector intertwine with the flanks of the primaries from the first and second reflectors at the far offsets. We believe that the strong amplitude elastic effects in the flanks overshadows a significant portion of the anisotropic kinematics of the third layer. Nevertheless, the image is accurate and the layering is visible in both V_V and V_h despite the simplified modeling algorithm.

a)

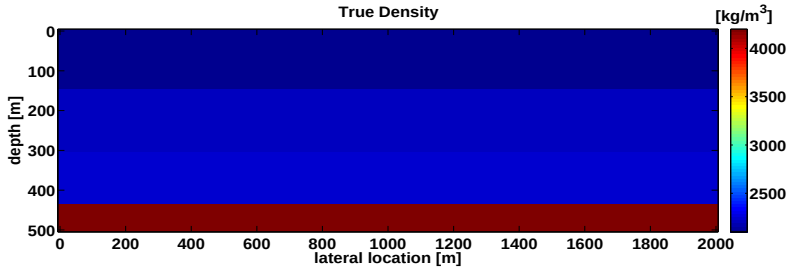

b)

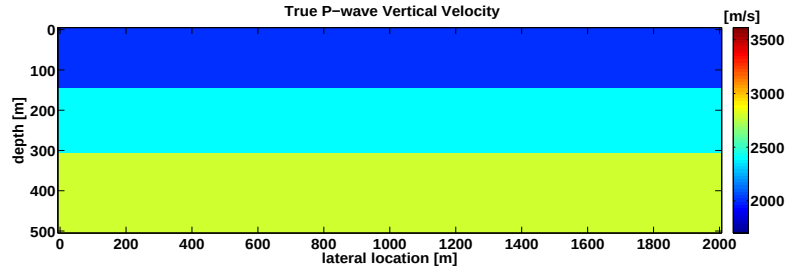

c)

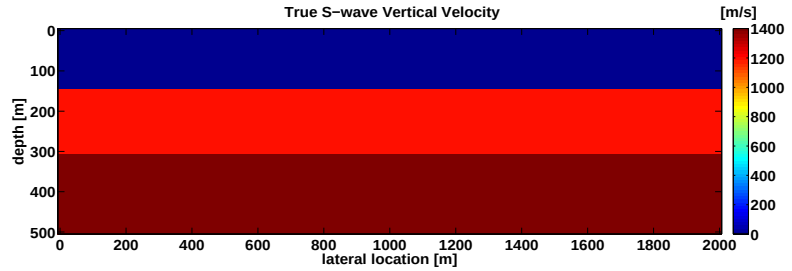

d)

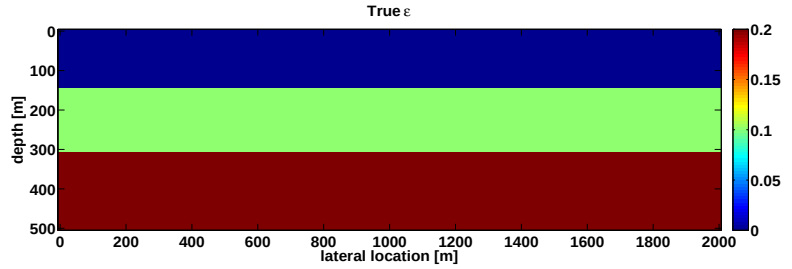

Figure 4.11: *The true values for a) the density [kg/m^3], b) the P-wave velocity along the symmetry axis [m/s], c) the S-wave velocity along the symmetry axis [m/s], and d) the ϵ field.*

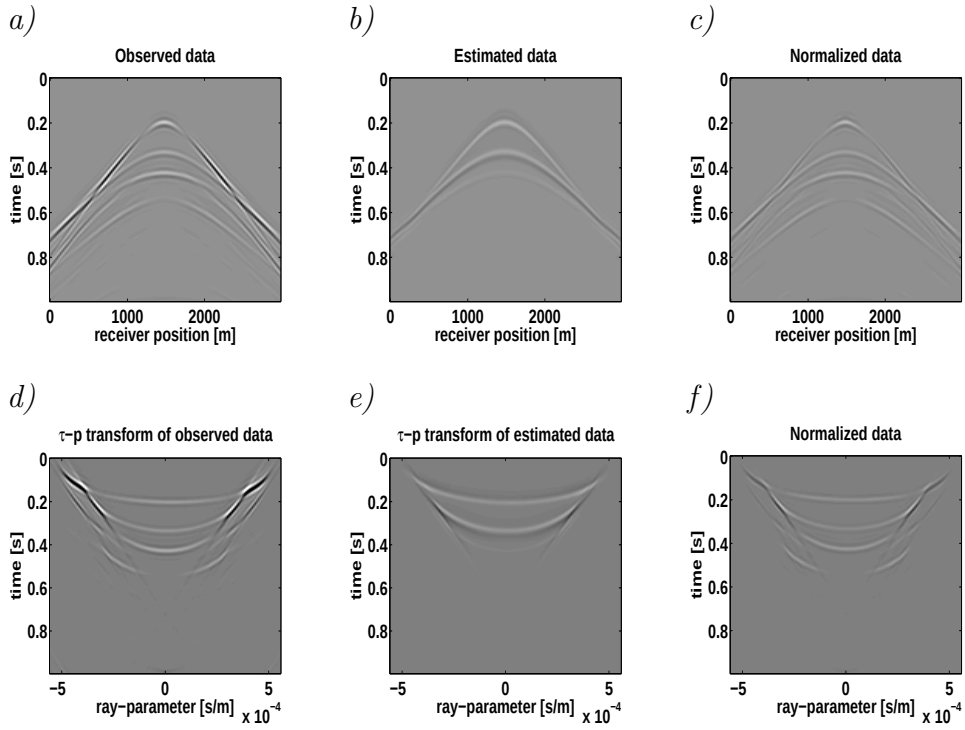

Figure 4.12: *Normalizing the data. a) The observed shot gather obtained via anisotropic elastic finite-difference. b) The estimated shot gather obtained via anisotropic JMI. c) The observed shot gather after normalization. d) The $\tau - p$ transform of the observed shot gather in a). e) The $\tau - p$ transform of the estimated shot gather in b). f) The normalization in the $\tau - p$ domain of the observed shot gather in d).*

a)

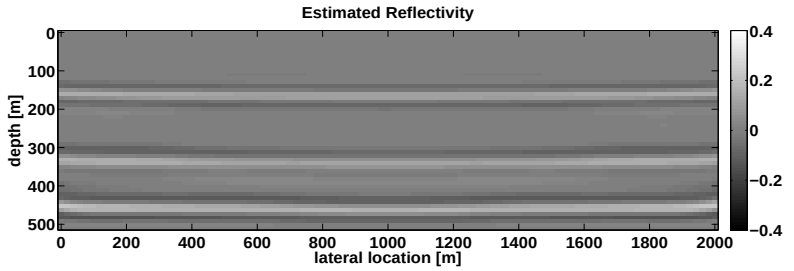

b)

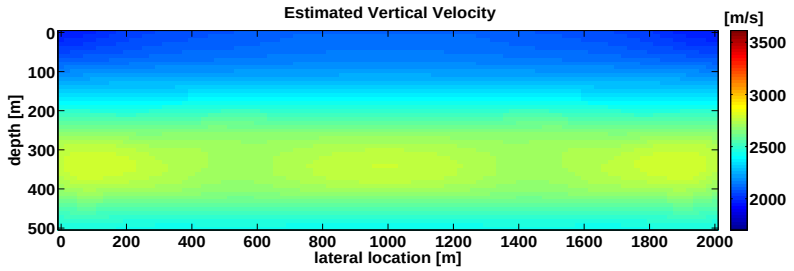

c)

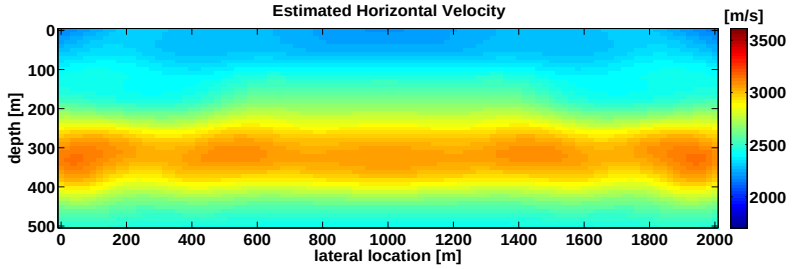

Figure 4.13: *The inverted values for a) the reflectivity, b) the vertical velocity V_v [m/s], and c) the horizontal velocity V_h [m/s] using elastic data.*

4.5 Example 5: Internal Multiple Model

In order to analyze the effects of internal multiples in this inversion, we generate a model that promotes the generation of strong internal multiples. Figure 4.14 shows the true reflectivity, vertical velocity, horizontal velocity, and δ values. The strong internal multiples are generated by the high reflectivity of the second layer (between $160m$ and $350m$). The multiples mask the weaker primaries that are generated underneath (from $350m$ and onwards). A total of 151 shots were generated at the surface at equal intervals. The source wavelet is a Ricker wavelet with a peak frequency of $30Hz$. The receivers span the $3000m$ section at $20m$ intervals.

The initial velocity models are 1D linearly increasing models as given in figure 4.15, while the initial reflectivity is set to zero. As in the previous case we initially only invert for $\mathbf{R}$ and V_v, and after achieving convergence we include V_h inversion. Figure 4.16 shows the inversion results. The estimated velocity models are a smoothed version of their true counterparts. Note that a smoothed version of the high velocity anomaly and the low velocities underneath are recovered. Also note that the results degrade towards the edges of the model due to the limited illumination.

We repeat the inversion using the same initial model. However, we limit the inversion to primaries-only. Although, internal multiples are present in the observed data, they will not be addressed in inversion and will be considered as noise. In this example the multiples ring through the record and mask the weak primaries. Figure 4.17 shows the primaries-only inversion results. Comparing the primaries-only inversion velocities with the full wavefield inversion velocities, we note that the velocities in the area below the high velocity anomaly are overestimated.

We believe that this is due to the cross-talk between the primaries and internal multiples. Since the internal multiples have larger amplitudes than the deeper primaries, they will contribute more towards a velocity update compared to the deep primaries. The velocities are generally overestimated below layer 2. Consequently, the corresponding image shows that the internal multiples are well focused but at the wrong location. Furthermore, they are masking the primaries.

a)

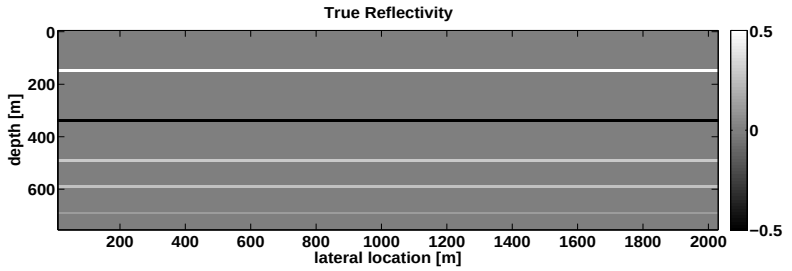

b)

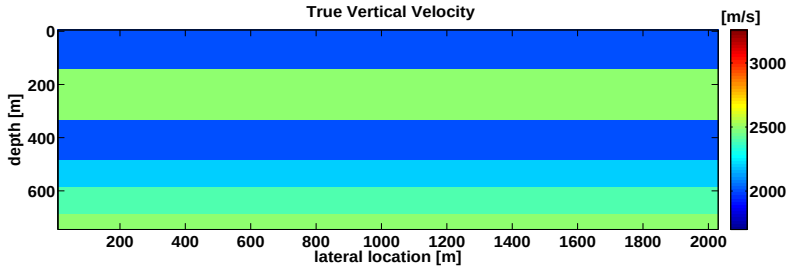

c)

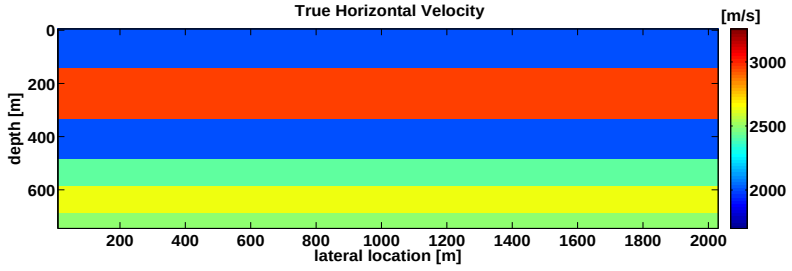

d)

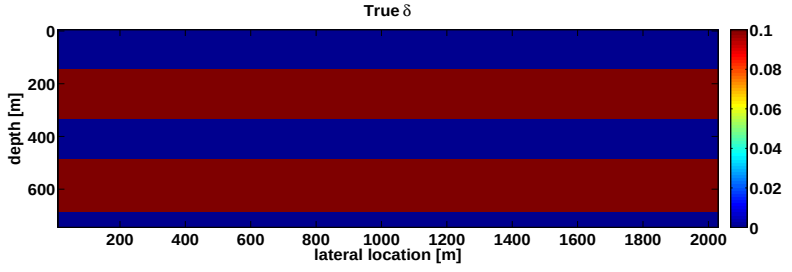

Figure 4.14: *The internal multiples model. a) The reflectivity, b) the vertical velocity V_v [m/s], c) the horizontal velocity V_h [m/s], and d) the δ values.*

a)

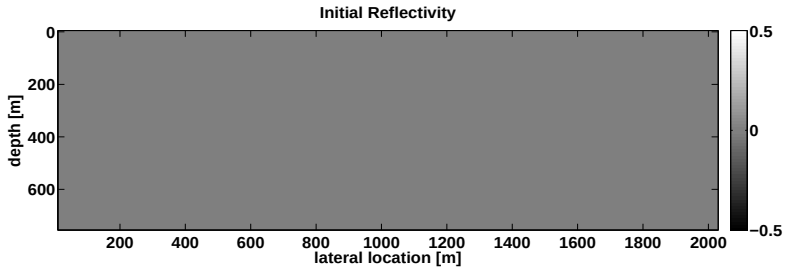

b)

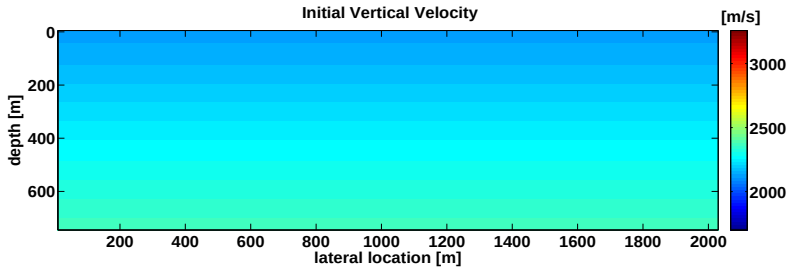

c)

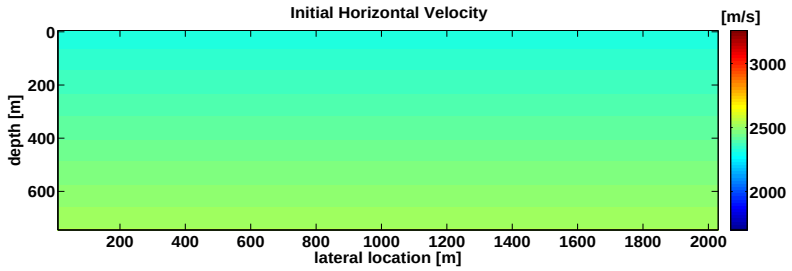

Figure 4.15: *The initial values used for inversion. a) The reflectivity, b) the vertical velocity V_v [m/s], and c) the horizontal velocity V_h [m/s].*

Finally, we consider the case where only primaries are modeled and inverted. There are no internal multiples in the observed data, i.e. we assume that they were perfectly removed and, therefore, they will not have any contribution in the inversion. We recompute the observed data and limit it to a single roundtrip of FWMod in order to model the primaries-only.

We then start the inversion with the same set of starting parameters as in

a)

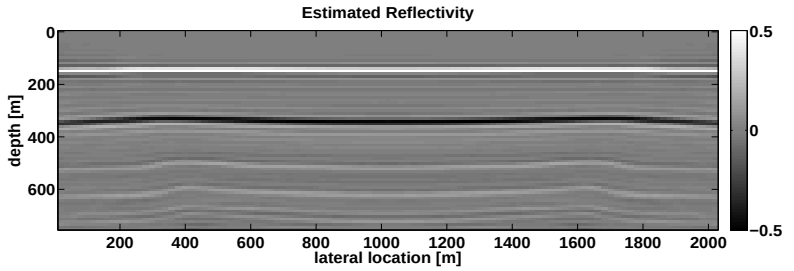

b)

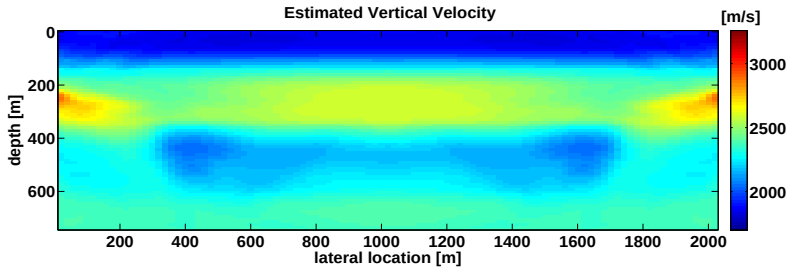

c)

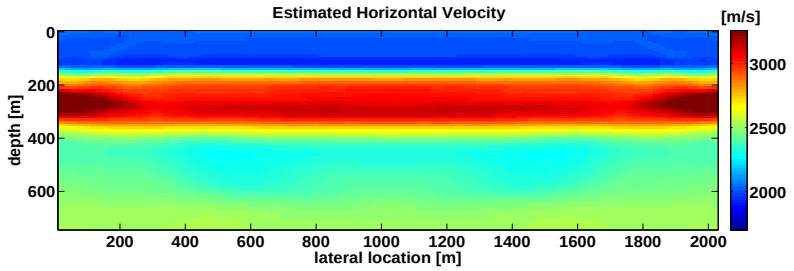

Figure 4.16: *The inverted values using primaries and internal multiples. a) The reflectivity, b) the vertical velocity V_v [m/s], and c) the horizontal velocity V_h [m/s].*

the previous examples. Figure 4.18 shows the inverted reflectivity, vertical velocity, and horizontal velocity. There are a couple of interesting features. First, it appears that the trade-off issue is still there, meaning that the vertical velocity is overestimated while the horizontal velocity is underestimated compared to figure 4.16.

a)

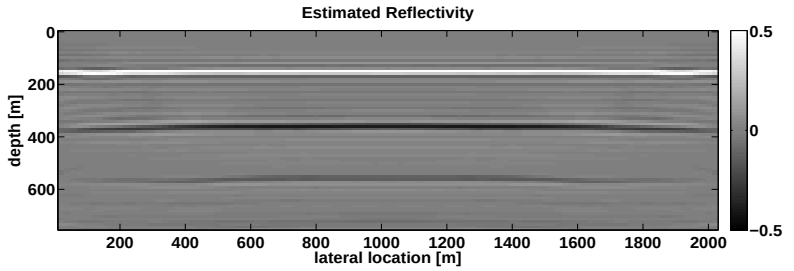

b)

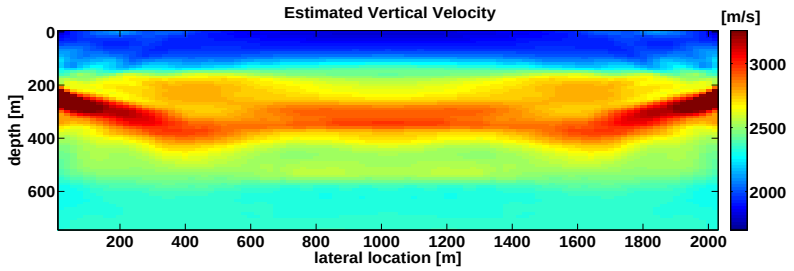

c)

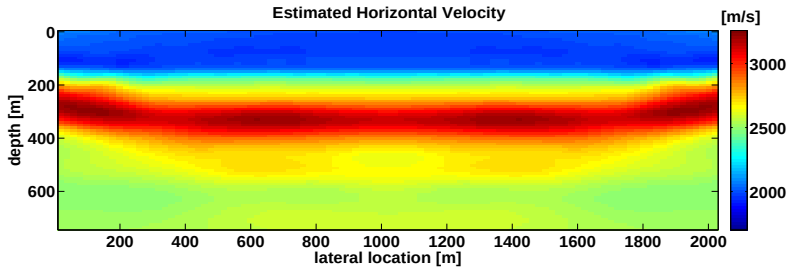

Figure 4.17: *The inverted values when only primaries are considered in inversion. a) The reflectivity, b) the vertical velocity V_v [m/s], and c) the horizontal velocity V_h [m/s].*

This suggests that the internal multiples added the extra sensitivity in both the velocity estimates. Note that the image suffers due to the trade-off, the events are a bit deeper compared to their true counterparts. The second observation is that the reflections underneath the high velocity layer are mapped too deep because of the vertical velocity being overestimated. Despite the

a)

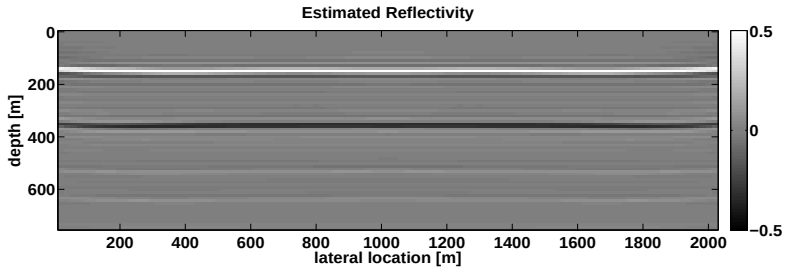

b)

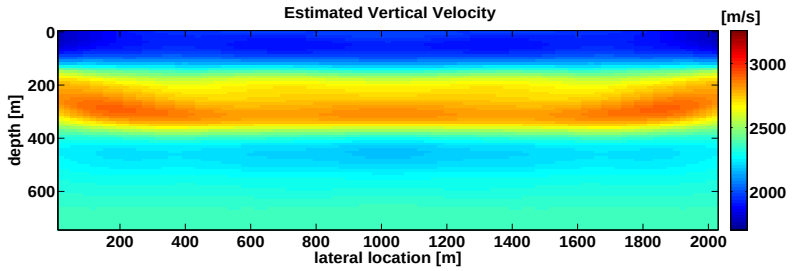

c)

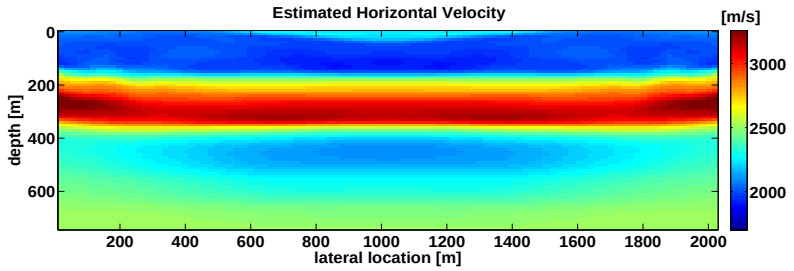

Figure 4.18: *The inverted values when only primaries are modeled in the observed data. a) The reflectivity, b) the vertical velocity V_v [m/s], and c) the horizontal velocity V_h [m/s].*

absence of internal multiples in the observed data, the invertion results are of lower quality. This is due to the trade-off occurring between the vertical velocity and the horizontal velocity.

4.6 Example 6: HESS VTI Model

The previous examples demonstrate the performance of the inversion algorithm on a number of simplified models in order to understand and analyze isolated effects. In this section we validate our theory on a more realistic and complex model, the so-called Hess VTI model. This model was generated in the late 1990s by the Amerada Hess Corp, who consider it to be representative of several exploration areas in the Gulf of Mexico. The magnitude of anisotropy is considered to be moderate to strongly anisotropic [Tsvankin, 2012]. We consider only part of the model containing the fault. We disregard the salt due the limited recording aperture, which causes limited illumination on some parts of the salt [Han et al., 2000; Tsvankin, 2012]. We also subsample and rescale the model in order to reduce the computational cost involved in inversion.

Figures 4.19 shows the true reflectivity, vertical velocity, horizontal velocity, and δ models. The acquisition configuration is a fixed spread survey with 87 equally spaced shots at the surface, the receivers are also located at the surface at $20m$ intervals. We generated a Ricker wavelet that has a peak frequency at $30Hz$ as the source wavelet. Note that the minimum frequency used in inversion is $5Hz$ while the maximum frequency used is $80Hz$, we zeroed-out any frequencies that were not in that range.

We generated two 1D linear models as the initial velocity models for the vertical and horizontal velocities, while the initial reflectivity was set to zero (figure 4.20). We invert for the reflectivity and vertical velocity first, and we include the horizontal velocity estimation only after we achieve convergence. Figures 4.21 shows the final inversion results. We notice that the image is band-limited but corresponds well to the true image, whereas the velocities are a smoothed version of their true counterparts, as expected. Note that internal multiples were addressed in the inversion method, as they no longer appear as significant artifacts in the image or the velocities. Also note that the fault is reasonably well represented in both velocity models.

Thus, we conclude that anisotropic JMI delivers good models for both the vertical and horizontal velocities (where δ is assumed to be known). Note that the method allows internal multiples to contribute towards the estimated models and that initial models can have large velocity errors.

a)

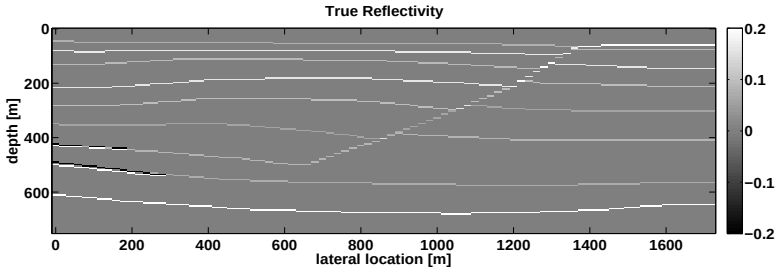

b)

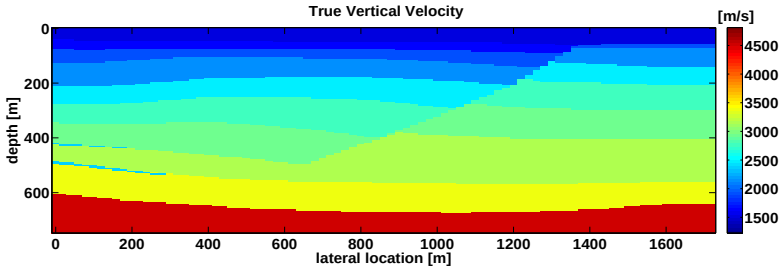

c)

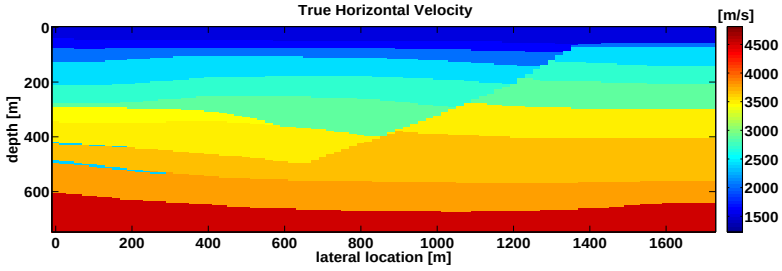

d)

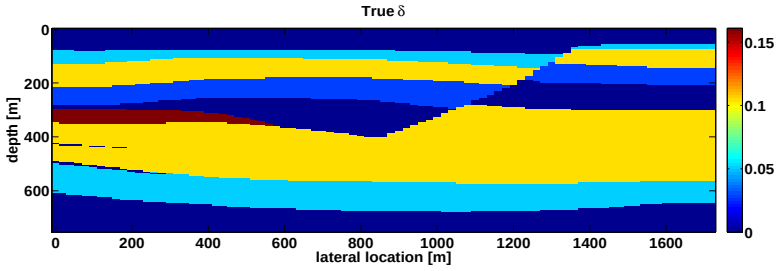

Figure 4.19: *Subset of the Hess VTI model. a) The reflectivity, b) the vertical velocity V_v [m/s], c) the horizontal velocity V_h [m/s], and d) the δ values.*

a)

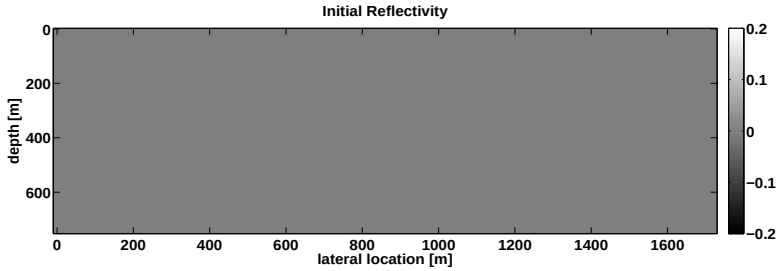

b)

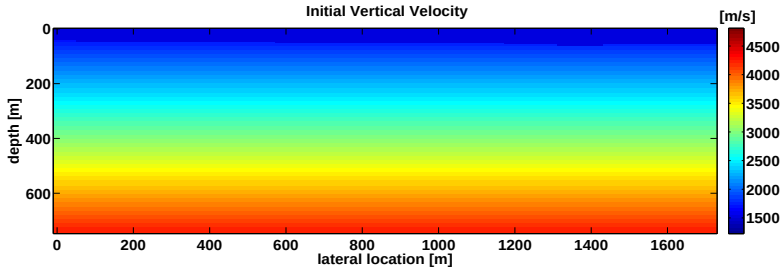

c)

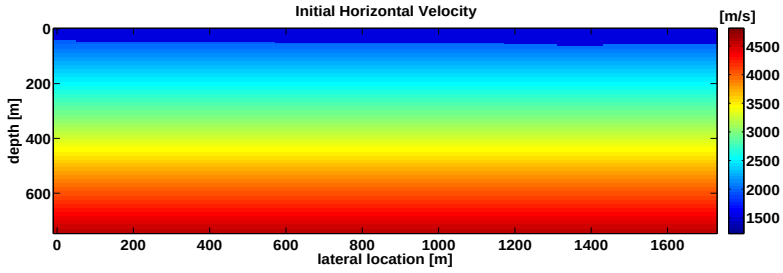

Figure 4.20: *The initial values used for inversion. a) The reflectivity, b) the vertical velocity V_v [m/s], and c) the horizontal velocity V_h [m/s].*

a)

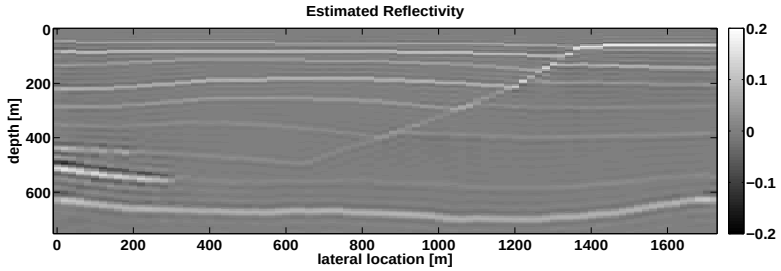

b)

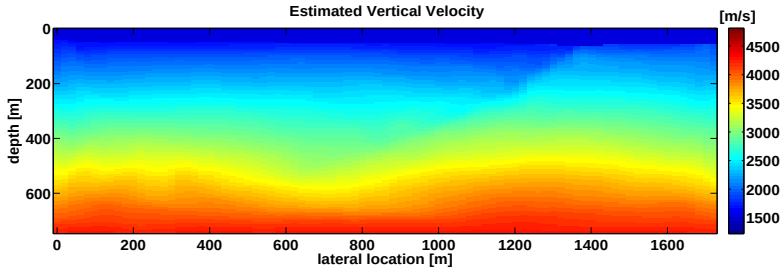

c)

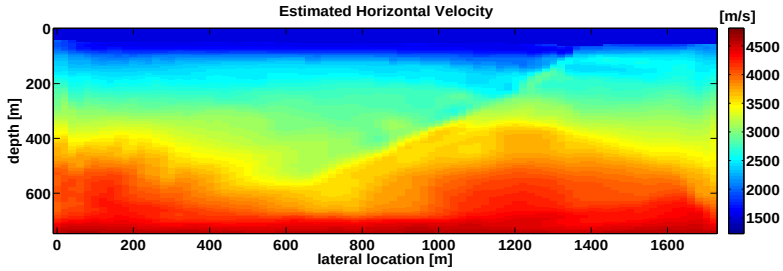

Figure 4.21: *The inverted values, a) The reflectivity, b) the vertical velocity V_v [m/s], and c) the horizontal velocity V_h [m/s].*

5

Field Data Example

This chapter illustrates the application of anisotropic JMI on a 2D marine field data set from the North Sea. Our aim is to automatically estimate the reflectivities, vertical velocities, and horizontal velocities of the subsurface.

5.1 Pre-processing

The seismic reflection data that we invert is a 2D streamer data that was acquired from the North Viking Graben in the North Sea [Keys and Foster, 1994]. The data is publicly available (courtesy of SEG and ExxonMobil) and is commonly referred to as the "Mobil AVO dataset". The data consists of 1001 shots with a shot spacing of $25m$. The receiver spacing is also $25m$. The recording time is $6s$ and the sampling time is $0.004s$. The acquisition geometry is an off-end spread with a minimum offset of $262m$ while the maximum offset is $3237m$. We make use of reciprocity in order to transform the off-end geometry to a split-spread geometry. Furthermore, we interpolate in order to generate the near offsets via Radon interpolation [Kabir and Verschuur, 1995]. In our formulation we assume that the recorded data consists of upgoing waves only, therefore, we deghost the data. Finally, due to the large size of the data we consider a $4km$ subsection, consisting of 161 shots.

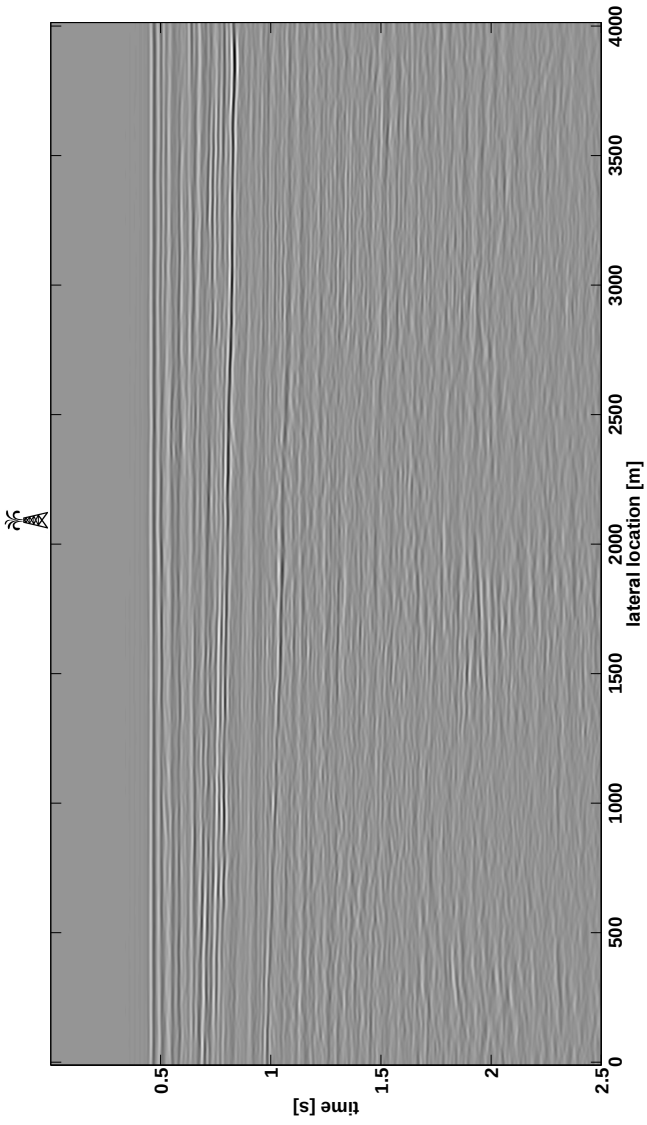

Figure 5.1: *Zero-offset section of the Viking Graben in the North Sea.*

In order to get a general idea of the geology in the region we generate a zero-offset section. Figure 5.1 shows the zero-offset section. The shallow layers are flat while the the deeper layers are gently dipping. We believe that a VTI model can be considered since most of the events are flat. We note that many of the events appearing past $1s$ are discontinuous and are of lower quality than the shallower events.

The next step lies in estimating a suitable source wavelet for inversion. We applied Estimation of Primaries by Sparse Inversion (EPSI) in order to estimate the primaries and the best fit source wavelet [van Groenestijn and Verschuur, 2009a,b]. We do not require a subsurface model at this stage since EPSI is a data-driven method. Figure 5.2a shows the estimated wavelet via EPSI. Note that we add $0.04s$ to the beginning of the seismic data in order to make it causal. Also note that we disregard the primaries in the EPSI result, we prefer a Surface-Related Multiple Elimination (SRME) approach to attenuate the surface-related multiples [Verschuur et al., 1992; Verschuur, 2006]. Therefore, we attenuate the surface-related multiples via SRME, as it turns out for these data SRME provides better surface multiple suppression, probably due to 3D amplitude effects in the data. Figures 5.2b and 5.2c show a shot gather (at the beginning of the section) before and after applying SRME. Note that many of the strong ringing surface-related multiples are suppressed. Figure 5.2c shows the residual (i.e. the surface-related multiples).

A vertical well is located at approximately the middle of the section (indicated by the drilling rig in figure 5.1). V_p, V_s, and ρ measurements were acquired starting at $1000m$ depth. Therefore, the vertical velocities are quite accurate beyond $1000m$ at the well location. However, the velocities above $1000m$ are relatively unknown. We analyze previous work done by Kabir and Verschuur [1996] in the same region. Their aim was to estimate the macro velocity model, in an isotropic framework. They corroborate their results by analyzing the Common Image Gathers (CIGs) and compare their results with the well-logs. Although they find an accurate representation for the velocity model in most parts of the section, the shallow region that we are interested in (less than $1000m$ near well A) shows inaccurate velocities, indicated by curved CIGs. Even though they estimate the best fit isotropic velocity, the CIGs are still curved which may indicate the presence of anisotropy. In this chapter we will attempt to estimate the velocities in this region under an anisotropic JMI framework, as well as investigate whether an anisotropic velocity model

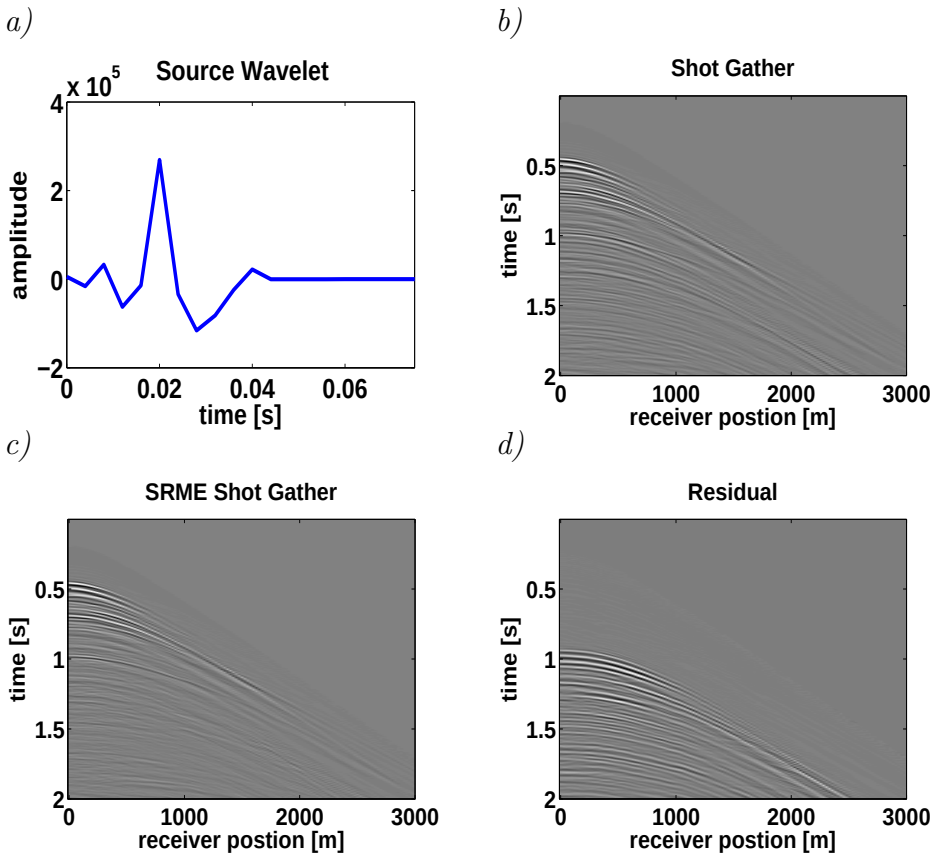

Figure 5.2: *a) The estimated source wavelet, via EPSI. b) Shot gather with multiples. c) Application of SRME on the same shot gather. d) The surface-related multiples that were attenuated.*

explains the reflection data better than an isotropic velocity model.

5.2 Anisotropic JMI

The initial isotropic velocity model for inversion is a 1D model that was generated by setting the water velocity to $1450m/s$ while the rest of the first $1000m$ is set to a constant value of $1700m/s$. Finally, we smooth the V_p velocities obtained from the well to fill the region beyond the first $1000m$. The initial isotropic model is shown in figure 5.3a. We image the data (via FWM) using the initial velocity model. Figure 5.3b shows the resulting FWM image. Note that many of the reflectors are discontinuous and are unfocused. We also generate the corresponding Angle-Domain Common Image Gathers (ADCIGs) in order to analyze the accuracy of the starting model [Sava and Fomel, 2003]. Figure 5.4 shows the ADCIGs for the initial model. Note that many of the events are curved upwards, indicating an erroneous velocity model. Also note that the deeper events, beyond $1000m$ are also curved although their values were obtained from well-logs. This may indicate erroneous overburden velocities.

We apply anisotropic JMI given the isotropic initial model in figure 5.3. We follow the same methodology presented in the synthetic examples in chapter 4. We run anisotropic JMI several times, each time taking the smoothed version of the previous result as the starting model. In total we run approximately 160 iterations of anisotropic JMI that include frequency bands that range from $2Hz$ to $40Hz$. In this example δ was set to be zero, there was no a priori information about it. Figure 5.5 shows the estimated vertical and horizontal velocity models. Figure 5.6 shows the estimated FWM image using the estimated anisotropic velocities of figure 5.5. Comparing the FWM image in figure 5.6 with the initial models image in figure 5.3b we find an improvement in the continuity and focusing of the reflectors (at approximately $800m$). Also note that the two faults are more clearly visible in the deep part of the section. The velocity models also slightly show the effect of the faults.

Figure 5.7 shows the associated ADCIGs obtained via conventional anisotropic depth migration with our estimated model. Note that the ADCIGs are fairly flat (but not perfect), indicating a suitable model. The ADCIGs are computed after anisotropic JMI in order to analyze the accuracy of inversion. They are not utilized in the inversion as in MVA. Also note that the ADCIGs still contain internal multiples, which appear as weak curved events (downward) in the background.

Figure 5.8 shows the observed data and modeled data after anisotropic JMI.

a)

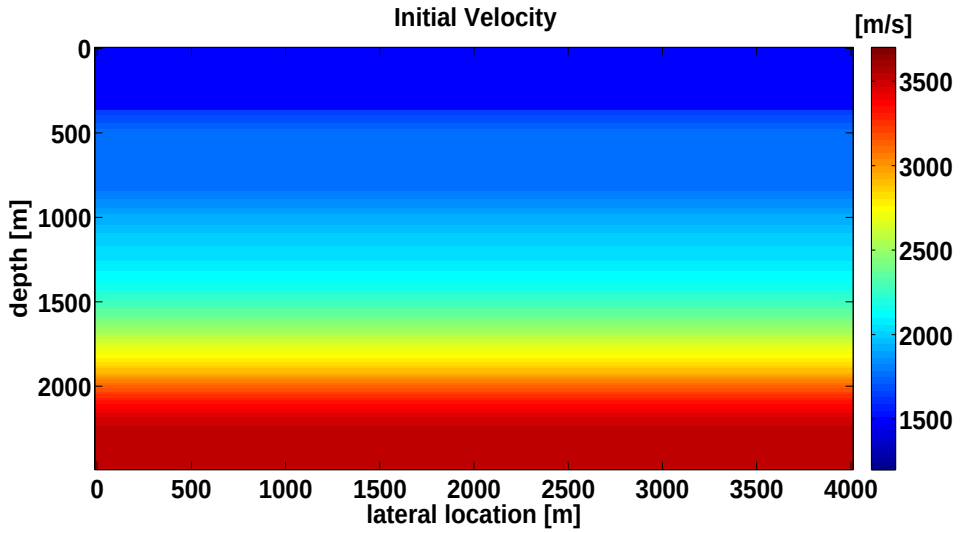

b)

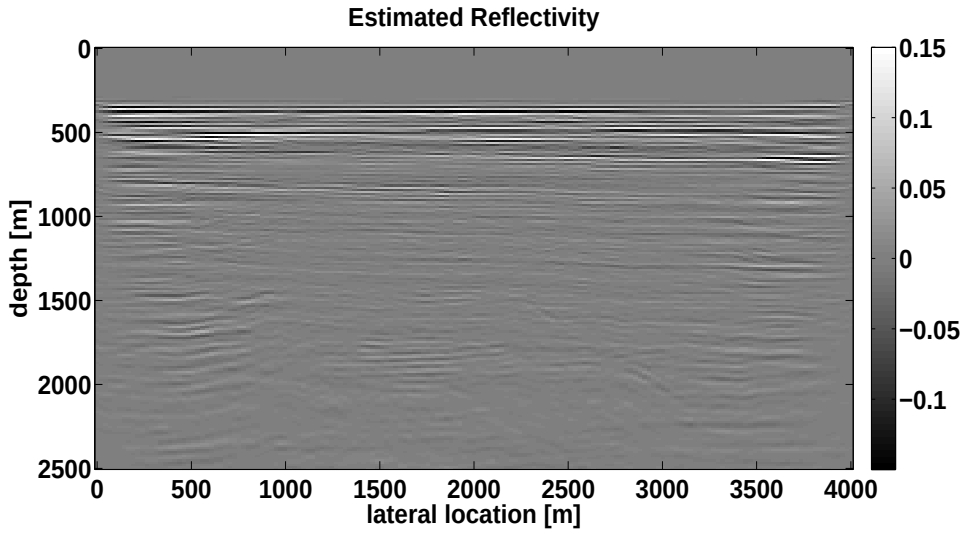

Figure 5.3: *The initial values for the isotropic velocity [m/s]. b) The FWM image obtained via the isotropic initial velocity model.*

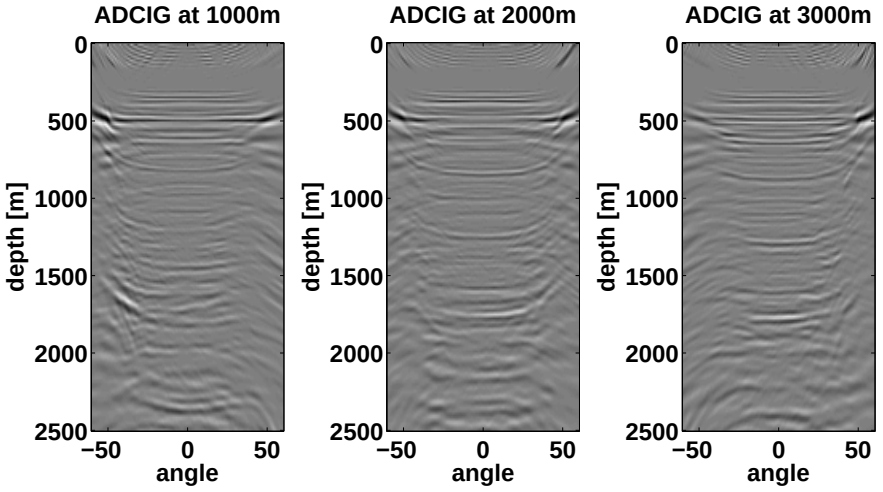

Figure 5.4: *ADCIGs associated with the initial model at lateral locations of* $1000m$*,* $2000m$*, and* $3000m$*.*

Note that most of the main reflections are explained. However, it is interesting to analyze the events that were not explained. Chief among them is a refracted wave (indicated by the arrows). The modeling method FWMod does not take it into account, therefore, it is ignored during inversion. The refracted waves can hold valuable information on the V_h parameter if one were to included them in inversion [Alkhalifah, 2016a]. Angle-dependent reflectivities and converted waves are also not explained by the method. Therefore, they do not appear in the calculated data set. Although we resort to an acoustic assumption, it adequately explains many of the events in this data set.

With the same initial model, we rerun the inversion under an isotropic assumption. We strive to keep the same procedure as in the anisotropic inversion. Hence, the number of iterations and frequency bands are the same as previously. The only difference is that the isotropic velocities will be estimated. Figure 5.9 shows the resulting isotropic velocity model and its resulting FWM image. Note that the isotropic velocity model is faster than the anisotropic velocity model at the shallow layers. This is most likely due to the isotropic assumption trying to explain the anisotropic effects. Figure 5.10 shows the associated ADCIGs. We note that the ADCIGs are very sim-

a)

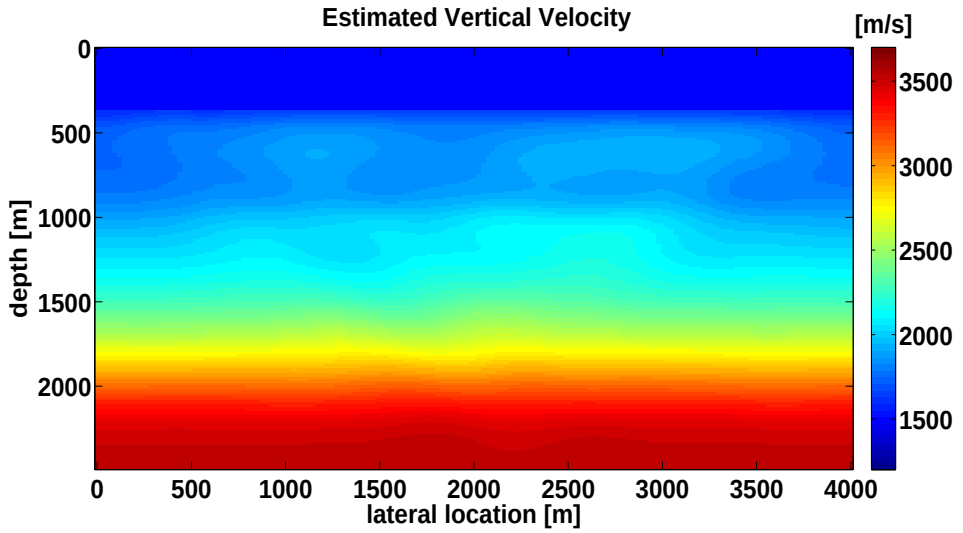

b)

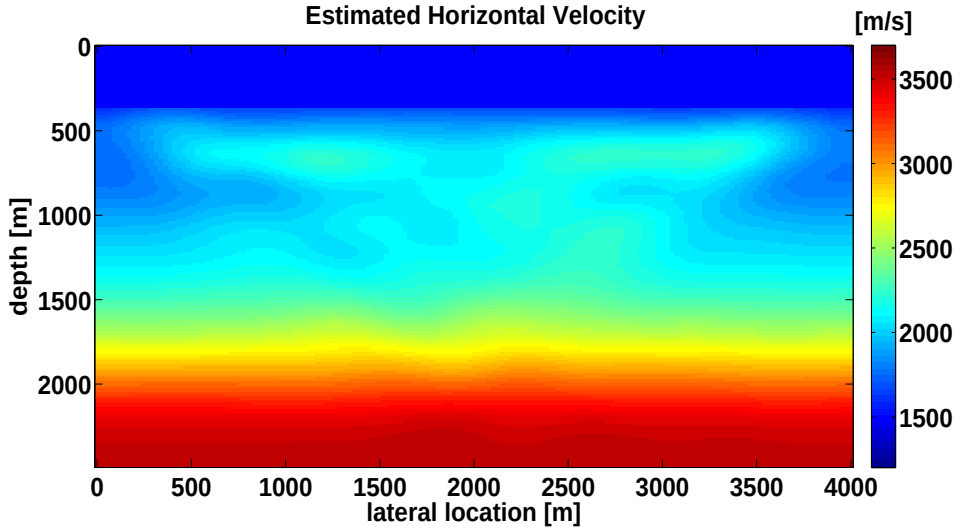

Figure 5.5: *The estimated values for a) the vertical velocity V_v [m/s] and b) the horizontal velocity V_h [m/s].*

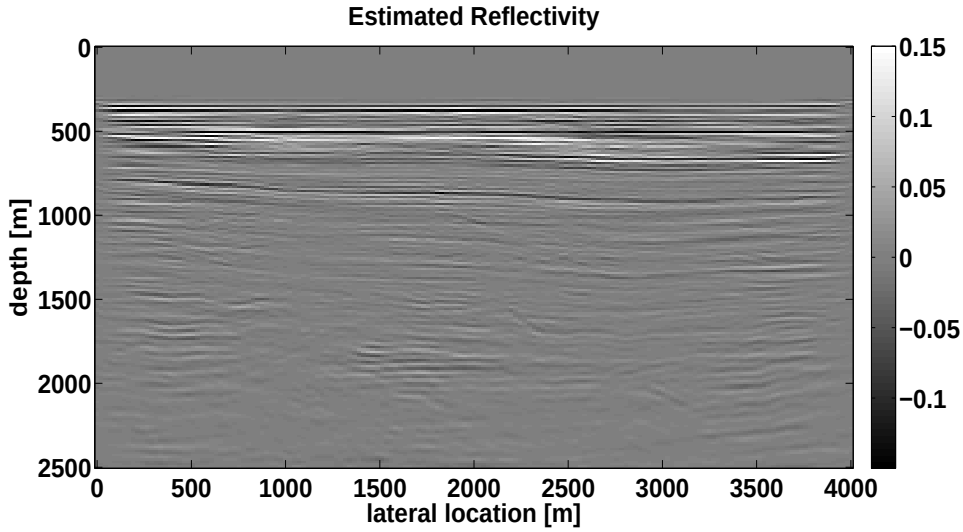

Figure 5.6: *The estimated FWM image obtained from the anisotropic models in figure 5.5.*

ilar to the anisotropic ADCIGs (figure 5.7), however, they are more curved towards higher angles. This indicates that the anisotropic velocity model was more adequate in describing the subsurface.

Finally, we analyze the effects of internal multiples. Surface-related multiples were attenuated, however, internal multiples are in the data. Anisotropic JMI will utilize them in inversion. We believe in this example the internal multiples are relatively weak due to the weak reflection coefficients. Therefore, their impact on updating the velocities is relatively weak. However, we can analyze their effects in the image. We take advantage of the imaging engine to examine different orders of scattering, such as primaries-only or primaries and internal multiples. We consider a primaries-only imaging, where we limit FWM to primary wavefield imaging (PWM) [Berkhout, 2014b; Davydenko and Verschuur, 2017]. The method will explain the primaries, but will not properly explain the internal multiples. As a consequence they will be treated as primaries, yielding cross-talk in the final image. Figure 5.11a shows the

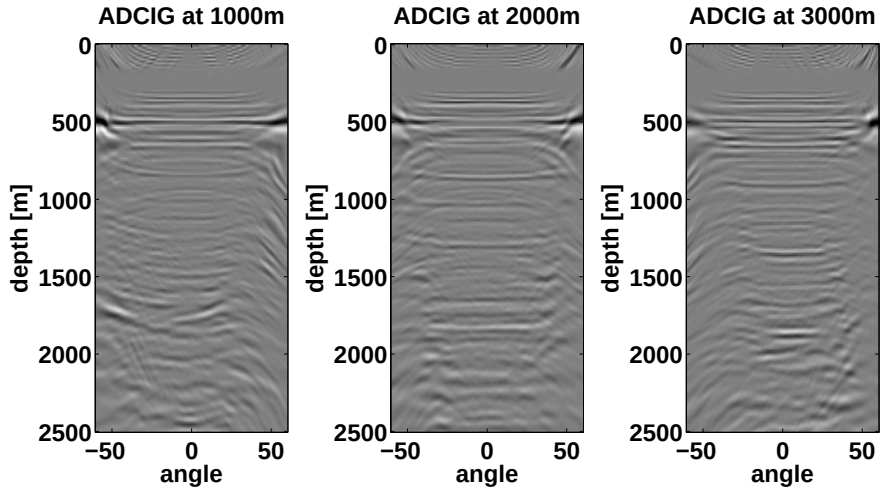

Figure 5.7: *ADCIGs associated with the anisotropic model (figure 5.5) at lateral locations of* $1000m$*,* $2000m$*, and* $3000m$*.*

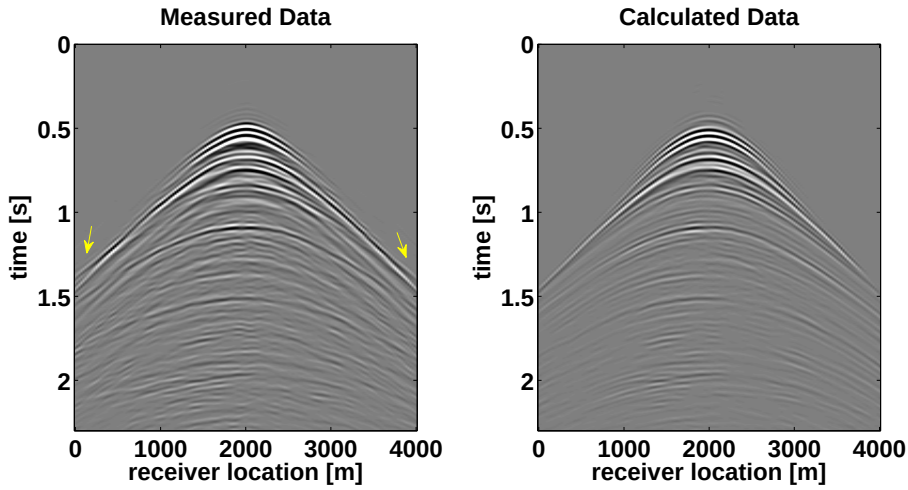

Figure 5.8: *The measured and calculated data shot gathers at* $2000m$*.*

a)

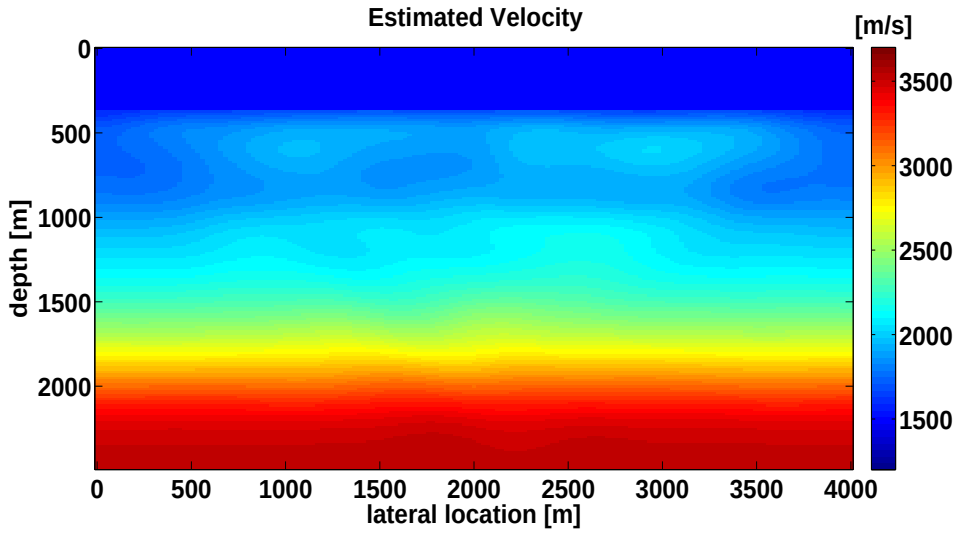

b)

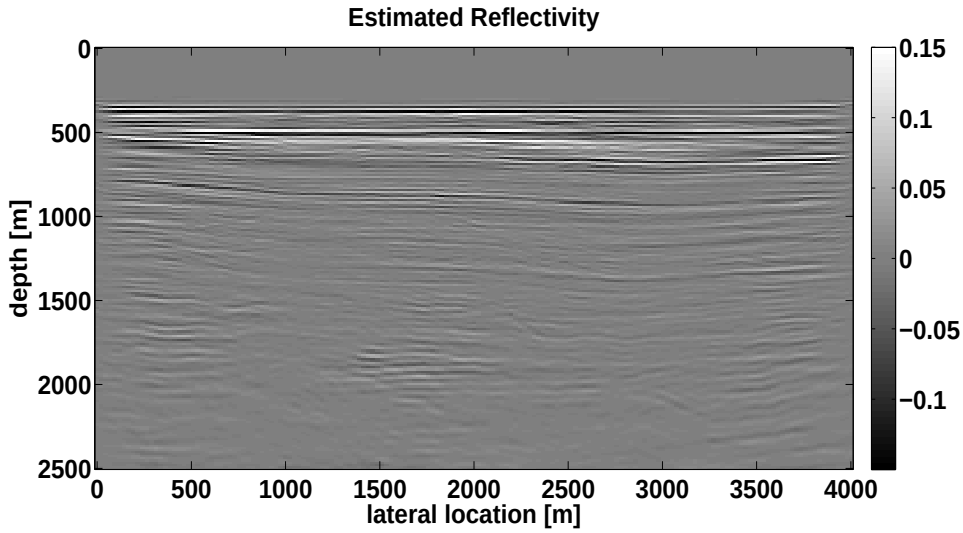

Figure 5.9: *The estimated values for the velocity V [m/s] and b) the FWM image obtained via an isotropic assumption.*

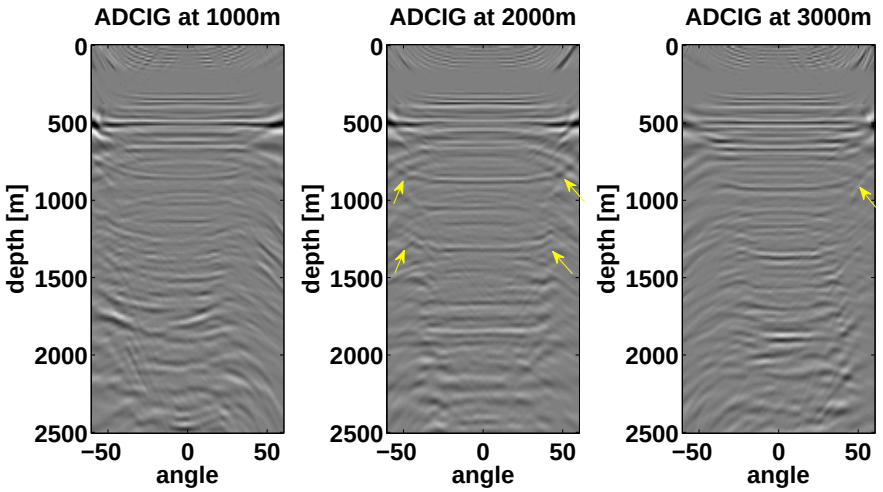

Figure 5.10: *ADCIGs associated with the isotropic model (figure 5.9) at lateral locations of* $1000m$*,* $2000m$*, and* $3000m$*.*

image after applying PWM. More events are imaged in the PWM image compared to the FWM image of figure 5.6. We compute the residual (figure 5.11b) in order to see the fine scale effects. We notice the cross-talk associated with the PWM image. Another interesting observation is that in FWM transmission effects are properly handled, whereas, the PWM image sufferers from inaccuracies in handling transmission effects. Hence, these appear in the residual on the reflectors.

This example demonstrates the effectiveness of anisotropic JMI in inversion of marine field reflection data. Our initial model was generated with the aid of well-logs. However, the well-logs only provided information beyond a certain depth (beyond $1000m$) and localized at the well location. Using anisotropic JMI we obtain estimates of the reflectivities, vertical velocities, and horizontal velocities. Analyzing the ADCIGs we find that most of the events are flat, which indicates that a suitable model was used. We rerun the inversion with an isotropic assumption and we note that the results are inferior, as indicated by the ADCIGs. Finally, we analyzed the effects of internal multiples in the image. The residual between the PWM and FWM image shows that internal multiples and transmission effects have a considerable imprint on the image if not taken into account properly.

a)

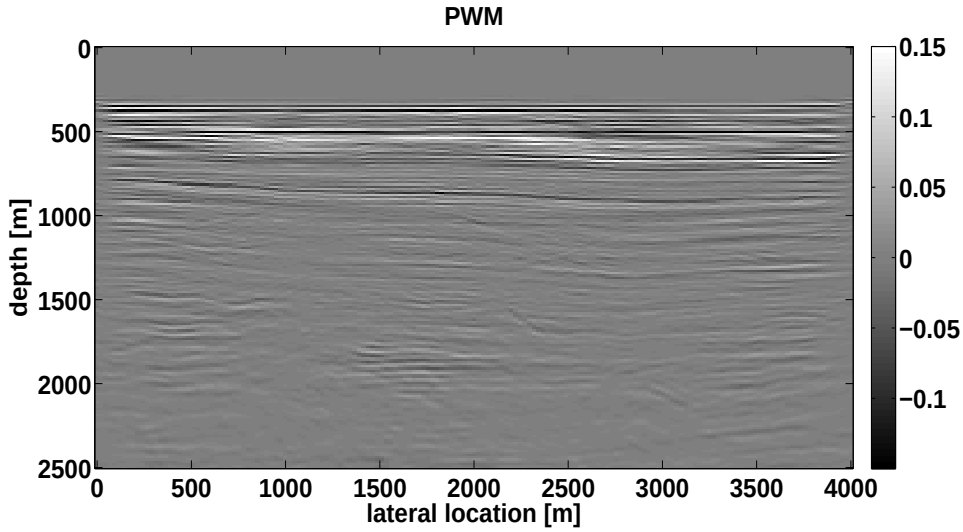

b)

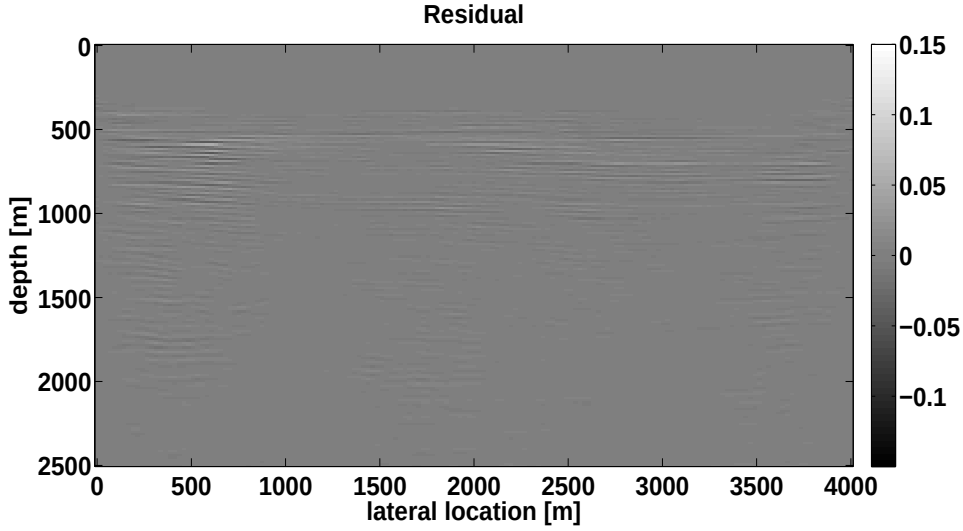

Figure 5.11: *a) The estimated images using primaries-only PWM. b) The residual between the PWM image (figure 5.11a) and the FWM image (figure 5.6).*

6

Beyond VTI

In the previous chapters, we limited ourselves to the special case of VTI media, which is the case when the symmetry axis is vertical. It is a fair assumption for many undisturbed geologic environments, where the layering remained horizontal since deposition. However, when tectonic forces act upon the medium it can deform it in many different ways. The deformation in these complex geologic structures may cause the symmetry axis to be reoriented in a direction other than the vertical axis. Hence, effectively creating a TTI medium that must be considered in imaging. Examples of deformed geologic settings that behave as effective TTI media are folds, shale flanks of salt diapir, and overthrust dipping shales. Effective TTI media can also be caused by a system of parallel dipping fractures [Tsvankin et al., 2010]. Ignoring TTI kinematics can cause mis-positioned structures and blurred images.

In this chapter we will include TTI kinematics in the FWMod scheme. We then incorporate TTI kinematics in FWM. We show the advantage of including internal multiples in imaging TTI media. Finally, we will analyze the effects of perturbations of TTI parameters on the estimated image.

6.1 Full Wavefield Modeling in TTI media

Full Wavefield modeling (FWMod) utilizes two types of operators to model the reflection response of the subsurface. The first is the scattering operator **R**, which dictates the reflection and transmission properties at each point in the subsurface. The second is the propagation operator **W**, which dictates the kinematics associated with a propagating wave at each point in the subsurface. In chapter 2 we extended the **W** operator to include VTI kinematics by using the acoustic anisotropic dispersion relation for VTI media (equation 2.1.15). However, since it was an approximation, it did come with limitations. Namely, the pseudo S-wave and the exponential growth in solution for negative η. Since we are using phase shift operators, we were able to reduce the effects of these limitations in a relatively straightforward manner.

Similar to the VTI case we need to update the dispersion relation to account for TTI kinematics. There are two approaches for introducing TTI kinematics. The first is sticking with an acoustic approximation, where the shear velocity is set to zero along the symmetry axis in the stress-strain relation (as done in chapter 2 for the VTI case). The concept is still the same as VTI, however, the tilt makes the algebra more complex. Zhou et al. [2006] follow this approach and derive pseudo-acoustic titled transversely isotropic wave-equations for their implementation. As in the VTI case there are limitations in implementing the TTI acoustic dispersion equation, namely the pseudo S-wave still exists and numerical instabilities happen for negative values of η. As we have seen in chapter 2, we can attenuate their effects if we use phase shift operators.

The second approach solves the TTI dispersion relation directly without any approximations or assumptions. Zhang et al. [2001] derive a quartic dispersion equation for TTI media, which gives the qP-wave and qSV-wave kinematics for arbitrary amount of anisotropy. Their solution is not an approximation as in the acoustic anisotropic dispersion relation, but rather they solve for k_z analytically. Despite the increase in the parameter space compared to the acoustic version, the analytic solution facilitates elastic inversion for future research. Since it is no longer an approximation, six parameters are needed to describe the wavefield. V_{P0} is the qP-wave velocity along the symmetry axis. V_{S0} is the qS-wave velocity along the symmetry axis. θ is the dip of the symmetry axis with respect to the vertical axis. Finally ϵ, δ, and γ are the Thomsen parameters [Thomsen, 1986]. The quartic dispersion

relation for the vertical wavenumber k_z can be written as:

$$k_z^4 + a_3 k_z^3 + a_2 k_z^2 + a_1 k_z + a_0 = 0, \tag{6.1.1}$$

where

$$a_3 = [f(\epsilon - \delta) sin(4\theta) + 2\epsilon(1-f) sin(2\theta)] k_x / a_4, \tag{6.1.2a}$$

$$a_4 = f - 1 + 2\epsilon(f-1) sin^2(\theta) - \frac{f}{2}(\epsilon - \delta) sin^2(2\theta), \tag{6.1.2b}$$

$$a_2 = \left[b_2 k_x^2 + \left(\frac{\omega}{V_{P0}} \right)^2 (2 + 2\epsilon sin^2(\theta) - f) \right] / a_4, \tag{6.1.2c}$$

$$b_2 = f(\epsilon - \delta) sin^2(2\theta) - 2(1-f)(1+\epsilon) - 2f(\epsilon - \delta) cos^2(2\theta), \tag{6.1.2d}$$

$$a_1 = \left[b_1 k_x^3 - 2\epsilon sin(2\theta) \left(\frac{\omega}{V_{P0}} \right)^2 k_x \right] / a_4, \tag{6.1.2e}$$

$$b_1 = 2\epsilon(1-f) sin(2\theta) - f(\epsilon - \delta) sin(4\theta), \tag{6.1.2f}$$

$$a_0 = b_0 / a_4, \tag{6.1.2g}$$

$$\begin{aligned} b_0 = {} & (2 + 2\epsilon cos^2(\theta) - f) \left(\frac{\omega}{V_{P0}} \right)^2 k_x^2 - \left(\frac{\omega}{V_{P0}} \right)^4 \\ & - \left[(1-f)(1 + 2\epsilon cos^2(\theta)) - \frac{f}{2}(\epsilon - \delta) sin^2(2\theta) \right] k_x^4, \end{aligned} \tag{6.1.2h}$$

and

$$f = 1 - V_{S0}^2/V_{P0}^2. \tag{6.1.2i}$$

Solving equation 6.1.1 analytically is not straightforward, as one must rewrite the quartic equation in terms of two quadratic equations and then solve for them (as done in Zhang et al. [2001]). The four solutions or the four roots of the quartic equation are associated with the upgoing and downgoing qP-wave and the upgoing and downgoing qS-wave. Figure 6.1 shows the dispersion relation pertaining to the downgoing qP-wave at 25Hz, it was generated in a TTI medium with $V_{P0} = 4000m/s$, $V_{S0} = 2000m/s$, $\epsilon = 0.2$, $\delta = 0$, $\gamma = 0$, $\theta = -30^o$. Note that the apex is no longer at $k_z = 0$ but rather shifted due to the non-vertical symmetry axis. Substituting the new dispersion curve in the propagation operator $\mathbf{W}$ incorporates TTI kinematics in FWMod. Figure 6.2 shows a snapshot of the qP-wave propagating in a homogeneous model with $V_{P0} = 2000m/s$, $V_{S0} = 1000m/s$, $\epsilon = 0.2$, $\delta = 0.1$, $\gamma = 0$, and $\theta = 30^o$. The wave propagation is asymmetric due to the TTI kinematics. Also note that the source and receivers are located inside an anisotropic layer, however, no pseudo S-waves are observed since we are no longer using an acoustic approximation. Hence, we do not need apply the remedies described in chapter 2. Note that since we have complete control over the explicit propagation operator and the solutions of the dispersion relation, we can separate the different solutions. In our case, we are mostly interested in the upgoing and downgoing qP-wave. Therefore, we will limit the solutions to the qP-waves only. With the new extrapolation operators that handle TTI media we can update the FWMod equations (equations 2.2.25 and 2.2.26) to handle the TTI kinematics. Note that we have control over the order of scattering being generated in the TTI model, hence, each roundtrip will add an order of scattering in the recorded data.

6.2 Full Wavefield Migration in TTI Media

Assuming a known subsurface velocity and anisotropy model, JMI reduces to FWM since there is no tomography associated. As in the VTI case, we only consider scalar reflectivities, hence, angle-independent reflectivities will be estimated. The imaging will only take into account the kinematics of TTI media. We update the reflectivity gradient (equation 3.3.3) by including the TTI propagation operators $\mathbf{W}$. We also update the linearized perturbation

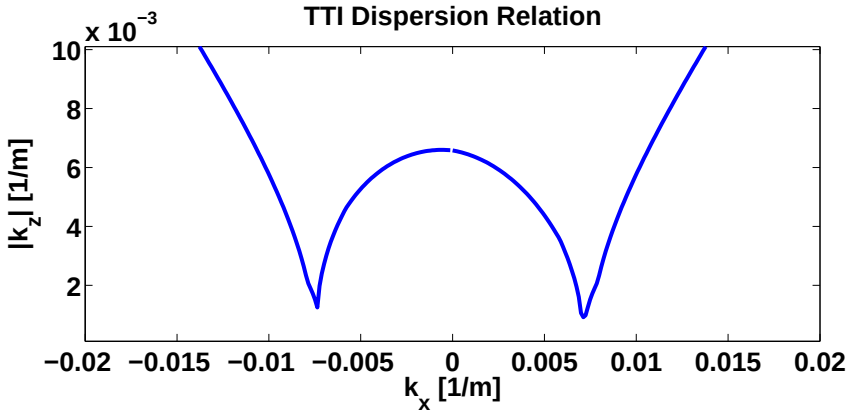

Figure 6.1: *The qP-wave dispersion relation in a homogeneous TTI medium with* $V_{P0} = 4000m/s$, $V_{S0} = 2000m/s$, $\epsilon = 0.2$, $\delta = 0$, $\gamma = 0$, *and* $\theta = -30^o$.

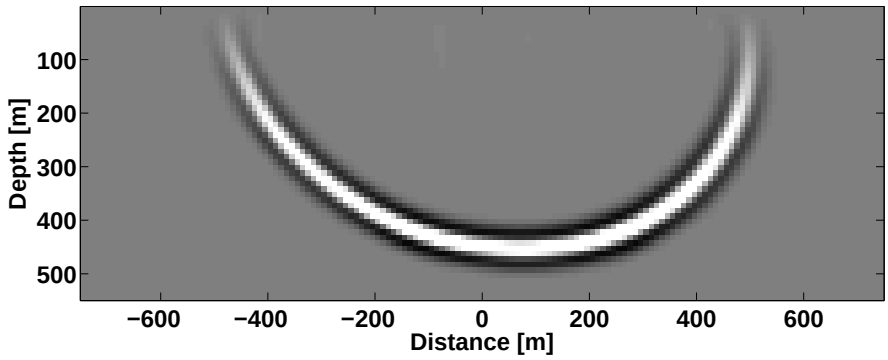

Figure 6.2: *qP-wavefield in a homogeneous TTI medium with* $V_{P0} = 2000m/s$, $V_{S0} = 1000m/s$, $\epsilon = 0.2$, $\delta = 0.1$, $\gamma = 0$, *and* $\theta = 30^o$.

(equation 3.3.4) with the TTI propagation operators to get an appropriate step length α_r.

We test the effectiveness of TTI FWM on the 2007 BP TTI Velocity-Analysis Benchmark model. We consider only a subset of the model containing the anticline, after which we subsample and rescale it due to its large size. Figure 6.3 shows the true reflectivity, true V_{P0}, true δ, true ϵ, and true θ. The shear velocity V_{S0} was set to half of V_{P0} while γ was set to zero. We generated 74 equally spaced shots at the surface and receivers are placed at the surface at $20m$ intervals. We model the data via FWMod while taking into account the TTI kinematics. Figure 6.4a shows the primary arrivals for one shot gather in the middle of the model. Figure 6.4b shows the same shot gather with primaries and internal multiples. Note that internal multiples constitute a significant portion of the recorded data. The first two reflectors have high reflectivity and, hence, create strong internal multiples that reverberate through the record. These internal multiples will obscure the image if not taken into account properly.

Given the anisotropic model we migrate the data following the FWM method [Berkhout, 2014b; Davydenko and Verschuur, 2017]. However, we include the TTI extrapolators for the forward and inverse extrapolation in order to handle TTI kinematics. As in the previous VTI examples we can take advantage of the imaging engine to examine different orders of scattering such as primaries-only or the full wavefield (primaries and internal multiples). The first case we consider is primaries-only imaging, where we limit FWM to primary wavefield imaging (PWM) [Berkhout, 2014b; Davydenko and Verschuur, 2017]. The method will explain the primaries, but will not properly explain the internal multiples. Figure 6.5a shows the image after applying PWM. We notice that extra reflectors appear in the image due to the multiples being explained as primaries. We also note that there is great deal of cross-talk appearing underneath the anticline, which degrades the quality of the image. The second case we consider is FWM where primaries as well as internal multiple are properly taken into account. Hence, FWM is applied to the scattered data without limitations. Figure 6.5b shows the the image after applying FWM. Note that many of the extra reflectors have been suppressed since the associated multiple energy was addressed properly. The reflectors are also of a higher quality since the cross-talk is minimized. We do note that some cross-talk still survives in the FWM image, however, it is highly attenuated compared to the primaries-only image.

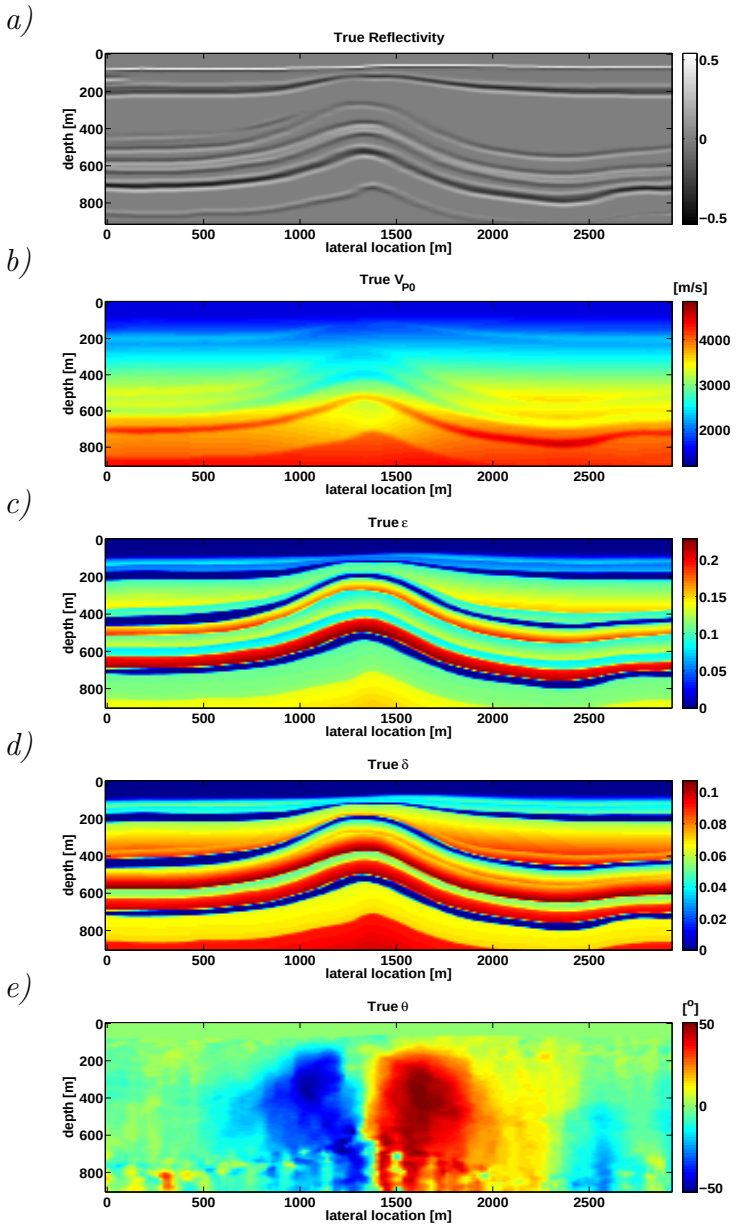

Figure 6.3: *Subset of the 2007 BP TTI Velocity-Analysis Benchmark model: a) the reflectivity, b) the P-wave velocity along the symmetry axis V_{P0} [m/s], c) ϵ, d) δ ,and e) θ [^{o}] values.*

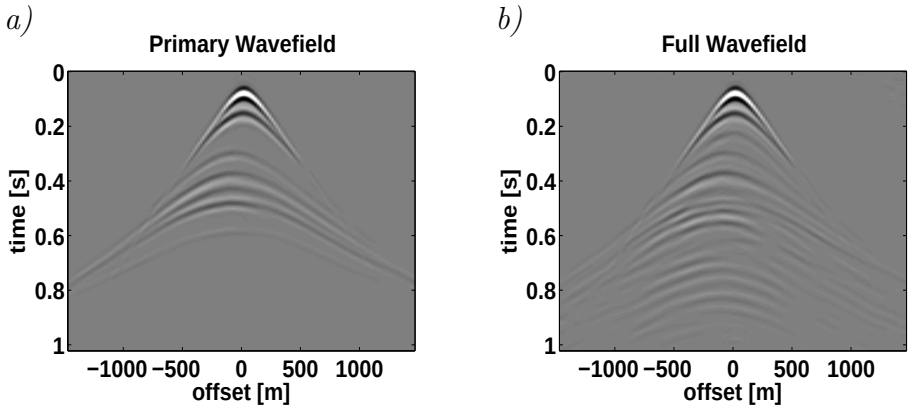

Figure 6.4: *Shot gather in the middle of the BP TTI model. a) The primary reflections only. b) The full wavefield (primaries and internal multiples).*

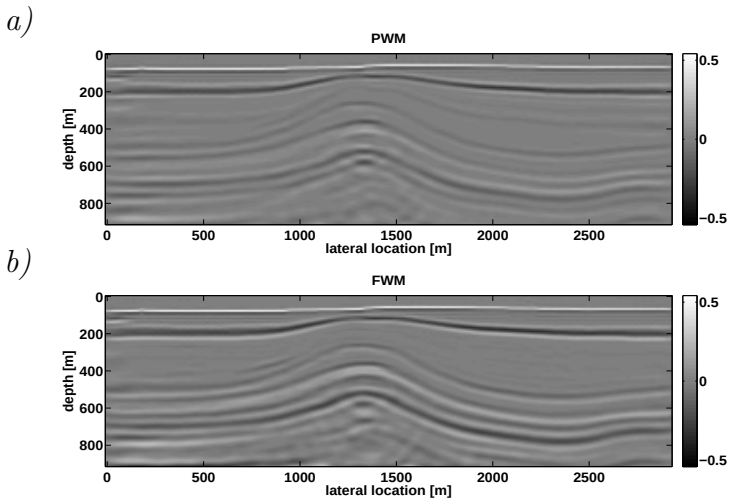

Figure 6.5: *The estimated images for the BP TTI model. a) The estimated image accounting for primaries-only. b) The estimated image accounting for primaries and internal multiples.*

6.3 Sensitivity Analysis in TTI Media

The quality of the image strongly relies on the accuracy of the anisotropic velocity models used. In this section we analyze the influence that the different TTI parameters have on the image. We start by perturbing some of the TTI parameters (V_{P0}, δ, ϵ, and θ) and evaluating the associated FWM image. We perturb the V_{P0} parameter by decreasing its value to be 20% lower than its true values, while keeping the other paramters fixed to their true values. Figure 6.6a shows the resulting image when the perturbed velocity model is used for imaging, while the original data is used. The image is significantly worse, which shows the significant influence of V_{P0} on imaging.

Figure 6.6b shows the effect of perturbing δ, where we set its value to zero. We note that the reflectors are slightly blurred. However, it is not that significant due to the low value of δ in this model (with an average value of approximately 0.05) and the fact that V_{P0} is correct. Next, we analyze the effect of the ϵ parameter on the image. Figure 6.6c shows the estimated image when ϵ is set to zero. We note that a large part of the image is blurred due to the effect of not flattening the reflectors at the far offsets. Hence, the well-known "hockey stick" effect is present and causes imperfect focusing. Finally, we perturb the θ parameter. Figure 6.6d shows the estimated image when θ is set to zero. θ has a significant impact on the position and dip of the reflectors, especially on the flanks of the anticline where its value is maximum. The shape of the anticline is now more gentle compared to the true image.

6.4 Towards TTI Parameter Estimation

In its current implementation JMI estimates the reflectivity, velocity, and even anisotropie models for VTI media. However, when it was first proposed by Berkhout [2012], it was envisioned that the parameterization is constrained to the reflectivity $\mathbf{R}$ and propagation operators $\mathbf{W}$. The advantage of using this type of generalized parametrization is that it avoids defining a certain model that the data should adhere to. If we consider the case of anisotropie kinematics, we assume a certain anisotropic model before starting the inversion (VTI or TTI in our case). The inversion is limited in terms of the anisotropic model, if some parts of the model do not obey this assumed model then there will be errors in inversion. An operator descrip-

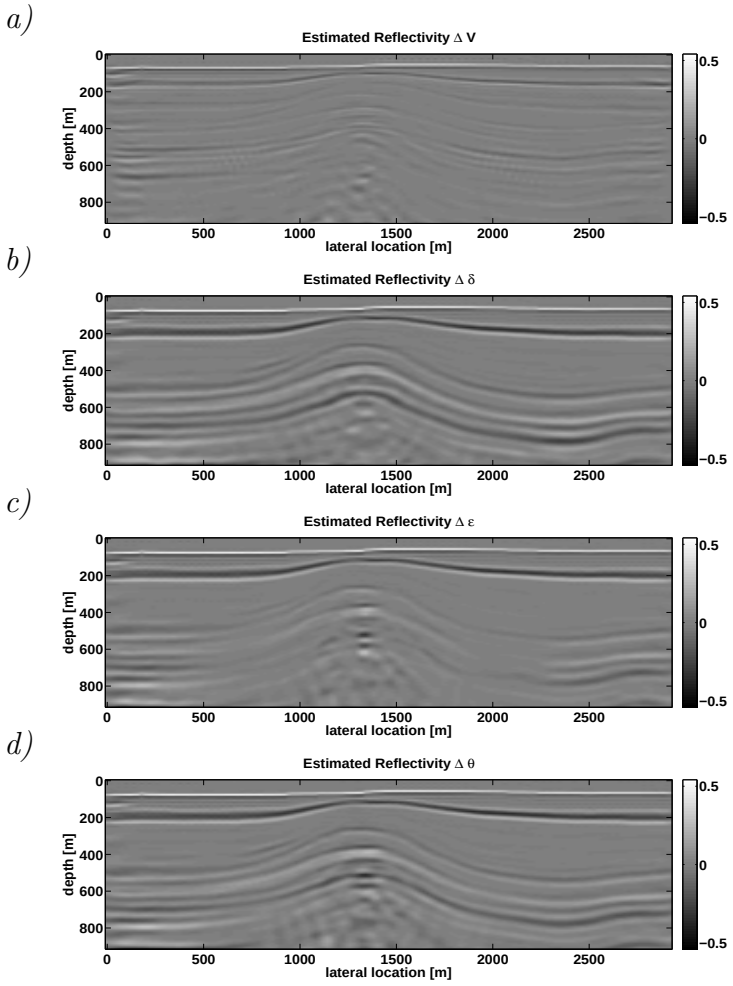

Figure 6.6: *The FWM image after perturbing a) the velocity (V_{P0}), b) δ, c) ϵ, and d) θ.*

tion of the subsurface does not impose any anisotropic models. The data is explained by the operators which increases the flexibility of the method. Another advantage lies in that the trade-off between the different parameters during inversion is no longer an issue. During inversion there is a degree of trade-off happening between the different TI parameters that might cause an oscillation of the solution between the parameters to be inverted. An operator that explains the data will not suffer as much from the trade-off issue during inversion. In this approach the TI parameterization is postponed to the end of inversion when the most accurate operator is estimated.

Coming back to the TTI problem at hand and looking at the dispersion relation we can see that this is not a straightforward linearization problem as in the VTI case. One could add different constraints in order to reduce and stabilize the inversion process. One common constraint is the structural transverse isotropy (STI) constraint, where the θ parameters is obtained by finding the reflectors dip in the image. However, the image used to obtain the dip of the reflectors is computed under an isotropic or a VTI assumption, which could result in erroneous dips in the first place. This can cause mispositioning of reflectors even if the other parameters were correct, as we have seen in figure 6.6d. Using a more advanced constraint such as dip-constrained transverse isotropy (DTI) can mitigate many of the structural issues as shown in Alkhalifah and Sava [2010].

Inverting directly for the propagation operator $\mathbf{W}$, as suggested in Berkhout [2014c], address many of the issues encountered in inversion. The operator $\mathbf{W}$ will implicitly contain information on the anisotropic parameters absorbed in it. However, this approach greatly expands the parameter space, which makes the inversion a highly under-determinate problem. Having prior knowledge of the operator can help steer the update and reduce the number of unknowns in the $\mathbf{W}$ matrix. It is definitely an interesting and fruitful approach that should be investigated in more scrutiny. Hence, this topic is left for further research.

7

Conclusions and Recommendations

When Full Wavefield Migration (FWM) was developed it was clear that it could provide superior images compared to traditional imaging. However, it was soon realized that if the velocity model was inaccurate then the image was of subpar quality. The need to include a tomographic component was evident. Joint Migration Inversion (JMI) combined imaging (typically FWM) with tomography. Although the tomographic component was limited to isotropic velocities it enabled imaging to be more applicable even when the velocity model was unknown. In our never ending strive to include more physics in modeling and inversion, I present a JMI approach that handles anisotropy.

The aim of this thesis was to include anisotropic kinematics to the JMI method. In chapter 1 and in more detail in chapter 2 we analyzed the effect of anisotropie kinematics on seismic reflection data. Furthermore, we saw in chapter 4 the effect of ignoring these anisotropic effects in inversion, where the isotropic velocities appear to be slower or faster (depending on the anisotropy), resulting in a degraded image. Clearly, anisotropy must be taken into account when it is present. In this thesis we consider two of the most commonly encountered anisotropic models namely, Vertical Transpose Isotropy (VTI) and Tilted Transpose Isotropy (TTI). Chapters 2 through 5 consider the VTI case while chapter 6 considers the TTI case. In this chapter

we discuss the main conclusions and explore future recommendations.

7.1 Conclusions

7.1.1 Anisotropic FWMod in VTI media

Before inversion we had to include anisotropie kinematics in our modeling engine (FWMod). We made use of the anisotropic dispersion relation associated with the acoustic wave-equation for VTI media. It enabled us to describe the anisotropic kinematics without having to resort to full elastic modeling. This reduced the number of parameters needed for inversion. It also simplifies the equations and reduced the computational cost involved in modeling and subsequently in inversion. Since it is an approximation, it came with two main limitations: the generation of a pseudo S-wave when the medium is anisotropic and an instability occurring with negative values of η. Attenuating these limitations for a implicit modeling method is not straightforward.

However, utilizing an explicit modeling method, such as FWMod, granted an immense flexibility in alleviating these limitations in a straightforward manner. We were able to distinguish and eliminate the pseudo S-wave directly from the propagation operators. Having explicit control over the propagation operator enabled us to diminish the exponentially increasing solution for negative values of η. With the new VTI extrapolators we are able to model reflections (primaries and multiples) in VTI media. The multiples are modeled iteratively, where each iteration adds an order of scattering (similar to the so-called Bremmer series) based on the reflectivity image. The nonlinearity of the modeling engine is the key in incorporating internal multiples in inversion. Since internal multiples are included, transmission effects are also naturally incorporated in the modeling engine. Although, angle-dependent reflection effects were not included for the implementation used in this thesis, it provides an accurate enough scheme for inversion.

7.1.2 Robustness of Anisotropic JMI

Anisotropic JMI is based on integrating anisotropic velocity estimates with reflectivity estimates, thus, making the process of inversion very robust. In

Chapter 3 we analyzed this robustness in converging to a solution more meticulously. For a layered model we evaluated the cost function for a number of different cases and different solutions. When the reflectivity is fixed the cost function starts oscillating, which increases the chance of getting stuck in a local minimum. However, estimating the best fit reflectivity between each iteration of velocity updates drastically changes the shape of the cost function. The cost function becomes less cyclic. Even when the discrepancy between the true and initial starting models are large the solution converges in an appropriate direction.

Hence, estimating the reflectivity along with the anisotropic velocities facilitates the convergence to a suitable solution. We corroborate this observation with synthetic examples. The most prominent ones are the layered model (example 2 in chapter 4) and the elastic model (example 3 in chapter 4). In these examples the initial velocity models were chosen to be far from the true models. However, anisotropic JMI was able to reconstruct an accurate image, velocity velocity model, and horizontal velocity model.

7.1.3 Multiples

Initially, the main reason to address internal multiples was to reduce the cross-talk appearing in the image. However, we soon realized that if the internal multiples were prominent, they not only create cross-talk in the image, but they also incorrectly influence the velocity update. The lens-shaped model (example 1 in chapter 4) and internal multiple model (example 5 in chapter 4) showed that internal multiples can obscure not only the image but also the velocity update if not taken into account. Since internal multiples were of high amplitudes compared to the primaries, they were picked up by the inversion algorithm as primaries for the primaries-only inversion case. Moreover, internal multiples constitute a significant amount of the energy in the reflection data for certain models. For example, the forward modeling example in chapter 2 shows that a significant part of the reflections in the record are internal multiples.

Addressing internal multiples during inversion will reduce the imprint of the cross-talk in the image as well as introduce extra sensitivity in updating the velocities. Analyzing internal multiples shows that they are more than redundant information. In the cost function analysis in chapter 3 we compared the cost function when multiples are modeled and when they are not

modeled. The trade-off between the parameters is much more constrained when multiples are considered. Internal multiples generally spend more time in the subsurface, therefore, they generally have more of an imprint of the subsurface parameters in them. This in turn helps in uniquely defining the subsurface parameters and subsequently reduce the trade-off. Although multiples will not generally generate wider offset data, they bring in the extra sensitivity in the V_v parameter, which in turn better constrains the V_h estimate.

In the internal multiple model (example 5 in chapter 4) we verify the extra sensitivity that internal multiples bring in. We see that when multiples are in the data and are ignored they can produce erroneous images that prioritize focusing the internal multiples at the wrong location at the expense of defocusing the primaries. We also note that the anisotropic velocities are overestimating due to the interference from the internal multiples. However, when they are properly addressed they produce a focused image that represents the subsurface reflectivities more accurately. Furthermore, it generates suitable corresponding anisotropic velocity models that focus the primaries and the internal multiples. Finally, using the same model we generate only primaries in the observed data and proceeded to invert for the primaries-only. We simulate a case where internal multiples are perfectly eliminated in the recorded data. We note that for the primaries-only inversion results the trade-off between V_v and V_h is more significant compared to the JMI approach where internal multiples are not eliminated and are taken into account properly. In this example the internal multiples reduce the trade-off between the inverted parameters (namely, V_v and V_h).

7.1.4 Synthetic Inversion Results

We test the method on a number of synthetic models. The first five models (examples 1-5 in chapter 4) are simple models that facilitate analyzing a single effect, such as isotropic inversion versus anisotropic inversion, inversion of data generated via FD versus FWMod, and inversion of primaries and internal multiples versus primaries-only inversion. However, the final synthetic model (example 6 in chapter 4) demonstrates the method on a realistic model that resembles a conventional exploration play. The model is the HESS VTI model. Anisotropic JMI estimates the reflectivity and anisotropic velocities in each iteration. We initially only estimate the angle-independent reflectiv-

ities and the vertical velocities. Only after a couple of iterations we include the horizontal velocity in the inversion. This approach stabilized the inversion. The reflectivity estimates are sharp band-limited versions of the true reflectivities. The vertical and horizontal velocities are generally a smooth representation of their true counterparts. The reason behind this is that the modeling method (Anisotropic FWMod) strictly separates these two quantities, where the reflectivity generates the scattering while the anisotropic velocities propagate the wavefields. Hence, the dynamic effects are mapped to the image while the kinematic effects are mapped to the anisotropic velocities. Moreover, the transmission effects and the internal multiples are addressed naturally. Therefore, they do not appear as significant artifacts in the image nor as unusual velocity updates.

7.1.5 Field Data Examples

We test anisotropic JMI on a marine field data set acquired in the North Sea. A well was drilled in the middle of the section and well-logs were acquired. However, the logs were only acquired beyond $1000m$ depth. Hence, the first $1000m$ were relatively unknown. We make use of a smoothed version of the well-logs to build the initial velocity model beyond $1000m$, while the velocities between the water bottom and $1000m$ were set to a constant value of $1700m/s$. We generate the FWM image associated with the initial velocity model. We note that many of the events are not focused and many of the reflectors are discontinuous. Furthermore, the ADCIGs showed curved events indicating that the velocity model is erroneous.

Applying anisotropic JMI we find the best fit anisotropic velocity model and the best fit reflectivity model. We note that the reflectivity is more continuous and the faults at the deep parts of the section are better visible. Analyzing the ADCIGs shows that the majority of the events have been flattened. We also compare the measured shot gathers versus the calculated shot gathers. Many of the reflection events are explained. However, in this domain we can analyze the limitations of the method. Refraction arrivals were ignored since they are not included in the modeling engine (FWMod). Furthermore, the Amplitude Versus Offset (AVO) effects and the converted waves are not explained either. Nevertheless, the majority of the events recorded were explained by the inversion method.

We also run JMI in an isotropic mode with the same set of initial parameters

as the anisotropic inversion. We note that although the resulting image is acceptable, the large offsets and angles are not quite contributing, as indicated by the curved ADCIGs. Although surface-related multiples were eliminated via SRME, internal multiples are still present in the data. We showed that they appear as considerable artifacts in the estimated image if they are not taken into account properly.

7.1.6 TTI Modeling and Imaging

Chapter 6 is dedicated to go beyond a VTI assumption and into a TTI assumption. We started by introducing TTI kinematics in the modeling method. For this implementation we decided to apply the TTI dispersion relation directly without any acoustic approximation. Solving for the quartic TTI dispersion relation is computationally intensive compared to the acoustic VTI dispersion relation. However, it provides us with more flexibility in the future if one were to move beyond acoustic inversion. The TTI extrapolators account for the tilt, which can produce non-symmetric wavefields in homogeneous media.

With the extrapolators, we can extend the method to account for TTI kinematics in FWM. We tested the method on a subset of the 2007 BP TTI velocity-analysis Benchmark model. We can see that taking multiples into account (as done in FWM) yields better results compared to taking primaries-only in TTI media. Finally, we tested the sensitivity of the different anisotropic parameters on the imaging results. We can conclude that the θ parameter in particular has a significant effect on the position of the reflectors in the image. Hence, a VTI assumption is not sufficient for imaging.

7.1.7 Automation

Anisotropic JMI is relatively hands-off compared to more traditional velocity analysis methods. Anisotropic JMI does not require a user to pick the velocities. Hence, avoiding user bias during picking velocities. Furthermore, with the ever increasing amount of seismic data being recorded in each survey the process of manually picking velocities becomes cumbersome. This is exacerbated when the user must not only pick isotropic velocities but also pick anisotropic parameters along with the velocity. After initial setup anisotropic JMI runs automatically without the need for a user to intervene.

7.2 Recommendations for Future Research

7.2.1 Other Arrivals

JMI relies on all types of reflections (primaries and multiples) to explain the subsurface parameters. However, other modes (such as surface waves and diving waves) also travel in the subsurface. These events could provide more information of the subsurface parameters. Diving waves in particular could help in better defining the horizontal velocity since they travel mostly in a horizontal direction. FWI implementations actually make use of the diving wave to update the velocities with great success [Alkhalifah, 2016a]. Including diving waves in inversion, one must update the modeling engine to include diving waves first. Davydenko and Verschuur [2013] and Berkhout [2014b] introduce an omni-directional implementation of FWMod where they include horizontally traveling waves. It is an initial step that incorporates more of the recorded data. However, since diving waves have a significant part traveling in both an up and down sense and in a left and right sense, it was not yet fully resolved how these different propagation directions can communicate with each other, while maintaining conservation of energy.

7.2.2 Angle-dependent R

In our implementation we assume that $\mathbf{R}$ is angle-independent. Hence, we discard the off-diagonal elements of the matrix. The off-diagonal components in the reflectivity operator can be considered as subsurface offsets of the reflectivity and are routinely used for Amplitude Versus Offset (AVO) studies. AVO analysis can shed light on the density, porosity, and even fluid content [Aki and Richards, 1980]. The off-diagonal components will also introduce more physics in the inversion. Hence, the seismic reflection data will be better explained.

For the FWM implementation, Davydenko and Verschuur [2017] show that angle-dependent reflectivities can be estimated by making use of the linear Radon domain. The transformation in the linear Radon domain allows the off-diagonal components of the reflectivity matrix to map into angle gathers, after which they sum over frequencies. Mapping to the linear Radon domain and summing over frequencies facilitates a more compact representation that avoids over-parameterizing the problem.

Extending this towards a JMI application where the velocity model is estimated along with the angle-dependent reflectivity is not straightforward. One can run the risk of over-parameterizing the problem, such that the angle-independent reflectivities leak into the velocity estimates and vice versa. Additional constraints, such as flattening CIGs, are being investigated in order to minimize this trade-off.

7.2.3 Elastic Effects

We base our modeling engine on an anisotropic acoustic approximation of the subsurface, although its validity is questionable when comparing it with real elastic data. Full elastic modeling requires much more parameters to describe it and subsequently more parameters to invert for. Hence, an accurate starting model is essential for inversion in order to avoid the null space. Starting with an acoustic approximation can help identify and estimate the essential parameters for subsequent inversion. Moreover, three or sometimes four component data is required for elastic inversion. Frequently, single component pressure or vertical displacement data is all that is recorded.

Nevertheless, elastic effects can be significant, inverting the layered elastic anisotropic model (example 4 in chapter 4) was challenging because the elastic effects were significant in the recorded data. However, our VTI implementation is based on an acoustic assumption. Therefore, when we blindly inverted the raw data we did not get satisfactory results. However, by preprocessing the raw data we were able to mitigate the elastic effects and rerun the inversion with better final results. Although, preprocessing helped in mitigating the elastic effects the optimal solution is to include the elastic effects in modeling and inversion. The ultimate goal is to use all the recorded data to describe the subsurface. In this way, one must include PS reflectivity operators and S-wave propagation operators in the FWMod scheme, then attempt to invert for them in a JMI-type approach. The converted waves can contribute towards an update for the image and velocities. Note that when converted waves are included in FWMod, the angle-independent reflection approach does not provide a reasonable approximation, since the converted wave reflectivity has a strong angle-dependent behavior.

7.2.4 Anisotropy Parametrization

As in all anisotropic inversion techniques the choice of parametrization is critical in obtaining an accurate solution. Also the trade-off between the different parameters must be taken into account. Although, we did not meticulously test the different parameterizations we were fortunate enough to rely on the work of others to better understand the different effects of parameterization. We use a V_v, V_h, and δ parametrization. With δ being excluded from inversion due to the intrinsic ambiguity between it and depth, it's estimates are obtained from other sources of information. Hence, we focus the kinematic part of the inversion to be between V_v and V_h. For our implementation we believe that this choice of parameters strives to minimize the trade-off between the parameters as much as possible. One can chose a different parameterization that consists of different combinations of velocities, Thomson parameters, and η. Translating the new parameterization is relatively straightforward. However, one must re-derive the gradients and apply some scaling in the case of the unitless parameters (Thomsen parameters and η) parameterizations.

7.2.5 Extension towards 3D

The development of the method is limited to the 2D case. If one where to image prominent 3D objects in the subsurface, inaccuracies would build up in the image due to out of plane reflections. Furthermore, a 3D application would increase the amount of information and accuracy of the image and the model.

Conceptually, the 3D extension of the 2D theory should follow a path similar to the JMI's isotropic 3D extension presented by Marhfoul and Verschuur [2016]. In practice the challenge lies in addressing the sparse and irregular sampling that is usually accompanied with 3D surveys. However, surface-related multiples can be utilized as secondary sources in order to fill up the illumination gaps as was shown by Kumar et al. [2014] and Davydenko and Verschuur [2017].

7.2.6 Propagation Operator Estimation

I leave the most encouraging recommendation for last. Currently, we linearize the propagation operator $\mathbf{W}$ in terms of a vertical velocity V_v and a horizontal velocity V_h. In doing so we greatly reduce the number of parameters being estimated in each iteration. However, we limit ourselves in terms of an anisotropic model and we are prone to parameter trade-off during inversion.

Estimating directly the propagation operator $\mathbf{W}$, allows the data, albeit complex it may be, to be explained directly by the operator. It avoids defining a certain propagation model that the data should obey. In most anisotropic inversion methods the model needs to be set before inversion. If parts of the model do not obey this assumed model then there will be errors in inversion. An operator description of the subsurface does not impose any anisotropic models (VTI or TTI). The data is explained by the operators, with fully flexible phase functions, which increases the applicability of the method to a wider range of anisotropic models. The other advantage lies in that the trade-off between the anisotropic parameters in inversion is no longer an issue. The inverted operator will be estimated such that it explains the reflection data. In this approach parameterization in terms of more traditional anisotropic parameters is postponed to the end of inversion when the most accurate operator is estimated.

Although inverting directly for the propagation operator $\mathbf{W}$ addresses many of the issues encountered in inversion. This approach greatly expands the parameter space, which makes the inversion a highly under-determinate problem. However, having prior knowledge of the operator via constraints can help steer the update and reduce the number of unknowns in the $\mathbf{W}$ operators.

A

Derivation of the Gradients

A.1 Vertical Velocity Gradient

We linearize the propagation operator (equations 3.3.11 and 3.3.12) with respect to the contrast parameter β_v. Each element can be written in the wavenumber frequency domain as:

$$\frac{\partial}{\partial \beta_v}\left[\tilde{W}(k_x; z_{m+1}, z_{m+1}; \omega)\right]_{\beta_v=0} = -j\Delta z\left(e^{-jk_z\Delta z}e^{-jk_x x_i}\right)\frac{\partial}{\partial \beta_v}\left[k_z\right]_{\beta_v=0}. \tag{A.1.1}$$

where,

$$\frac{\partial}{\partial \beta_v}\left[k_z\right]_{\beta_v=0} = \frac{1}{2}\frac{1}{k_z}\frac{\partial}{\partial \beta_v}\left[\frac{\omega^2}{V_v^2} - \frac{\omega^2(1+2\delta)k_x^2}{\omega^2 - V_h^2k_x^2 + V_v^2(1+2\delta)k_x^2}\right]_{\beta_v=0} \tag{A.1.2}$$

Note that we are using the acoustic anisotropic dispersion relation to express k_z (equation 2.1.15). Taking the first expression and substituting the contrast parameter with velocities (equation 3.3.8) we arrive at,

$$\frac{\partial}{\partial \beta_v}\left[\frac{\omega^2}{V_v^2}\right]_{\beta_v=0} = \omega^2\frac{\partial}{\partial \beta_v}\left[\frac{1-\beta_v}{V0_v^2}\right]_{\beta_v=0} = \frac{-\omega^2}{V0_v^2}. \tag{A.1.3}$$

The second expression can be calculated by applying the quotient rule

$$\frac{f\left[\frac{\partial g}{\partial \beta_v}\right] - g\left[\frac{\partial f}{\partial \beta_v}\right]}{g^2}, \tag{A.1.4}$$

where

$$f = -\omega^2(1+2\delta)k_x^2, \tag{A.1.5a}$$

$$\begin{aligned}\left[\frac{\partial f}{\partial \beta_v}\right]_{\beta_v=0} &= \left[\frac{\partial\left(-\omega^2(1+2\delta)k_x^2\right)}{\partial \beta_v}\right]_{\beta_v=0} \\ &= 0,\end{aligned} \tag{A.1.5b}$$

$$g = \omega^2 - V_h^2 k_x^2 + V_v^2(1+2\delta)k_x^2, \tag{A.1.5c}$$

$$\begin{aligned}\left[\frac{\partial g}{\partial \beta_v}\right]_{\beta_v=0} &= \left[\frac{\partial\left(\omega^2 - V_h^2 k_x^2 + V_v^2(1+2\delta)k_x^2\right)}{\partial \beta_v}\right]_{\beta_v=0} \\ &= 0 - 0 + (1+2\delta)k_x^2 \frac{\partial}{\partial \beta_v}\left[V_v^2\right]_{\beta_v=0} \\ &= V0_v^2(1+2\delta)k_x^2 \frac{\partial}{\partial \beta_v}\left[\frac{1}{1-\beta_v}\right]_{\beta_v=0} \\ &= V0_v^2(1+2\delta)k_x^2.\end{aligned} \tag{A.1.5d}$$

Hence,

$$\frac{\partial}{\partial \beta_v}\left[\frac{-\omega^2(1+2\delta)k_x^2}{\omega^2 - V_h^2 k_x^2 + V_v^2(1+2\delta)k_x^2}\right]_{\beta_v=0} = \frac{\omega^2 V0_v^2(1+2\delta)^2 k_x^4}{\left(\omega^2 - V_h^2 k_x^2 + V0_v^2(1+2\delta)k_x^2\right)^2}. \tag{A.1.6}$$

Finally, we can write the linearization of equation A.1.1 as

$$\frac{\partial}{\partial \beta_v}\left[\tilde{W}\right]_{\beta_v=0} = \frac{-j\Delta z}{2k_z}\left(e^{-jk_z\Delta z}e^{-jk_x x_i}\right)\left(\frac{-\omega^2}{V0_v^2} + \frac{\omega^2 V0_v^2(1+2\delta)^2 k_x^4}{\left(\omega^2 - V_h^2 k_x^2 + V0_v^2(1+2\delta)k_x^2\right)^2}\right). \tag{A.1.7}$$

A.2 Horizontal Velocity Gradient

We also linearize the propagation operator (equations 3.3.25 and 3.3.26) with respect to β_h. Each element can be written in the wavenumber frequency domain as:

$$\frac{\partial}{\partial \beta_h}\left[\tilde{W}(k_x; z_{m+1}, z_{m+1}; \omega)\right]_{\beta_h=0} = -j\Delta z\left(e^{-jk_z\Delta z}e^{-jk_x x_i}\right)\frac{\partial}{\partial \beta_h}\left[k_z\right]_{\beta_h=0}, \tag{A.2.8}$$

where,

$$\frac{\partial}{\partial \beta_h}\left[k_z\right]_{\beta_h=0} = \frac{1}{2}\frac{1}{k_z}\frac{\partial}{\partial \beta_h}\left[\frac{\omega^2}{V_v^2} - \frac{\omega^2(1+2\delta)k_x^2}{\omega^2 - V_h^2k_x^2 + V_v^2(1+2\delta)k_x^2}\right]_{\beta_h=0}. \tag{A.2.9}$$

Note that, as in the previous case, we are using the acoustic anisotropic dispersion relation to express k_z (equation 2.1.15). Taking the first expression we find that,

$$\frac{\partial}{\partial \beta_h}\left[\frac{\omega^2}{V_v^2}\right]_{\beta_h=0} = 0. \tag{A.2.10}$$

The second expression can be calculated by applying the quotient rule (equation A.1.4), where

$$f = -\omega^2(1+2\delta)k_x^2, \tag{A.2.11a}$$

$$\begin{aligned}\left[\frac{\partial f}{\partial \beta_h}\right]_{\beta_h=0} &= \left[\frac{\partial\left(-\omega^2(1+2\delta)k_x^2\right)}{\partial \beta_h}\right]_{\beta_h=0} \\ &= 0,\end{aligned} \tag{A.2.11b}$$

$$g = \omega^2 - V_h^2k_x^2 + V_v^2(1+2\delta)k_x^2, \tag{A.2.11c}$$

$$\begin{aligned}\left[\frac{\partial g}{\partial \beta_h}\right]_{\beta_h=0} &= \left[\frac{\partial\left(\omega^2 - V_h^2 k_x^2 + V_v^2(1+2\delta)k_x^2\right)}{\partial \beta_h}\right]_{\beta_h=0} \\ &= 0 - k_x^2 \frac{\partial}{\partial \beta_h}\left[V_h^2\right]_{\beta_h=0} + 0 \\ &= -V0_h^2 k_x^2 \frac{\partial}{\partial \beta_h}\left[\frac{1}{1-\beta_h}\right]_{\beta_h=0} \\ &= -V0_h^2 k_x^2.\end{aligned} \tag{A.2.11d}$$

Hence,

$$\frac{\partial}{\partial \beta_h}\left[\frac{-\omega^2(1+2\delta)k_x^2}{\omega^2 - V_h^2 k_x^2 + V_v^2(1+2\delta)k_x^2}\right]_{\beta_h=0} = \frac{-\omega^2 V0_h^2(1+2\delta)k_x^4}{\left(\omega^2 - V0_h^2 k_x^2 + V_v^2(1+2\delta)k_x^2\right)^2}. \tag{A.2.12}$$

Finally, we can write the linearization of equation A.2.8 as

$$\frac{\partial}{\partial \beta_h}\left[\tilde{W}\right]_{\beta_h=0} = \frac{-j\Delta z}{2k_z}\left(e^{-jk_z\Delta z}e^{-jk_x x_i}\right)\left(\frac{-\omega^2 V0_h^2(1+2\delta)k_x^4}{\left(\omega^2 - V0_h^2 k_x^2 + V_v^2(1+2\delta)k_x^2\right)^2}\right). \tag{A.2.13}$$

Bibliography

Aki, K., and Richards, P. G., 1980, Quantative seismology: W. H. Freeman and Co.

Al-Chalabi, M., 2014, Principles of seismic velocities and time-to-depth conversion: EAGE Publications BV.

Al-Yahya, K. M., 1989, Velocity analysis by iterative profile migraton: Geophysics, **54**, no. 6, 718–729.

Aldawood, A., Hoteit, I., Zuberi, M., Turkiyyah, G., and Alkhalifah, T., 2015, The possibilities of least-squares migration of internally scattered seismic energy: Geophysics, **80**, no. 4, S93–S101.

Alkhalifah, T., and Plessix, R. É., 2014, A recipe for practical full-waveform inversion in anisotropic media: An analytical parameter resolution study: Geophysics, **79**, no. 3, R91–R101.

Alkhalifah, T., and Sava, P., 2010, A transversely isotropic medium with a tilted symmetry axis normal to the reflector: Geophysics, **75**, no. 3, A19–A24.

Alkhalifah, T., and Tsvankin, I., 1995, Velocity analysis for transversely isotropic media: Geophysics, **60**, no. 5, 1550–1566.

Alkhalifah, T., and Wu, Z., 2016, The natural combination of full and image-based waveform inversion: Geophysical Prospecting, **64**, no. 1, 19–30.

Alkhalifah, T., 1997, Seismic data processing in vertically inhomogeneous TI media: Geophysics, **62**, no. 2, 662–675.

Alkhalifah, T., 1998, Acoustic approximations for processing in transversely isotropic media: Geophysics, **63**, no. 2, 623–631.

Alkhalifah, T., 2000, An acoustic wave equation for anisotropic media: Geophysics, **65**, no. 4, 1239–1250.

Alkhalifah, T., 2014, Full waveform inversion in an anisotropic world: EAGE Publications BV.

Alkhalifah, T., 2016a, Research note: Insights into the data dependency on anisotropy: An inversion prospective: Geophysical Prospecting, **64**, no. 2, 505–513.

——— 2016b, Research note: The sensitivity of surface seismic Pwave data in transversely isotropic media to reflector depth: Geophysical Prospecting.

Alshuhail, A., and Verschuur, D. J., 2015, Robust anisotropy estimation using joint migration inversion: 85th Ann. Internat. Mtg., Soc. Expl. Geophys., Expanded abstracts, 472–477.

Alshuhail, A. A., 2006, Fracture-porosity inversion from P-wave AVOA data along 2D seismic lines: An example from the Austin Chalk of southeast Texas: Geophysics, **72**, no. 1, B1–B2.

Anderson, J. E., Tan, L., and Wang, D., 2012, Time-reversal checkpointing methods for RTM and FWI: Geophysics, **77**, no. 4, S93–S103.

Backus, G. E., 1962, Long-wave elastic anisotropy produced by horizontal layering: Journal of Geophysical Research, **67**, no. 11, 4427–4440.

Bagaini, C., 2006, Overview of simultaneous vibroseis acquisition methods: 66th Ann. Internat. Mtg., Soc. Expl. Geophys., Expanded abstracts, 70–74.

Bale, R. A., 2007, Phase-shift migration and the anisotropic acoustic wave equation: 66th Ann. Internat. Mtg., Eur. Ass. of Geosc. and Eng., Expanded abstracts, C021.

Banik, N. C., 1984, Velocity anisotropy of shales and depth estimation in the North Sea basin: Geophysics, **49**, no. 9, 1411–1419.

Baysal, E., Kosloff, D. D., and Sherwood, J. W. C., 1983, Reverse time migration: Geophysics, **48**, no. 11, 1514–1524.

Berkhout, A. J., and Verschuur, D. J., 1999, Removal of internal multiples: 69th Ann. Internat. Mtg., Soc. Expl. Geophys., Expanded abstracts, 1334–1337.

Berkhout, A. J., and Verschuur, D. J., 2000, Internal multiple removal - boundary-related and layer-related approach: 62nd Ann. Internat. Mtg., Eur. Ass. of Geophys. and Eng., Expanded abstracts, L–56.

Berkhout, A. J., and Verschuur, D. J., 2016, Enriched seismic imaging by using multiple scattering: The Leading Edge, **35**, no. 2, 128–133.

Berkhout, A. J., Verschuur, D. J., and Staal, X. R., 2015, Integration of velocity estimation and nonlinear migration: 85th Ann. Internat. Mtg., Soc. Expl. Geophys., Expanded abstracts, 5233–5237.

Berkhout, A. J., 1980, Seismic migration, imaging of acoustic energy by wave field extrapolation, vol. 14a: theoretical aspects: Elsevier; second edition in 1982 and third edition in 1985.

Berkhout, A. J., 1997, Pushing the limits of seismic imaging, part II: integration of prestack migration, velocity estimation and AVO analysis: Geophysics, **62**, no. 3, 954–969.

Berkhout, A. J., 2012, Combining full wavefield migration and full waveform inversion, a glance into the future of seismic processing: Geophysics, **77**, no. 4, S43–S50.

Berkhout, A. J., 2014a, Review Paper: An outlook on the future of seismic imaging, Part I: forward and reverse modelling: Geophys. Prosp., **62**, no. 5, 911–930.

——— 2014b, Review Paper: An outlook on the future of seismic imaging, Part II: Full-wavefield migration: Geophys. Prosp., **62**, no. 5, 931–949.

——— 2014c, Review Paper: An outlook on the future of seismic imaging, Part III: Joint Migration Inversion: Geophys. Prosp., **62**, no. 5, 950–971.

Biondi, B., and Almomini, A., 2014, Simultaneous inversion of full data bandwidth by tomographic full-waveform inversion: Geophysics, **79**, no. 3, WA129–WA140.

Biondi, B., and Shan, G., 2002, Prestack imaging of overturned reflections by reverse time migration: 72nd Ann. Internat. Mtg., Soc. Expl. Geophys., Expanded abstracts, 1284–1287.

Biondi, B., 2006, 3D seismic imaging: Society of Exploration Geophysicists.

Bleistein, N., 1984, Mathematical methods for wave phenomena: Academic Press Inc.

Bleistein, N., 1987, On the imaging of reflectors in the Earth: Geophysics, **52**, 931–942.

Bremmer, H., 1951, The WKB approximation as the first term of a geometric-optical series: Communications on Pure and Applied Mathematics, **4**, no. 1, 105–115.

Bunks, C., Saleck, S. M., Zaleski, S., and Chavent, G., 1995, Multiscale seismic waveform inversion: Geophysics, **60**, no. 5, 1457–1473.

Byun, B. S., Corrigan, D., and Gaiser, J. E., 1989, Anisotropic velocity analysis for lithology discrimination: Geophysics, **54**, no. 12, 1564–1574.

Cheng, X., Jiao, K., Sun, D., and Vigh, D., 2014, Anisotropic parameter estimation with full-waveform inversion of surface seismic data: 84th Ann. Internat. Mtg., Soc. Expl. Geophys., Expanded abstracts, 1072–1076.

Claerbout, J. F., 1971, Toward a unified theory of reflector mapping: Geophysics, **36**, no. 3, 467–481.

Claerbout, J. F., 1985, Imaging the Earth's interior: Blackwell Scientific Publications.

Coates, R. T., and Weglein, A. B., 1996, Internal multiple attenuation using inverse scattering: Results from prestack 1 and 2-D acoustic and elastic synthetics: 66th Ann. Internat. Mtg., Soc. Expl. Geophys., Expanded abstracts, 1522–1525.

Davydenko, M., and Verschuur, D. J., 2013, Full wavefield migration, using internal multiples for undershooting: 83th Ann. Internat. Mtg., Soc. Expl. Geophys., Expanded abstracts, 3741–3745.

Davydenko, M., and Verschuur, D. J., 2014, Omnidirectional extension of full wavefield migration: 78th Ann. Internat. Mtg., Eur. Ass. of Geosc. and Eng., Expanded abstracts, TuG10306.

Davydenko, M., and Verschuur, D. J., 2017, Full-wavefield migration: using surface and internal multiples in imaging: Geophys. Prosp., **65**, no. 1, 7–21.

de Bruin, C. G. M., Wapenaar, C. P. A., and Berkhout, A. J., 1990, Angle-dependent reflectivity by means of prestack migration: Geophysics, **55**, no. 9, 1223–1234.

de Hoop, M. V., Rousseau, J. H. L., and Wu, R., 2000, Generalization of the phase-screen approximation for the scattering of acoustic waves: Wave Motion, **31**, no. 1, 43–70.

Dix, C. H., 1955, Seismic velocities from surface measurements: Geophysics, **20**, no. 1, 68–86.

Dobrin, M. B., and Savit, C. H., 1988, Introduction to geophysical prospecting: McGraw Hill Book Co.

Duveneck, E., Milcik, P., Bakker, P. M., and Perkins, C., 2008, Acoustic VTI wave equations and their application for anisotropic reverse-time migration: 78th Ann. Internat. Mtg., Soc. Expl. Geophys., Expanded abstracts, 2186–2190.

Fei, T. W., and Liner, C. L., 2008, Hybrid fourier finite-difference 3D depth migration for anisotropic media: Geophysics, **73**, no. 2, S27–S33.

Gardner, G. H. F., Gardner, L. W., and Gregory, A. R., 1974, Formation velocity and density-the diagnostic basics for stratigraphic traps: Geophysics, **39**, no. 6, 770–780.

Gazdag, J., 1978, Wave equation migration with the phase-shift method: Geophysics, **43**, no. 7, 1342–1351.

Gerchka, V., 2009, Applications of seismic anisotropy in the oil and gas industry: EAGE Publications BV.

Gholami, Y., Brossier, R., Operto, S., Prieux, V., Ribodetti, A., and Virieux, J., 2013a, Which parameterization is suitable for acoustic vertical transverse isotropic full waveform inversion? Part 2: Synthetic and real data case studies from Valhall: Geophysics, **78**, no. 2, R107–R124.

——— 2013b, Which parameterization is suitable for acoustic vertical transverse isotropic full waveform inversion? Part 1: Sensitivity and trade-off analysis: Geophysics, **78**, no. 2, R81–R105.

Gray, S. H., Etgen, J., Dellinger, J., and Whitmore, D., 2001, Seismic migration problems and solutions: Geophysics, **66**, no. 5, 1622–1640.

Grechka, V., Zhang, L., and Rector, J. W., 2004, Shear waves in acoustic anisotropic media: Geophysics, **69**, no. 2, 576–582.

Hammad, H. I., and Verschuur, D. J., 2016, Joint migration inversion for laterally varying media: 78th Ann. Internat. Mtg., Eur. Ass. of Geosc. and Eng., Expanded abstracts, TuSRS214.

Han, B., Galikeev, T., Grechka, V., Rousseau, J. L., and Tsvankin, I., 2000, A synthetic example of anisotropic P-wave processing for a model from the Gulf of Mexico: Anisotropy 2000: Fractures, converted waves and case studies: Proceedings of the 9th International Workshop on Seismic Anisotropy (9IWSA), Soc. Expl. Geophys.

Igel, H., Mora, P., and Riollet, B., 1995, Anisotropic wave propagation through finite-difference grids: Geophysics, **60**, no. 4, 1203–1216.

Jiang, Z., Sheng, J., Yu, J., and Schuster, G. T., 2007, Migration methods for imaging different-order multiples: Geophys. Prosp., **55**, no. 1, 1–19.

Jones, I. J., 2010, An introduction to: Velocity model building: Eage Publications BV.

Juhlin, C., 1995, Finite-difference elastic wave propagation in 2D heterogeneous transversely isotropic media: Geophysical Prospecting, **43**, no. 6, 843–858.

Kabir, M. M. N., and Verschuur, D. J., 1995, Restoration of missing offsets by parabolic radon transform: Geophys. Prosp., **43**, no. 3, 347–368.

Kabir, M. M. N., and Verschuur, D. J., 1996, Macro model estimation using primary and multiple reflections: DELPHI Volume VII, Chapter 7, pages 7–1 – 7–32.

Kamath, N., and Tsvankin, I., 2016, Elastic full-waveform inversion for VTI media: Methodology and sensitivity analysis: Geophysics, **81**, no. 2, C53–C68.

Keys, R. G., and Foster, D., 1994, Comparison of seismic inversion methods on a single real data set: Post-convention workshop 6: 64th Ann. Internat. Mtg., Soc. Expl. Geophys., Expanded abstracts.

Kumar, A., Blacquière, G., and Verschuur, D. J., 2014, 3-D acquisition geometry analysis: incorporating information from multiples: 84th Ann. Internat. Mtg., Soc. Expl. Geophys., Expanded abstracts, 30–35.

Lee, H. Y., Koo, J. M., Min, D. J., Kwon, B. D., and Yoo, H. S., 2010, Frequency-domain elastic full waveform inversion for VTI media: Geophys. J. Int., **183**, no. 2, 884–904.

Levin, F., 1979, Seismic velocities in transversely isotropic media: Geophysics, **44**, no. 5, 918–936.

Liner, C., and Fei, T. W., 2006, Layer-induced seismic anisotropy from full-wave sonic logs: Theory, application, and validation: Geophysics, **71**, no. 6, D183–D190.

Lopez, G. A., and Verschuur, D. J., 2015, Closed-loop surface-related multiple elimination and its application to simultaneous data reconstruction: Geophysics, **80**, no. 6, V189–V199.

Lu, S., Valenciano, A. A., Cheminigui, N., and Lecerf, D. B., 2015, Separated Wavefield Imaging of Ocean Bottom Seismic (OBS) Data: 77th Ann. Internat. Mtg., Eur. Ass. of Geosc. and Eng., Expanded abstracts, WeN10608.

Lynn, W., Gonzalez, A., and MacKay, S., 1991, Where are the fault-plane reflections?: 61st Ann. Internat. Mtg., Soc. Expl. Geophys., Expanded abstracts, 1151–1154.

Marhfoul, B. E., and Verschuur, D. J., 2016, High-resolution, integrated 3D joint migration inversion of surface and VSP data: 86th Ann. Internat. Mtg., Soc. Expl. Geophys., Expanded abstracts, 672–676.

Matson, K. H., and Weglein, A. B., 1996, Removal of elastic interface multiples from land and ocean bottom data using inverse scattering: 66th Ann. Internat. Mtg., Soc. Expl. Geophys., Expanded abstracts, 1526–1529.

McMechan, G. A., 1983, Migration by extrapolation of time-dependent boundary values: Geophys. Prosp., **31**, no. 3, 413–420.

Menke, W., 2012, Geophysical data analysis: Discrete inverse theory:, volume 45 Academic press.

Michell, S., Shoshitaishvili, E., Chergotis, D., Sharp, J., and Etgen, J., 2006, Wide azimuth streamer imaging of Mad Dog; have we solved the subsalt imaging problem?: 76th Ann. Internat. Mtg., Soc. Expl. Geophys., Expanded abstracts, 2905–2909.

Nemeth, T., Wu, C., and Schuster, G., 1999, Least-squares migration of incomplete reflection data: Geophysics, **64**, no. 1, 208–221.

Nur, A., and Simmons, G., 1969, Stress-induced velocity anisotropy in rock: An experimental study: Journal of Geophysical Research, **74**, no. 27, 6667–6674.

Plessix, R. É., and Cao, Q., 2010, A parametrization study for surface seismic full waveform inversion in an acoustic vertical transversely isotropic medium: Geophys. J. Int., **185**, no. 1, 539–556.

Plessix, R. É., and Mulder, W. A., 2004, Frequency-domain finite-difference amplitude-preserving migration: Geophys. J. Int., **157**, no. 3, 975–987.

Pratt, R. G., 1999, Seismic waveform inversion in the frequency domain, part 1: Theory and verification in a physical scale model: Geophysics, **64**, no. 3, 888–901.

Prieux, V., Brossier, R., Gholami, Y., Operto, S., Virieux, J., Barkved, O. I., and Kommedal, J. H., 2011, On the footprint of anisotropy on isotropic full waveform inversion: The Valhall case study: Geophys. J. Int., **187**, no. 3, 1495–1515.

Robein, E., 2003, Velocities, time-imaging and depth imaging: Principles and methods: EAGE Publications BV.

Robertsson, J. O., Blanch, J. O., and Symes, W. W., 1994, Viscoelastic finite-difference modeling: Geophysics, **59**, no. 9, 1444–1456.

Robinson, E. A., 1983, Migration of geophysical data: Springer.

Rüger, A., 2002, Reflection coefficients and azimuthal AVO analysis in anisotropic media: Society of Exploration Geophysicists.

Sarkar, D., Bakulin, A., and Kranz, R. L., 2003, Anisotropic inversion of seismic data for stressed media: Theory and a physical modeling study on Berea Sandstone: Geophysics, **68**, no. 2, 690–704.

Sava, P., and Biondi, B., 2004a, Wave-equation migration velocity analysis-I: Theory: Geophys. Prosp., **52**, no. 6, 593–606.

——— 2004b, Wave-equation migration velocity analysis- II: Subsalt imaging example: Geophys. Prosp., **52**, no. 6, 607–623.

Sava, P., and Fomel, S., 2003, Angle-domain common-image gathers by wavefield continuation methods: Geophysics, **68**, no. 3, 1065–1074.

Schneider, W. A., 1978, Integral formulation for migration in two and three dimensions: Geophysics, **43**, no. 1, 49–76.

Schoenberg, M., and Sayers, C. M., 1995, Seismic anisotropy of fractured rock: Geophysics, **60**, no. 1, 204–211.

Shan, G., and Biondi, B., 2004, Imaging overturned waves by plane-wave migration in tilted coordinates: 74th Ann. Internat. Mtg., Soc. Expl. Geophys., Expanded abstracts, 969–972.

Staal, X. R., and Verschuur, D. J., 2012, Velocity estimation using internal multiples: 82nd Ann. Internat. Mtg., Soc. Expl. Geophys., Expanded abstracts, 1–5.

Staal, X. R., and Verschuur, D. J., 2013, Joint migration inversion, imaging including all multiples with automatic velocity update: 75th Ann. Internat. Mtg., Eur. Ass. of Geosc. and Eng., Expanded abstracts, Tu0216.

Staal, X. R., Verschuur, D. J., and Berkhout, A. J., 2014, Robust velocity estimation by joint migration inversion: 76th Ann. Internat. Mtg., Eur. Ass. of Geosc. and Eng., Expanded abstracts, WeG10307.

Staal, X. R., 2015, Combined imaging and velocity estimation by Joint Migration Inversion: Ph.D. thesis, Delft University of Technology.

Stolt, R. H., 1978, Migration by fourier transform: Geophysics, **43**, no. 1, 23–48.

Symes, W. W., and Carazzone, J. J., 1991, Velocity inversion by differential semblance optimization: Geophysics, **56**, no. 5, 654–663.

Symes, W. W., and Kern, M., 1994, Inversion of reflection seismograms by differential semblance analysis: Algorithm structure and synthetic examples: Geophysical Prospecting, **42**, no. 6, 565–614.

Tarantola, A., 1987, Inverse problem theory, methods for data fitting and model parameter estimation: Elsevier Science Publ. Co., Inc.

Telford, W. M., Geldart, L. P., and Sheriff, R. E., 1990, Applied geophysics: Cambridge university press.

Thomsen, L., 1986, Weak elastic anisotropy: Geophysics, **51**, no. 10, 1954–1966.

Thomsen, L., 2002, Understanding seismic anisotropy in exploration and exploitation: Society of Exploration Geophysicists.

Tsvankin, I., Gaiser, J., Grechka, V., van der Baan, M., and Thomsen, L., 2010, Seismic anisotropy in exploration and reservoir characterization: An overview: Geophysics, **75**, no. 5, 75A15–75A29.

Tsvankin, I., 2012, Seismic signatures and analysis of reflection data in anisotropic media: Society of Exploration Geophysicists.

van Groenestijn, G. J. A., and Verschuur, D. J., 2009a, Estimating primaries by sparse inversion and application to near-offset data reconstruction: Geophysics, **74**, A23–A28.

——— 2009b, Estimation of primaries and near offsets by sparse inversion: Marine data applications: Geophysics, **74**, R119–R128.

Verschuur, D. J., Berkhout, A. J., and Wapenaar, C. P. A., 1992, Adaptive surface-related multiple elimination: Geophysics, **57**, no. 9, 1166–1177.

Verschuur, D. J., Staal, X. R., and Berkhout, A. J., 2016, Joint migration inversion: Simultaneous determination of velocity fields and depth images using all orders of scattering: The Leading Edge, **35**, no. 12, 1037–1046.

Verschuur, D. J., 2006, Seismic multiple removal techniques - past, present and future: EAGE Publications BV.

Vigh, D., Starr, B., Kapoor, J., and Li, H., 2010, 3D full waveform inversion on a Gulf of Mexico WAZ data set: 80th Ann. Internat. Mtg., Soc. Expl. Geophys., Expanded abstracts, 957–961.

Virieux, J., and Operto, S., 2009, An overview of full-waveform inversion in exploration geophysics: Geophysics, **74**, no. 6, WCC1–WCC26.

Virieux, J., 1986, P-SV wave propagation in heterogeneous media: Velocity-stress finite-difference method: Geophysics, **51**, no. 4, 889–901.

Wapenaar, C. P. A., and Berkhout, A. J., 1989, Elastic wave field extrapolation: redatuming of single- and multi-component seismic data: Elsevier Science Publ. Co., Inc.

Warner, M., and Guasch, L., 2014, Adaptive waveform inversion: Theory: 84th Ann. Internat. Mtg., Soc. Expl. Geophys., Expanded abstracts, 1089–1093.

Winterstein, D. F., 1990, Velocity anisotropy terminology for geophysicists: Geophysics, **55**, no. 8, 1070–1088.

Yang, M., Chen, C., Chazalnoel, N., Ho, R., and Laugier, B., 2016, Are we ready for offsets up to 50 km? Exploring very far and extremely far offsets in subsalt imaging: 86th Ann. Internat. Mtg., Soc. Expl. Geophys., Expanded abstracts, 4336–4340.

Yilmaz, O., 1987, Seismic data processing: Society of Exploration Geophysicists.

Zhang, D., and Schuster, G. T., 2013, Least-squares reverse time migration of multiples: Geophysics, **79**, no. 1, S11–S21.

Zhang, J. F., Verschuur, D. J., and Wapenaar, C. P. A., 2001, Depth migration of shot records in heterogeneous, transversely isotropic media using optimum explicit operators: Geophys. Prosp., **49**, no. 3, 287–299.

Zhou, H., Bloor, R., and Zhang, G., 2006, An anisotropic acoustic wave equation for modeling and migration in 2D TTI media: 76th Ann. Internat. Mtg., Soc. Expl. Geophys., Expanded abstracts, 194–198.

Zuberi, M., and Alkhalifah, T., 2014, Generalized internal multiple imaging: Geophysics, **79**, no. 5, S207–S216.

Summary

One of the most crucial estimates obtained from reflection seismology is the seismic image. It provides a map of the subsurface reflectivities. However, in order to construct an accurate map an accurate propagation velocity model is needed. For simple geologic environments an isotropic velocity model is sufficient, however, for complex geologic environments an anisotropic velocity model is more appropriate and more realistic in describing wave propagation. Ignoring the anisotropic kinematics in these geologic environments will most definitely lead to sub-optimal or even poor imaging results, especially with the tendency of today's acquisition geometries that include measurements at large source-receiver offsets.

This thesis extends the theory of the Joint Migration Inversion (JMI) method to include anisotropic kinematics. In its isotropic implementation, JMI is a full waveform approach that inverts for the subsurface reflectivities and velocities. The scattering information is encoded in the reflectivity operators, while the phase information is encoded in the propagation operators. This strict separation enables the JMI method to decrease the degree of nonlinearity in inversion. JMI utilizes both the primaries and internal multiples in updating the subsurface parameters. Hence, multiples are not considered as noise.

This thesis first considers the case of Vertical Transpose Isotropic (VTI) media. The forward modeling engine Full Wavefield Modeling (FWMod) is updated to include VTI kinematics. This is done through the use of the acoustic anisotropic dispersion relation. Choosing an acoustic anisotropic approximation reduces the number of parameters needed for inversion, thus reduces the null space. However, it does come with some drawback, namely

the pseudo S-wave and the instabilities happening for negative η. Usually, attenuating these artifacts is challenging in standard, so-called finite difference modeling schemes. Utilizing the explicit phase-shift extrapolators (as in FWMod) it is possible to distinguish and attenuate these artifacts in a relatively straightforward manner.

The choice of parameterization is critical in multi-parameters anisotropic inversion problems. The chosen parameterization for this thesis consists of a vertical velocity V_v, a horizontal velocity V_h, and a δ parameterization. This parameterization is convenient in that it reduces the trade-off between the different parameters. Note that δ is not estimated due to its intrinsic ambiguity between it and depth, so its estimates are obtained from other sources of information. Analysis of the cost function gives some insight on its the behavior. We show that estimating only the anisotropic velocities is not ideal (due to the existence on many local minima). However, estimating the best fit reflectivity between anisotropic velocity estimation significantly reshapes the cost function and makes it more suitable for gradient decent methods (due to the absence of most of the local minima). Finally, internal multiples are included in evaluating the cost function. Depending on their relative strength, internal multiples can help in uniquely defining the anisotropic velocities, thus, further reducing the trade-off between the anisotropic parameters.

The method is tested on a number of different synthetic models. The chosen numerical tests become increasingly complex in order to test the limitations of the method. After that, the method is then demonstrated on a 2D marine field data set from the North Sea. Even for a far from correct initial velocity model the method converges to a satisfactory anisotropic solution and the inverted results significantly improve the continuity and focusing of the final image.

Finally, the Tilted Transverse Isotropic (TTI) case is addressed. TTI kinematics are first included in the FWMod scheme. More parameters are needed in order to describe TTI kinematics than in the VTI case, which makes the inversion more challenging. Given the anisotropic model the reflectivity gradient and imaging are updated to include TTI kinematics. We demonstrate the effectiveness of the method in estimating the reflectivities (using primaries and internal multiples) on a subset of the 2007 BP TTI Velocity-Analysis Benchmark model. Furthermore, we analyze the sensitivity of the different TTI parameters on the estimated image. We find that the tilt in particular affects the image significantly, which suggests that it can be incorporated in

inversion. However, one needs to analyze the trade-off between it and the other parameters before inversion. This is left for further research.

The anisotropic JMI methodology presented is a hands-off method that estimates the best fit subsurface reflectivities and anisotropic velocities. It's inherit decoupling of scattering and propagation reduces the nonlinearity and in turn facilitates the inversion process, even with highly erroneous starting models. Furthermore, the methodology aims at explaining more of the physics encountered in the subsurface, therefore, all orders of scattering (primaries and multiples) are included in inversion. Hence, multiples are no longer considered as noise in the data, but rather they are a crucial part of the data that assists in estimating the reflectivities and the anisotropic velocities.

Samenvatting

Een van de meest cruciale schattingen die verkregen wordt uit reflectie seismologie is het seismische beeld. Het geeft een nauwkeurige representatie van de reflectiviteiten van de ondergrond. Echter, om een accuraat seismisch beeld te maken is een accuraat model van de voortplantingssnelheid essentieel. Voor simpele geologische omgevingen is een isotropisch snelheidsmodel voldoende. Echter, voor complexere geologische omgevingen is een anisotropisch model geschikter en realistischer voor het beschrijven van propagatie van de golf. Buiten beschouwing laten van anisotropische kinematica in deze geologische omgevingen leidt hoogstwaarschijnlijk tot een sub-optimaal of zelfs slecht seismisch beeld, in het bijzonder met de tendens van hedendaagse acquisitie geometrien die metingen omvatten met grote afstanden tussen bron en ontvanger.

Deze thesis breidt de theorie van Joint Migration Inversion (JMI) methode uit, zodat het anisotropische kinematica omvat. De isotropische implementatie vam JMI is een volledige golfveld methode die inverteert voor de ondergrondse reflectiviteiten en snelheden. De verstrooiingsinformatie is versleuteld in de reflectiviteit operatoren, terwijl de fase informatie versleuteld is in de propagatie operatoren. Deze strikte scheiding maakt het mogelijk dat de JMI methode de mate van niet-lineariteit in de inversie vermindert. JMI gebruikt zowel de enkelvoudige als meervoudige reflecties in het updaten van de parameters van de ondergrond. Daarom worden de meervoudige reflecties niet beschouwd als ruis.

Deze thesis beschouwt allereerst Vertical Transpose Isotropic (VTI) media. Het voorwaartse modellering programma Full Wavefield Modeling (FWMod) is bijgewerkt, zodat VTI kinematica worden meegenomen. Dit wordt gedaan

door het gebruik van de akoestische anisotropische dispersie relatie. Het maken van een akoestische anisotropische schatting vermindert het aantal parameters dat nodig is voor de inversie sterk, en verkleint zodoende de nulruimte. De keerzijde is echter de pseudo S-golf en de instabiliteiten die ontstaan door een negatieve η. Normaal gesproken is demping van deze artefacten lastig in standaard, zogenaamde eindige differentiemethoden. Met het gebruik van de expliciete fase-verschuiving extrapolatoren (in FWMod) is het mogelijk onderscheid te maken tussen de artefacten en deze op een simpele manier te dempen.

De keuze van de parametrisering is cruciaal in multiparameter anisotropische inversie problemen. De gekozen parametrisering voor deze thesis bestaat uit een verticale snelheid V_v, een horizontale snelheid V_h en een δ parametrisering. Deze parametrisering is handig omdat het de wisselwerking tussen de verschillende parameters vermindert. Merk hierbij op dat δ niet geschat wordt door de intrinsieke ambiguteit tussen δ en de diepte, dus de schattingen hiervoor worden verkregen door andere informatiebronnen. Een analyse van de kostenfunctie geeft inzicht in het gedrag van de kostenfunctie. We laten zien dat het schatten van alleen de anisotropische snelheden niet ideaal is (door het bestaan van lokale minima). Echter, het schatten van de best passende reflectiviteit met de geschatte anisotropische snelheid hervormt de kostenfunctie aanzienlijk en maakt het geschikter voor gradint optimalisatie methoden (door de afwezigheid van lokale minima). Ten slotte worden interne meervoudige reflecties meegenomen in het bepalen van de kostenfunctie. Afhankelijk van hun relatieve gewicht, kunnen interne meervoudige reflecties helpen bij de unieke bepaling van anisotropische snelheden en kunnen zodoende helpen bij het verminderen van de wisselwerking tussen de anisotropische parameters.

De methode wordt getoond voor verschillende synthetische modellen. De gekozen numerieke tests worden steeds complexer om de beperkingen van de methode te testen. Daarna wordt de methode getoond op 2D mariene data uit een veld in de Noordzee. Zelfs voor een verre van correct initieel snelheidsmodel convergeert de methode tot een bevredigende anisotropische oplossing en de genverteerde resultaten verbeteren de continuteit en de focus van het uiteindelijke beeld significant.

Ten slotte wordt de Tilted Transverse Isotropic (TTI) casus behandeld. TTI kinematica worden eerst in het FWMod schema gentegreerd. Meer parameters zijn nodig om de TTI kinematica te beschrijven dan in het geval van VTI,

hetgeen de inversie moeilijker maakt. Gegeven het anisotropische model, worden de reflectiviteits gradient en beeld bijgewerkt zodat de TTI kinematica inbegrepen zijn. We demonstreren de effectiviteit van de methode in het schatten van de reflectiviteiten (enkelvoudige en meervoudige reflecties inbegrepen) op een gedeelte van het 2007 BP TTI Velocity-Analysis Benchmark model. Bovendien analyseren we de gevoeligheid van de verschillende TTI parameters voor het geschatte beeld. We merken dat de schuine helling in het bijzonder het beeld sterk benvloedt, wat suggereert dat het in de inversie opgenomen kan worden. Men moet echter voor de inversie de wisselwerking tussen deze en andere parameters analyseren. Dit laten we voor volgend onderzoek.

De anisotropische JMI methodiek die hier gepresenteerd wordt is een hands-off methode die de best passende ondergrondse reflectiviteit en anisotropische snelheid schat. De inherente loskoppeling van verstrooiing en propagatie reduceren de niet-lineariteit en helpen het inversie proces, zelfs voor zeer onjuiste beginmodellen. Bovendien probeert de methodiek de fysica van de ondergrond beter te beschrijven en daarom worden alle ordes van verstrooiing (enkelvoudige en meervoudige reflecties) meegenomen in de inversie. Dus meervoudige reflecties worden niet langer beschouwd als ruis in de data, maar gelden als een cruciaal onderdeel van de data die helpen bij het schatten van de reflectiviteit en de anisotropische snelheden.

Acknowledgments

"*The journey of a thousand miles begins with one step*" Lao Tzu. I vividly remember my first steps from learning what **WRW** is to relearning how to ride a bicycle again in order to get to work. During this four year journey I have come to realize that I would not be where I am today without the help of my family, friends, and colleagues. My only regret in my Msc thesis was that I did not take the time to really acknowledge everyone who helped me get to where I am. So, I will try to give a little credit here to everyone who has helped or influenced me along the way.

First and foremost, I thank my co-promoter and daily supervisor Dr. D.J. (Eric) Verschuur. I am proud and honored to be your student and to have been supervised by you. I have truly learned a lot, not only in the theoretical aspect of our science but also on the practical side as well. I recall the first time I met you was in Dhahran when you were visiting Saudi Aramco. I was working on an adaptive subtraction method that took me weeks to get working, with many unsatisfactory results. After meeting you, you suggested that we have a meeting and a couple of days later the method was ready for implementation on the toughest data sets I had. Ever since that moment I knew I wanted to work with you. I valued the research freedom that you give me, at the same time whenever a challenge arises that was too difficult you were always there to provide a creative yet practical solution. I was fortunate enough to witness the handing of the Delphi consortium to Eric. Despite the significant increase in logistical work, I have never had to hesitate to stop by his office with any questions. I look forward to our continued collaboration in the future.

I also thank my promoter Prof. Lucas van Vliet for his thorough review of

my thesis and my propositions. I appreciate your valuable and fresh insight on various aspects of the thesis. I also thank Prof. Tariq Alkhalifah for your thorough review of my thesis, your comments and suggestions have improved its quality. I was always inspired by your talks in the SEG/EAGE meetings and to have you being part of my thesis committee is a pure pleasure. Furthermore, I thoroughly enjoyed the courses you taught me at KAUST, I always found them to be enlightening. I distinctly remember that I was introduced to inversion based velocity analysis by you, back in 2009, on an inversion project that I worked on with you. Eight years later I am writing my thesis on an inversion based velocity analysis method.

I thank Prof. Colin Macbeth, I was fortunate to meet you during your sabbatical year in the TUDelft/Shell. I enjoyed your talks where you linked geophysics with engineering. Moreover, your book "Multi-component VSP analysis for applied seismic anisotropy" was one of the main sources of information for me during the early days in my PhD. Thank you for your review of my thesis. I thank Prof. Jacob Fokkema for your review and I also thank you for teaching me one of the most rewarding course I took at TUDelft, the "Advanced wave theory for geoscientists". I thank the rest of my committee members Prof. Andrei Metrikine and Dr. Barbara Cox for their review of my thesis.

The vision of Prof. A.J. Berkhout (the founder of the Delphi consortium) has always been the corner stone that I turn to when ideas run dry. I have come to realize that it is much more fruitful to go back to the fundamentals and find the root of the problem rather than trying to get the method to "work" for the time being. I also thank you for ever so eloquently convincing me that internal multiples are an essential part of our data that should not be eliminated. I will take with me many of the ideas and try to implement them in my new job. I wish you all the best in your new endeavors and do sincerely hope we get to work together again.

I would not be here without the kind sponsorship of Saudi Aramco. Saudi Aramco has been an integral part of my PhD life, besides giving me this opportunity, it has always ensured that everything is taken care of and I can focus on my studies. I would like to thank in particular the division head of Geophysical Technology (GPT) Dr. Mustafa Al-Ali for constantly following up with me and ensuring that I am always part of GPT. I also thank Dr. Panos Kelamis (for actually introducing me to Delphi), Dr. Constantinos Tsingas, Dr. Andrey Bakulin, Dr. Gaithan Muntashiri (for encouraging me

to go to TUDelft), and Mohammad Bannagi for helping me at various stages of my PhD studies. I look forward in coming back and applying the ideas I learned in Delphi.

I also thank the Delft arm of GPT, Dr. Roald van Borselen, Dr. Yimin Sun, Dr. Hannes Kutscha, Dr. Jewoo Yoo, Dr. Mikhail Belonosov, and Dr. Rob Hegge. Having you nearby to bounce ideas off was a pure pleasure, also there was always a friendly Aramcoan face nearby (quit literally around the corner). I appreciate your suggestions towards my thesis and I wish the center continued success and prosperity. Aramco Overseas Company (AOC) has been instrumental in easing my transition to the Netherlands. I would particularly thank its CEO Mr. Fahad AbdulKareem for extending a warm hand to the students in the Netherlands and in including us in AOC's many social activities. I also thank Ms. Aggie Cooper my career advisor from AOC for following up with me and ensuring that all the logistics are taken care of and I can focus on my studies. I always enjoyed your annual visits to check that I was on track. I was checking my email and I noticed that on average I sent you an email almost every month! Thanks for putting up with me and my many requests.

I thank the Delphi sponsors for making the consortium what is today. I also thank you for your interesting discussions at the Delphi meetings. I always consider the questions posed at the sponsor meetings as opportunities for improving my thesis, thanks for both the tough and easy questions. I also thank Dr. Gerrit Blacquière the chairman for the Acquisition and Preprocessing (A&P) project in Delphi. I always found your talks in the A&P day to be fascinating (especially the ones on robotics) and they actually got me interested in the acquisition part of the industry, something I plan to delve deeper into once I get back to Saudi Aramco. I also thank Delphi supervisors Prof. A. Gisolf and Dr. F. Vossepoel for your feedback on my project at the various Delphi meetings.

A special thanks goes to my Delphi colleagues, I consider you as family, we usually work together 8+ hours a day and we travel together 4+ times a year to the different conferences and sponsor meetings. I always enjoyed your company and enjoyed our social outings. The 12 hour flight to Houston becomes fun when there are friends in the next 15 seats to talk to. It worries me to think that the flights to Houston will never be as enjoyable as with you guys. I thank the older generation of students: Dr. Xander Staal (the original JMI Guru), Dr. Alok Soni, Gabrio Rizzuti, Dr. Gabriel Lopez, Dr.

Mikhail Davydenko, Dr. Amarjeet Kumar, Dr. Tomohide Ishiyama, Dr. Peter Haffinger, Dr. Panos Doulgeris, and Apostolos Kontakis (my lunch buddy for 4 years). I also thank the newer generation of students: Shogo Masaya (my office/tea buddy), Hussain Hammad, Bouchaib El Marhfoul, Shan Qu, Sixue Wu, Matteo Caporal, Jan-Willem Vrolijk, Aayush Garg, Aparajita Nath, Nick Luiken (thanks for the Beschuit met Muisjes and the translation of my summary and propositions in Dutch), Siddarth Sharma, Runhai Feng, and Dr. Özkan Sertlek. I wish you all the best of luck in your future endeavors and if we meet in future meeting don't worry I won't ask "too many" questions.

A warm thanks goes to the medical imaging group in Acoustic Wavefield Imaging (AWI) I thoroughly enjoyed the seminars and talks, it is truly fascinating that you apply the same physics but on a much smaller scale for imaging tiny vessels in the human body. I also thank the geophysics department in CiTG. Some of the most memorable and enjoyable courses where there. I thank colleagues from CiTG: Dr. Niels Grobbe, Dr. Pawan Pisupati, Dr. Yohei Nishitsuji, Max Holicki, Dr. Joost van der Neut, and the rest of the wonderful CiTG group. TUDelft has been my home for the past 4 years and the many colleagues there have been instrumental in making Delft feel like home. I thank our vibrant former secretary Margaret van Fessem for all her help and easing my transition to the Netherlands. Thank you for translating the many Dutch documents I get in the mail, without which I would have missed many appointments. I also thank Henry den Bok, Edo Bergsma, and Angela van der Sande for making everything run smoothly in the department. I enjoyed your discussions during the coffee breaks. I also thank you for letting me know when the Dutch public holidays are, without that I would have had many strange days in the office while no one was here.

I also thank my Saudi colleagues at Delft. When I first arrived in Delft I was the only Saudi student in the campus, as the months went by more came and some even already graduated. As I am leaving there are a dozen or so Saudi students still working towards different degrees. I was fortunate to have you guys around and thank you for the good old Saudi dinners. I thank Bander Alquaimi, Ahmad Alayesh, Raid Saadan, Ali Alfaraj, Abdulmohsen Alali, Hussain Hammad, Naif Alghamdi, Abdullah Aljeffri, Omar Abdulgader, Feras Alshehri, Ahmad Alwoshel, and Abdulmohsen Almansour (thanks for the farewell party). I wish you all the best in your studies and I hope to see you in Saudi. Please forgive me if I unintentionally miss

someone's name.

My MSc at KAUST weighed heavily on my eagerness to do research, for that I thank the following: Prof. Martin Mai who actually introduced me to scientific writing. Furthermore, your eagerness to discover different geophysical/geologic features in the Arabian peninsula is always an inspiration. Prof. Gerard Schuster, you thought me most of the courses at KAUST and I was always excited by each course. I still remember you saying that if you can't explain it in 10 words or less then you don't understand it. I took this with me and till this day I try to be brief in my explanations. I also thank Prof. Tariq Alkhalifah, Prof. Sigurjón Jónsson, and Dr. Ibrahim Hoteit. Those early days at KAUST were some of the most exciting in my life. It was during those early days at KAUST where I understood what it meant to be part of the scientific community. I also thank the professors at KFUPM where I did my bachelors. I thank Dr. A. Al-Shaibani, Dr. A. Abukhodair, Dr. M. Hariri, Dr. A. Al-Shuhail, Dr. M. Makkawi, and Dr. A. Abdulghani. Without your foundation I would not have been able to purse graduate studies. It is always a pleasure when I bump into you at the different conferences and I hope to have more scientific collaboration when I am back in Dhahran.

My family has been my source of strength throughout my life, whether I come back home with good or bad results they are always there supporting me to go further. I start with my father Dr. Abdullatif Alshuhail you have been an inspiration to me all my life. This thesis is dedicated to you and I only wish that it gains your approval. I knew I wanted to do a PhD ever since I was a 6 year old kid following around the Texas A&M campus and seeing all the "cool" rocks in the laboratory. You also thought me to never never never never give up no matter how difficult it gets, something that had helped me tremendously when my research was not going the way I wanted it. I also thank my mother Noriyah Albedah for creating a nurturing and loving environment and taking care of us. Thank you for your many visits to the Netherlands and bringing sweets and other delicacies from Saudi. I always joked that my mom never packed a suitcase with cloths, it was always full of sweets and food from Saudi.

I thank my brother Abdullah for being one of my best friends for as long as I can remember, I have faith in the Saudi banking system while you are still working there. I thank my sister Shamael, I am confident that you have a bright future ahead of you. I thank my brother Faisal for being the first person to visit me in the Netherlands. I thank my brother Talal, I know that

I can rely on you for anything and I know you will get it done. I thank my little sister Lujain for the gifts and the smiles. I also thank my in-laws the Alshekhmubarak family for visiting us in the Netherlands and taking care of me and my wife when our baby was born and showing us how to calm a crying baby (not an easy task).

Finally, I thank my wife Norah. We have been a on a wonderful adventure these last 2 years and I look forward for more in the future. I would not have been able to finish my PhD on time without your help and support. The last 6 months of my PhD were quite a crunch and you were always supportive of my dreams. I also thank you for painting the cover of this thesis, some say it's the best part. As I am writing my acknowledgments we were blessed with a son (2 weeks ago), we named him Yousef. A smile from you automatically makes all in the room smile. I thank you for brightening up my days.

Abdulrahman Alshuhail
11 May 2017